Study of contributions of diffractive processes to forward neutral particle production in p-p collisions at $\sqrt{s} = 13$ TeV with the ATLAS-LHCf detector

Qi-Dong ZHOU
Division of Particle and Astrophysical Science
Graduate School of Science
Nagoya University

A thesis submitted in fulfillment of the requirements
for the degree of Doctor of Science

February 2018

NAGOYA
UNIVERSITY

Abstract

Knowing the properties of ultra-high energy cosmic rays (UHECRs) is extremely important to solving the puzzle of their origin. Determination of the mass composition and reconstruction of the energy of UHECRs, based on the interpretation of large scale ground-based experimental data depends strongly on the Monte Carlo (MC) simulation of air showers. Limitations in the modelling of hadronic interactions, which are widely used in the MC simulations, and the unknown model uncertainties lead to large uncertainties when interpreting the measurement data. So an adequate understanding of hadronic interactions occurring between cosmic-ray and the atmosphere is the key to solving the puzzling origin of UHECRs. The Large Hadron Collider forward (LHCf) experiment is a unique experiment dedicated to measuring the neutral particle production in the very forward region of the LHC to understand the hadronic interactions. According to the published LHCf results, no hadronic interaction model can predict the various data perfectly. Corresponding forward neutral particle production is able to provide the unique constraint to the parameters in the models, improving the accuracy of determination of properties of UHECRs.

To explore the potential of the LHCf data for improving the hadronic interactions, in this work we studied the different contributions of diffractive processes to the inclusive forward neutral particle production in the *p*-*p* collisions at $\sqrt{s} = 13$ TeV by using MC simulations. It is able to specify the poor constraint on the aspect of diffractive interactions (especially the low-mass diffraction) in the models. We first evaluated the methodology for classifying the LHCf observables into specific interaction types of single, double diffraction or non-diffraction by using the ATLAS-LHCf apparatus. It was confirmed that the ATLAS-LHCf common experiment has a unique sensitivity to the low-mass diffraction, which has never been measured directly at high energies. Low-mass diffraction is still not well implemented in the model, and it is sensitive to inelasticity which is a key parameter controlling the global characteristics of air-shower developments.

The identification of diffraction based on the rapidity gap technique has been investigated. The low-mass diffractive events at $\log_{10}(\xi_x) < -5.5$ can survive from the central-veto selection, which requires *no charged particles in the kinematic range of* $p_\mathrm{T} > 100$ *MeV and* $|\eta| < 2.5$. Among the event samples observed by LHCf, the corresponding central-veto selection has approximately 100% purity and 100% efficiency for the identification of low-mass diffraction.

The first ATLAS-LHCf joint analyses have been accomplished based on 0.191 nb^{-1} of *p*-*p* collision data recorded at $\sqrt{s} = 13$ TeV. The photon energy spectra were measured in two pseudorapidity ranges, $\eta > 10.94$ or $8.81 < \eta < 8.99$, for the events with no extra charged particles having $p_{\mathrm{T}} > 100$ MeV and $|\eta| < 2.5$. Both LHCf and ATLAS data were unfolded for the detector effects. By applying the event selection and the necessary corrections, as well as estimating the systematic uncertainties, the photon production cross-section of low-mass diffraction were shown and compared with four post-LHC models. Furthermore, the ratio of photon spectra derived from the low-mass diffraction to the inclusive photon spectra was calculated and also compared with the predictions of models. It was confirmed the pomeron flux is a dominant parameter for the implementation of diffractive dissociation in the SIBYLL2.3c-Diff model, which improves the production of low-mass forward photons by using joint analyses results to tune the pomeron flux of the SIBYLL2.3 model. The corresponding tuning of low-mass diffraction has strong correlation with inelasticity, resulting in shifting the determination of X_{max}.

Contents

List of Figures

List of Tables

Acknowledgements

I would like to express my gratitude to my supervisor, Prof. Y. Itow for providing me with this opportunity to complete this research project, and giving me a lot of useful advices. I would also like to thank Prof. T. Sako and Dr. H. Menjo for taking time to give me many valuable advices, instruction, and elaborated guidances during many years of research with LHCf group. They provided me the essential support for completing this research.

I am deeply grateful to Prof. Y. Muraki, Prof. O. Adriani, and other LHCf collaborators to give me useful comments and suggestions. I would also like to thank Prof. H. Tajima, Prof. K. Masuda, Prof. Y. Matubara, Prof. F. Abe for teaching me various knowledge about fundamental physics especially about cosmic-ray and giving me a lot of encouragement.

Thanks to Prof. L. Adamczyk for the very good collaboration works, including many support and suggestions for the joint analyses with ATLAS.

I also want to show my appreciation to E. Berti, A. Tiberio, Y. Makino, E. Matsubayashi, M. Ueno, M. Shinoda, K. Sato, K. Ohashi and all members in CR lab for meaningful discussions and support.

I am also grateful to the program of Leadership Development Program for Space Exploration and Research, NGK INSULATORS LTD. Foundation Scholarship, JASSO international students scholarship for making my study possible by the financial support.

Finally, I would like to offer my special thanks to my family for their endless love, understanding, and encouragement. For they supported in all my pursuits, and all their sacrifice throughout my study. No matter where life takes me, they are always the reason let me to keep a smile to my life.

Chapter 1

Introduction

1.1 Cosmic Rays

1.1.1 Overview

Cosmic rays (CRs) were discovered by Austrian physicist Victor Hess in 1912. He made a historic balloon flight to measure the rate of ionization in the atmosphere and found that the radiation increased about three times than that at sea level. Thus, he concluded the radiation was entering the atmosphere from above. Now we know that these particles are mainly protons (89%) but also include helium nuclei (10%) and heavier nuclei (1%) with energy up to 10^{20}eV. Figure 1.1 shows the energy spectrum of primary CRs at high energies. The flux of CRs decreases dramatically as the energy rises up. The expected integral fluxes of CRs are 1 particle / m^2 sec at 10^{11} eV, 1 particle / m^2 year at 10^{15} eV and 1 particle / km^2 year at 10^{18} eV. The steepen structure of energy spectrum at around $10^{15.6}$ eV and the flatten structure at around $10^{18.7}$ eV called "knee" and "ankle", respectively. Another steepen structure at around $10^{17.2}$ eV between knee and ankle is "2nd knee", the rapid steepening around 5×10^{19} called Greisen-Zatsepin-Kuzmin (GZK) cutoff. Corresponding energies of these structures can be expressed by E_{knee}, $E_{2nd\ knee}$ and E_{ankle}. The differential flux of CRs can be described by Equations 1.1,

$$\frac{dN}{dE} \propto \begin{cases} E^{-2.87}(E < E_{knee}) \\ E^{-3.0}(E_{knee} < E < E_{2nd\ knee}) \\ E^{-3.29}(E_{2nd\ knee} < E < E_{ankle}) \\ E^{-2.53}(E_{ankle} < E). \end{cases} \tag{1.1}$$

Though the origin of high-energy CRs is still the most outstanding problem in the field of CRs, basically, the most viable theory of the CR origins is that they are generated in

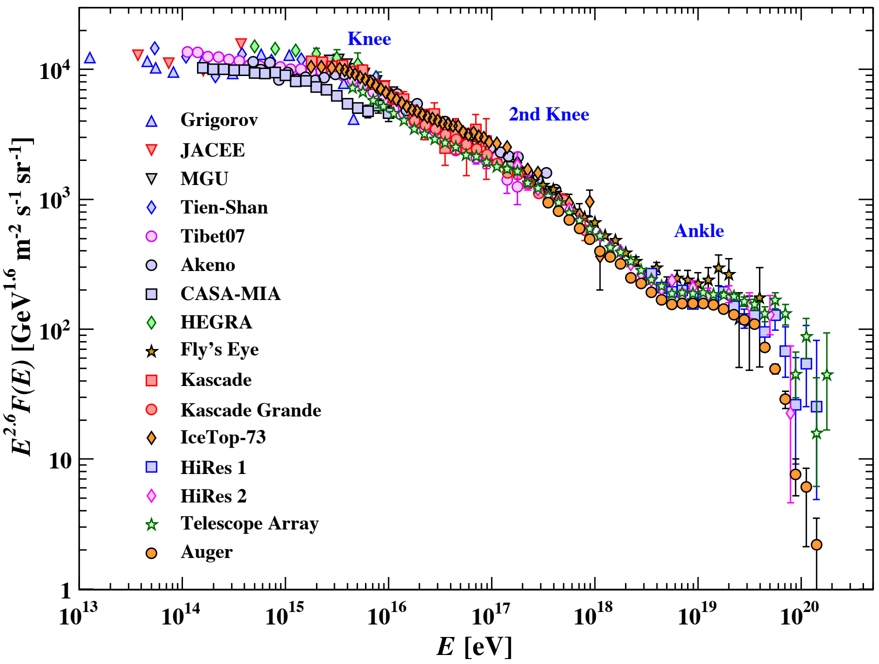

FIGURE 1.1: The energy spectra of cosmic-ray from high to ultra-high energies observed by several experiments [5].

the shock waves of supernova remnants (SNR) in the energy regions below 10^{17} eV [1]. In such a case, CRs are accelerated through the so-called Fermi mechanism [2], which explains the acceleration of CRs by mean of their collisions with interstellar clouds. The particles of CRs are reflected off these clouds, which act as magnetic mirrors. The reason to choose this model is that it succeeds in describing the power law of the observed energy spectrum. On the other hand, it unable to explain the presence of CRs with energies above 10^{18} eV, so-called Ultra-High Energy Cosmic Rays (UHECRs). Two plausible classes of astrophysical accelerators, so-called Gamma Ray Bursts (GRBs) [3] or Active Galactic Nuclei (AGNs) [4], are the candidates of UHECR origin.

The shape features of energy spectrum contain important information of CRs' propagation and acceleration mechanisms and, furthermore of their sources. Hereby, following scenarios explain the structures of the spectrum. The observed structure of "knee" is because that the dominant composition of galactic CRs; proton reaches to its accelerating limit at around E_{knee} energy. Because the maximum energy of accelerated particles is proportional to rigidity (pc/Z), heavy galactic nuclei continuously reach to their accelerating limit of energy until $E_{2nd\ knee}$. Recent observations supported the scenario of that there is a transition of the sources of CRs from galactic to extra-galactic between

$E_{2nd\ knee}$ and E_{angle}. There is no galactic astrophysical source is capable of accelerating the UHECRs to such high energies, besides, it is known that the galactic field is too weak to contain UHECRs particles. Therefore, contribution of extra-galactic sources dominates the formation of ankle.

1.1.2 Ultrahigh-energy cosmic rays

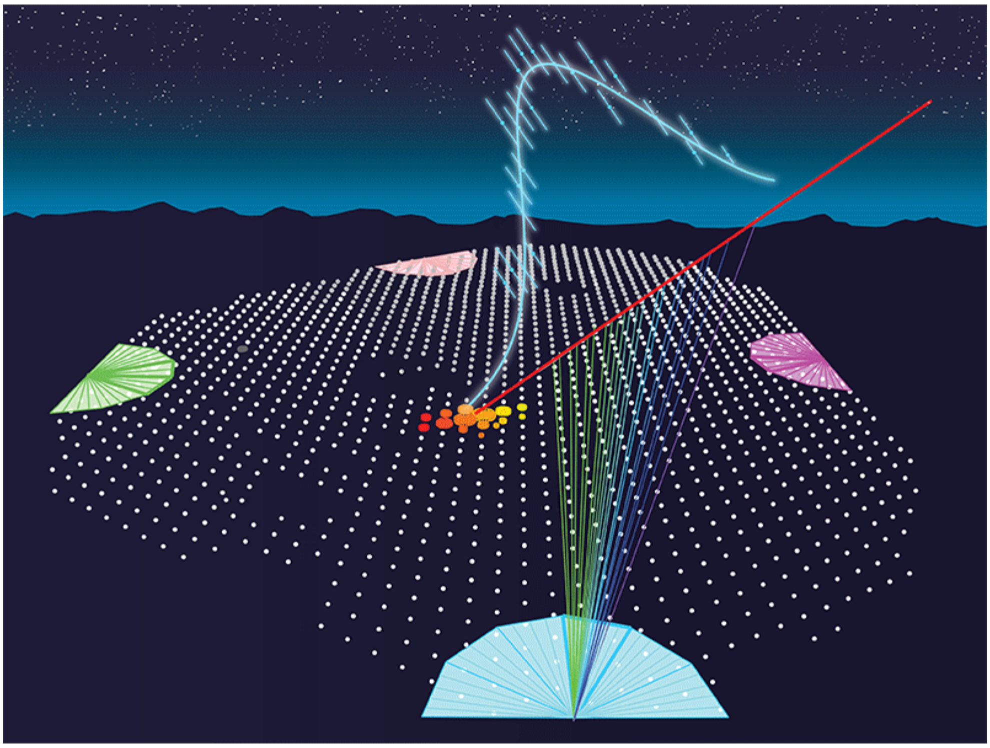

FIGURE 1.2: The illustration of the detection of a hybrid event in PAO, which by using fluorescence telescope (light blue semicircle) and the array of water Cherenkov detectors (white dots) [6].

The CR flux would have a rapid steepening at extremely high energies which was predicted by Greisen [7] Zatsepin and Kuzmin [8]. Protons with the energy above $10^{19.5}$ eV from extra-galactic sources (assumed the inter-galactic distances $\sim$ 10-100 Mpc) are not expected to reach the earth, because these protons will interact with cosmic microwave background (CMB) photons (the proton's mean free path for this interaction is $\sim$ 3 Mpc) losing energy while producing pions. The GZK cutoff energy corresponds to the energy threshold of the interaction shown as below,

$$p + \gamma \longrightarrow \Delta^+(1232) \longrightarrow \begin{cases} p + \pi^0 \\ n + \pi^+. \end{cases} \tag{1.2}$$

After the experimental efforts in the last decade, one of the big achievements is the confirmation of GZK cutoff at around $10^{19.5}$ eV as shown in Fig. 1.1 [9, 10].

At different energy ranges, the techniques used for measuring CRs are also different. CRs with the energy below 10^{14} eV are directly measured by using balloons and satellites, owing to their large flux. Due to the flux of UHECRs in the universe is extremely small, almost 1 particle/year/km^2, large area ground-based measurement of extensive air-shower (EAS) is widely used to study their properties. When a CR particle collides with a molecule in Earth's atmosphere, it generates a cascade of secondary particles so-called "air-shower". There are two methods to observe the induced air-shower at the ground which are illustrated in Fig. 1.2.

- Measurements of lateral densities of all charged particles and/or exclusively muons by ground-based detector array.
- Measurements of fluorescence emission induced by the charged particles in air-showers during dark and clear night by using telescopes.

Both methods can generally be powerful enough for determining the primary energy and composition of UHECRs. In general, the longitudinal development profiles of air-showers observed by the fluorescence detector are usually used for the determination of the compositions of primary cosmic rays. There are two big experiments dedicated to observing UHECRs by using both techniques. The Pierre Auger Observatory (PAO) [10] located in the southern hemisphere, and the Telescope Array (TA) [11] experiment located in the northern hemisphere. Two experiments have observed a considerable number of UHECRs events in the energy regions up to 10^{20} eV as shown in Fig. 1.1. It also indicates that a consistent energy spectra for UHECRs were obtained based on two different kinds of detection techniques.

1.1.3 Mass composition measurement of UHECRs

The chemical composition is an extremely important parameter for researching the origin and acceleration mechanism of UHECRs. As shown in Fig. 1.3, it indicates the distance of candidate sources of UHECRs for different groups of chemical compositions on the bias of a uniform source distribution. It is worth noting that only protons and iron nuclei survived when the source distance is larger than 50 Mpc.

Determination of composition of UHECRs is preformed by using an estimator, so-called X_{max} [g/cm^2], which is the maximum depth of longitudinal shower development (the mean depth in the atmosphere where maximal number of ionizing particles is observed) in the atmosphere. It is known that X_{max} depends strongly on the nuclei mass number. The heavy nuclei can be simply regarded as several lower energy nucleons. Comparing

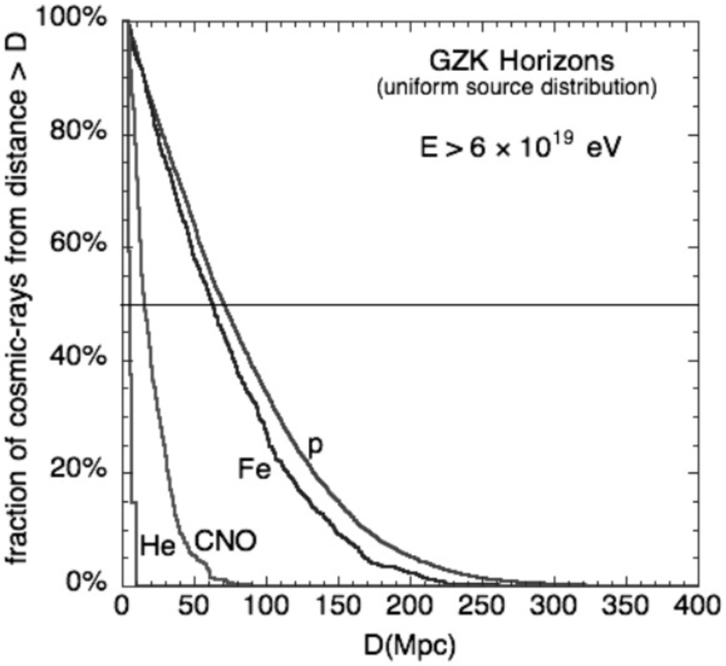

FIGURE 1.3: GZK horizons for proton and nuclei with different faction of attenuation [12].

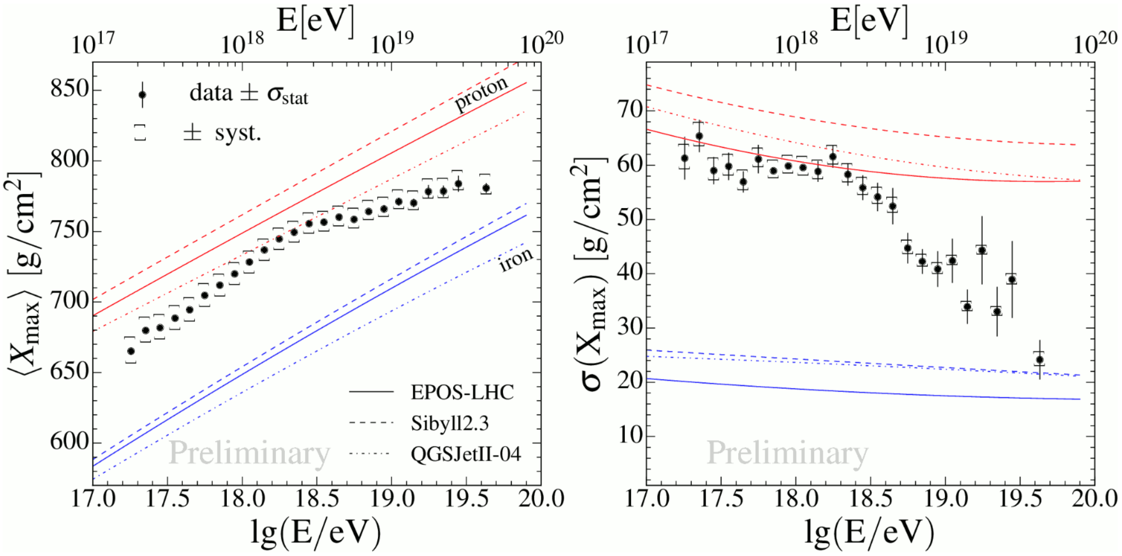

FIGURE 1.4: The mean (left) and the standard deviation (right) of X_{max} measured by PAO compared with post-LHC hadronic interaction models [13].

with a same energy proton, a heavy nucleus as primary CR will start the development of air-shower in the atmosphere earlier (due to the larger total cross-section) with larger multiplicity. At the same time, the shower will reach to the shower maximum at the higher altitude of the atmosphere, which corresponds to a smaller X_{max}.

The measurement of X_{max} is mainly based on the fluorescence light detection techniques. During the shower development, the charged particles excite nitrogen molecules in the atmosphere, then induce fluorescence emissions. The yield of fluorescence lights is proportional to the energy of electromagnetic (EM) components in air-shower. Such EM components carry approximately 90% of the primary energy of CRs. Figure 1.4 shows the mean and standard deviation of X_{max} measured by PAO compared with MC predictions [13]. The red lines indicate the simulations assumed all primary UHECRs are pure proton, the blue lines correspond to pure iron nuclei. Auger claims that light nuclei play a dominated role at around $10^{18.3}$ eV, while the fraction of heavy nuclei is increasing up to energies of $10^{19.6}$ eV [14]. On the other hand, the other large experiment TA claims that the observed data prefers a light composition [15]. Since the interpretations of measurement data rely on the choice of the simulation models, the large uncertainties among simulation models are remaining problems for the mass determination.

1.1.3.1 Muon issue reported by Pierre Auger Observatory

Recently, the hottest topic in the cosmic-ray observations is the ”muon excess” issue. Pierre Auger Observatory reported the number of muon at the ground level is considerably larger than that of the expectation of air-shower simulations based on the hadronic interaction models [16]. It directly connects to the determination of muon production depth, which is an estimator of the UHECRs composition similar to X_{max}. Figure 1.5 (a) shows the $< X^{*\mu}_{max} >$ from the inclined showers as a function of energy measured by PAO. Figure 1.5(b) is the parameter of average logarithmic mass $< \ln A >$ for evaluating the mass composition. According to the comparisons between data and MC predictions, the models predict unreasonable mass compositions which the mass number is larger than iron nuclei.

1.2 Hadronic interactions in air-shower

1.2.1 Phenomenological model

Inelastic hadronic collisions are usually classified into *soft processes* and *hard processes*. The momentum transfer $-\,t$ is only the energy scale to categorised the corresponding processes. Because the cross-section of inelastic hadronic collisions can be expressed as an exponential function of t, so that the large t events are strongly suppressed. The elastic scattering and diffractive dissociation are the two typical examples of soft processes, meanwhile, two classical examples of hard precesses are deep inelastic scattering and large-p_T jet production. Most of the hard processes can be treated within a theoretical framework based on perturbative quantum chromodynamics (QCD) owing to

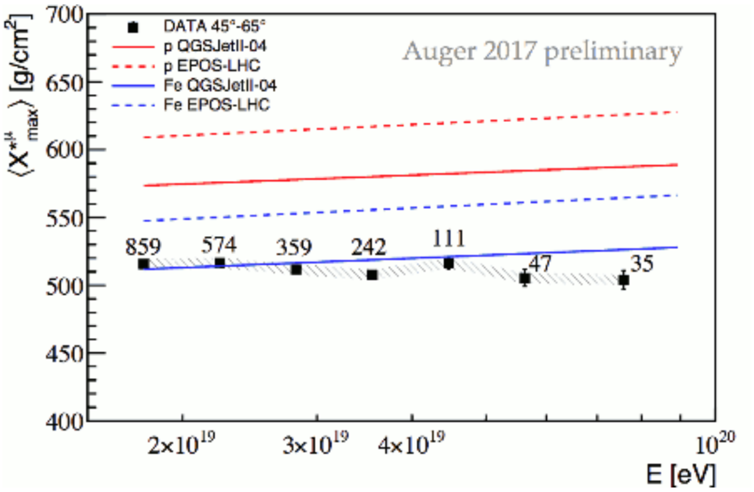

(a) $< X^{*\mu}_{max} >$ as a function of energy.

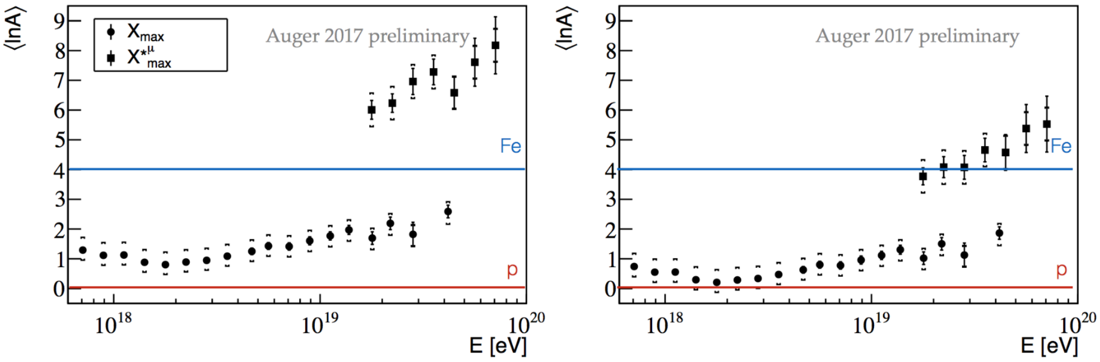

(b) Comparison of $< \ln A >$ converted from $< X^{*\mu}_{max} >$ and $< X_{max} >$

FIGURE 1.5: (a) The muon production depth $< X^{*\mu}_{max} >$ as a function of energy measured by PAO compared with the predictions of hadronic interaction models. (b) The evaluation of $< \ln A >$ as a function of energy which is obtained from the $< X^{*\mu}_{max} >$ and $< X_{max} >$. Predictions of EPOS-LHC (left) and QGSJetII-04 are shown as reference. [16].

the large momentum transfer. However, perturbative QCD is inadequate for describing soft processes such as diffractive dissociation. Instead, the phenomenology of soft hadronic processes based on Gribov–Regge theory [17, 18] has been employed to describe these processes at high energies. Therefore, it is extremely important to constrain the phenomenological parameters based on experimental data to obtain the correct understanding of various diffractive processes and their accurate contribution to the total inelastic cross-section.

1.2.2 Interpretation of air-shower measurement

In experimental studies of UHECRs, the properties of primary UHECR particles (protons and nuclei) are reconstructed from the measured characteristics of nuclear-electromagnetic cascades which are induced in the atmosphere. Determination of primary mass composition and reconstruction of primary particle energy depend strongly on the Monte Carlo (MC) procedures used for numerical simulations of air-showers. These MC simulations are however made by assuming the hadronic interaction which is hardly predicted theoretically. It leads to the big systematic uncertainty for interpretation of measurement data. In the last decade, even after the improvements of the energy resolution and the statistics of data in ultra-high energy regions, there is still a problem remaining for the precise determination of energy and mass composition of UHECRs. For instance, the determination of mass composition as illustrated in Fig. 1.4, the uncertainties among model predictions are much larger than the experimental systematic and statistical uncertainties. Limitations in modelling of hadronic interactions and the largely unknown uncertainties in the models lead to large uncertainties in interpreting the measurement data [19, 20]. As shown in Fig. 1.4, the Auger data are shown together with three predictions estimated based on the interaction models. The same experimental data interpreted with different model, resulting in a different conclusion. Recently, several popular hadronic interaction models are widely used in the interpretation of CRs experimental data are EPOS-LHC [21], QGSJET-II-04 [22], SYBILL 2.3 [23, 24], the one which particularly used in high energy experiments is PYTHIA 8 [25, 26].

Basically, the inherent uncertainties of modelling the hadronic interactions between CRs and atmosphere mainly due to several parameters. The development of air-showers depends strongly on the key quantities as illustrated in Fig. 1.6,

- the total inelastic cross-section,
- the leading particle spectrum,
- the multiplicity,
- the pion charge ratio,

Figure 1.6 shows the mean value and standard deviation of X_{max} predicted by SIBYLL2.1, corresponding to $10^{19.5}$ eV proton and iron primaries. In order to investigate the influences of different parameters for the determination of X_{max} and $\sigma(X_{max})$, f_{19} is defined as a reference variable which is used to evaluate all the other four parameters. $f_{19} = 1$ for each parameter means the value of corresponding parameter used in the simulation of 10^{19} eV primary shower. The parameters has already been constrained by accelerator data below 10^{15} eV. Because the interpretation of CR properties relies on the extrapolation to the UHECRs energies, it means we have to extrapolate all the four parameters based on the low-energy data. Figure 1.6 illustrates the relative extrapolation uncertainties of each parameter. These parameters play an important role for the determination

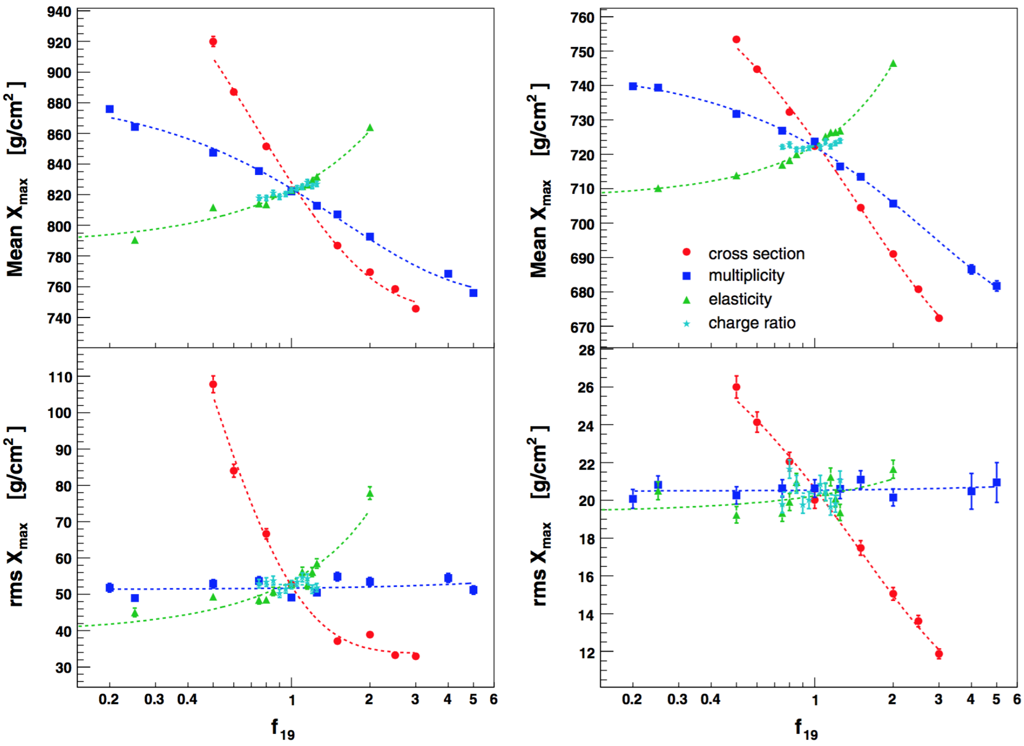

FIGURE 1.6: The mean (top) and the standard deviation (bottom) of X_{max} predicted by SIBYLL2.1, corresponding to $10^{19.5}$ eV proton (left) and iron (right) primaries [19]. Different color lines and markers indicate the influences to the determination of X_{max} and $\sigma(X_{max})$ for each parameters, according to the evaluation by an artificial shifting of corresponding parameter.

of X_{max}. For instance, if the total inelastic cross-section is large, air-shower starts to develop earlier on the top of atmosphere, thus, the showers will have a smaller X_{max}. According to Fig. 1.6, it has the largest impact on X_{max}, shifting the mean value of X_{max} by approximately 100 g/cm^2 for proton and by about 40 g/cm^2 for iron primaries. It also exhibits the largest correction with the fluctuations of X_{max}. The energy fraction of leading particle to the primary particle ($\kappa_{ela} = E_{leading}/E_{primary}$) correlates to the inelasticity which is defined as κ_{inel} = 1 - κ_{ela}. In the nuclear-electromagnetic cascades, the smaller inelasticity means the leading secondary particles carry more energy deep into the atmosphere for the air-shower development, and the corresponding air shower will have a larger X_{max}. It has the second large order of correlation with the fluctuations of X_{max}, especially for proton primaries. Impact of the shifting of X_{max} is smaller than inelastic cross-section and multiplicity. The multiplicity of secondary particle exhibits almost same effects in shifting X_{max}, but small correlation with the fluctuations of X_{max}. On the other hand, the pion charge ratio has no much effect to the both X_{max} shifting and the fluctuations of X_{max}.

In a simple Heitler model, it generalizes the hadronic showers and provides some insights into air shower development [27, 28]. According to this kind of toy model, one can understand how the shower observables are related to the hadronic interaction physics. Figure 1.7 shows the components from the air-shower can be categorised into hadronic and electromagnetic parts. Only the charged hadronic components are related to the muon production. In a hadronic shower, a charged particle with energy E can produce N_{tot} secondary particles with energy E/N_{tot}. If you assume N_{EM} particles transfer their energies to the electromagnetic showers, then the other ones will distribute to hadronic channels. Corresponding evolution will continue as soon as their energy reach to a characteristic energy E_{dec}, where pions decay into muons.

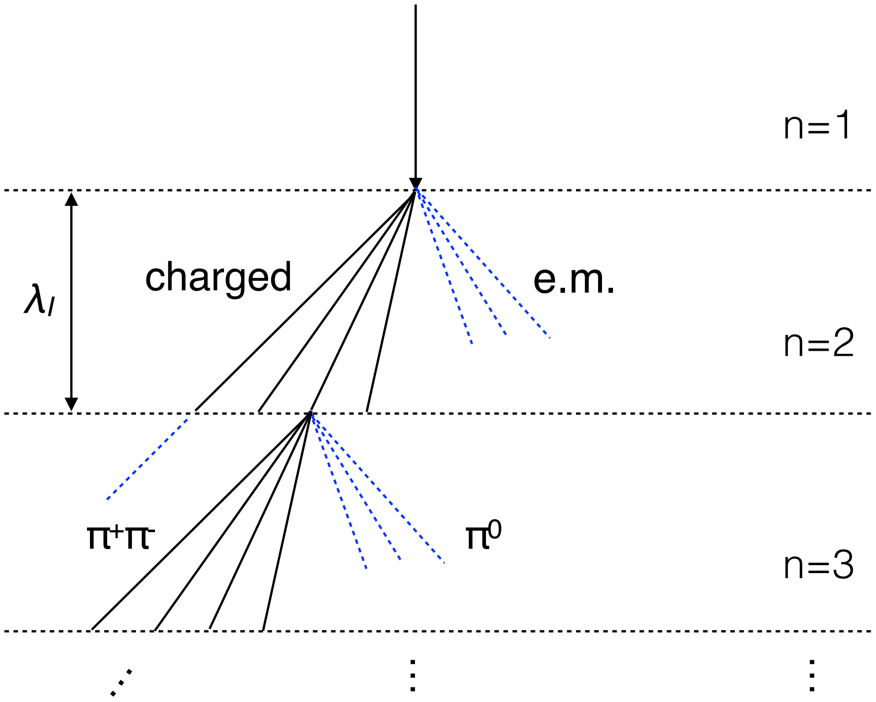

FIGURE 1.7: Heitler model illustrates pion production in air shower.

In a shower produced by a primary particle with energy E_0, the number of muons N_μ after n generations is given as [29]

$$N_u = (N_{tot} - N_{EM})^n = (\frac{E_0}{E_{dec}})^{1+\frac{\ln R}{\ln N_{tot}}}, \tag{1.3}$$

where $R = (N_{tot} - N_{EM})/N_{tot}$. In the pure pion case $R = 2/3$, however, R will not just simply $2/3$ if all kinds of hadrons are considered. Accordingly, R depends on the individual hadrons yields, and the change of R is very sensitive to the number of muons. Figure 1.8 shows the R as a function of x_E, which is the large energy fraction of hadrons. The ratio R is much bigger for p-air collisions compared to π-air collisions, because of the leading baryon effect. In addition, an enhancement of leading baryon production will increase p-air interactions respect to π-air interactions, thus leading to an even larger value of R. Corresponding different dependency between EPOS1.6 and QGSJET01, resulting in the muon density changes approximately 20% at 10^{18} eV [29]. Therefore, the measurement of forward baryon production is very important to solving the "muon excess" problem.

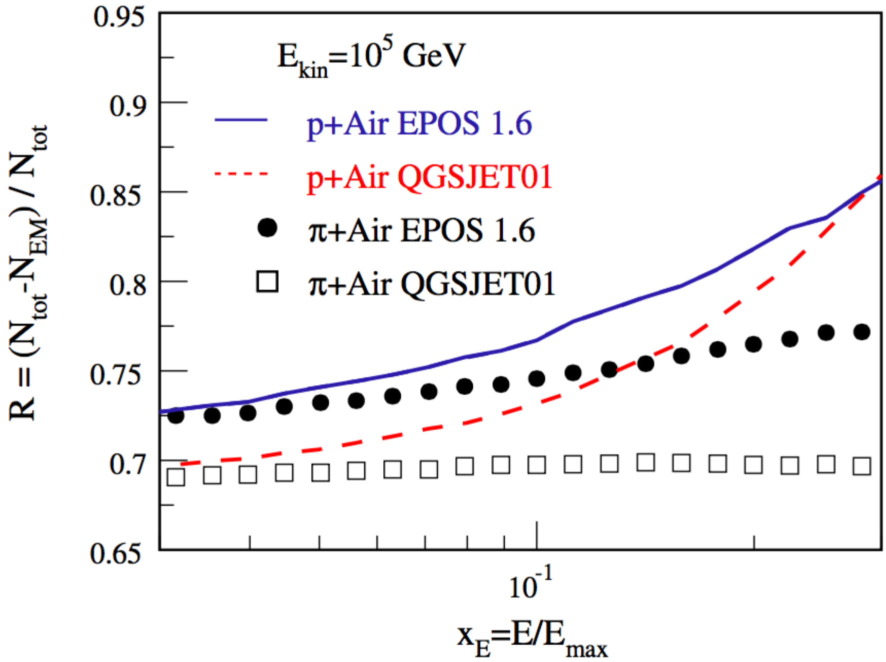

FIGURE 1.8: The ratio $R = (N_{tot} - N_{EM})/N_{tot}$ as a function of energy fraction in p-air collisions and in π-air collisions at 10^5 GeV kinetic energy. Predictions from EPOS 1.6 and QGSJET01 are shown for comparisons [29].

Similar to the X_{max}, the influence of the four key parameters mentioned above was also investigated in a paper [19]. Figure 1.9 shows the mean value and standard deviation of $\log_{10}(\mathrm{N}_\mu)$ predicted by SIBYLL2.1, summarizing the impact by changing each individual key parameter on the muon number. Firstly, we have to keep in mind that SIBYLL2.1 predict ~70% less muons than EPOS1.6. Thus, corresponding difference can not be explained by just changing these key parameters. Modifications of these parameters would lead to an enhancement of muon number by only ~30% [19]. In other word, the forward leading baryon production is still the dominant feature to effect the muon number. According to the simulation results shown in Fig. 1.9, the muon number increases proportional to logarithmic of multiplicity. The pion charge ratio ($r = n_{\pi^0}/(n_{\pi^0} + n_{\pi^+} + n_{\pi^-})$) is very sensitive to the muon production, while have small effect to X_{max}. The dependence on elasticity is $\log_{10} N_\mu \propto$ -κ_{ela}. The fluctuation in $\log_{10} N_\mu$ are dominated by elasticity.

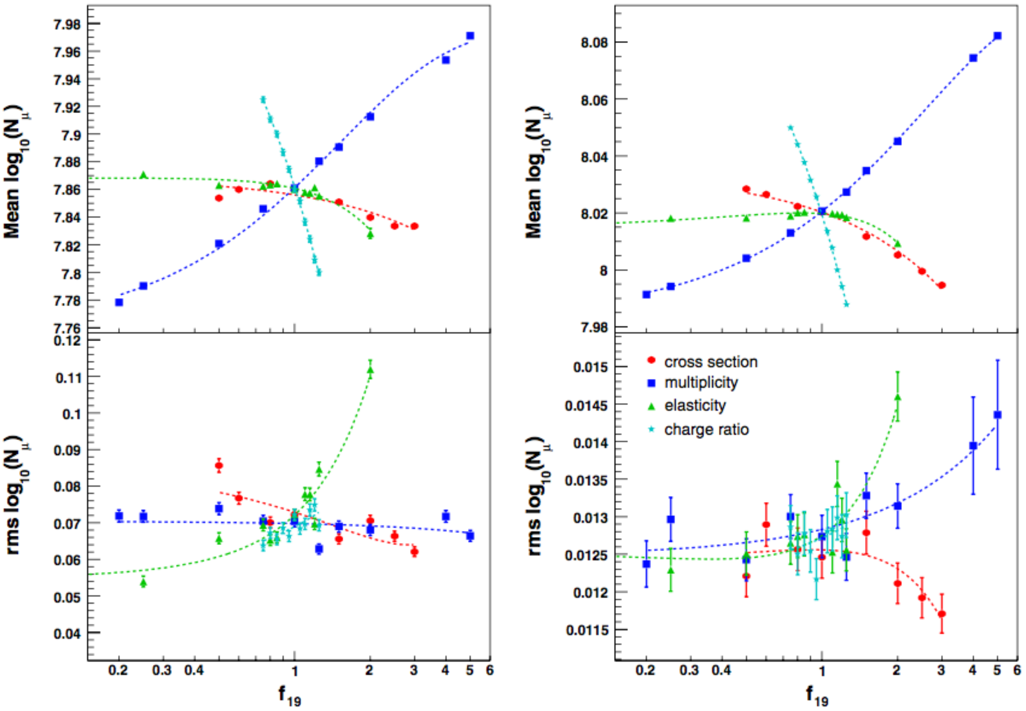

FIGURE 1.9: The mean (top) and the standard deviation (bottom) of $\log_{10}$ (N_μ) predicted by SIBYLL2.1, corresponding to $10^{19.5}$ eV proton (left) and iron (right) primaries [19]. Different color lines and markers indicate the effect of each parameter to the determination of $\log_{10}$ (N_μ) and σ $\log_{10}$ (N_μ) based on an artificial shift in single corresponding parameter [19].

1.2.3 Diffraction in predictions of longitudinal air-shower development

In proton-proton interactions, events can be classified into either elastic or inelastic, inelastic collisions can be furthermore categorized into soft or hard processes. Among typical collision types of soft processes, diffractive processes are still poorly constrained due to the lack of experimental data. Figure 1.10 shows the image of differences of air-shower development between diffraction and non-diffraction collisions. It was mentioned in the previous section, the total inelastic cross-section, inelasticity (k_{inel}), and the forward production spectrum of baryons and mesons play a very important role during the development of air-showers. Once the diffraction takes place in the primary interaction of air-shower development, substantial amounts of energy of the primary particles will transfer deep into the atmosphere. It is known that the diffractive interactions directly effect to the inelasticity [30]. The rate and characteristics of the diffraction turn into critical factors that control the global characteristics of the shower profile. As shown in Fig. 1.11, the original QGSJET-II-04 model was tuned with gaining and reducing the differential cross-section of Single Diffraction (SD) within the size is considerable to the uncertainties. The predicted average X_{max} as a function of primary energy are compared among these three versions of models. Without changing any aspect of the model

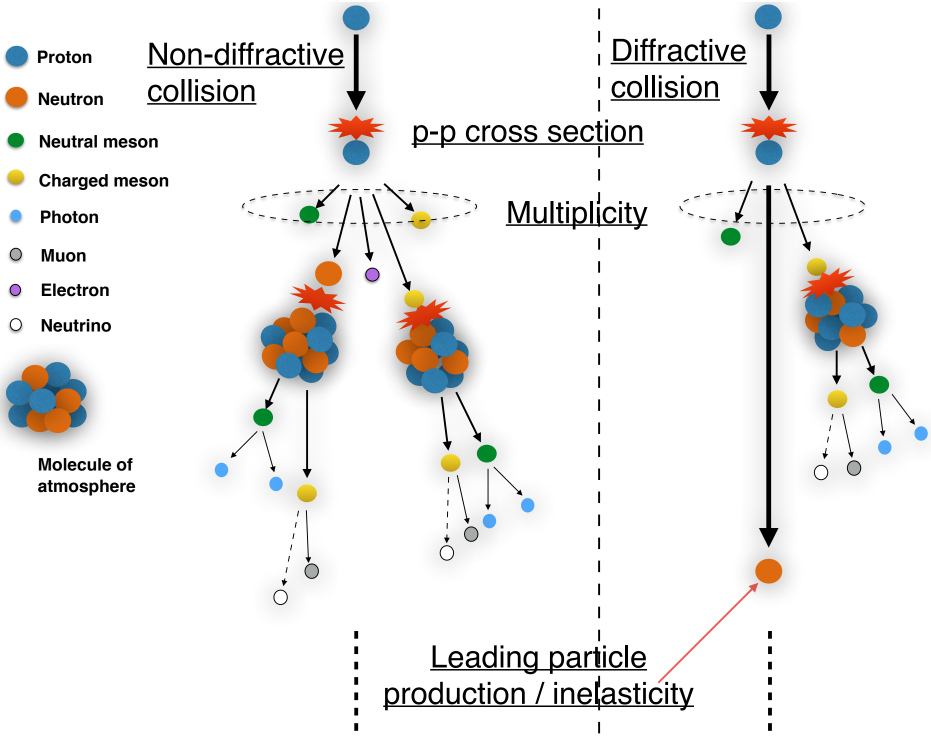

FIGURE 1.10: Image of air-shower development in the atmosphere. Diffractive and non-diffractive collisions between primary cosmic-ray and atmosphere have different kind of development of air-showers.

but only SD cross-section, the two alternative version of models have approximately 10 g/cm^2 differences between each other.

The diffractive events and non-diffractive events are totally different interaction processes and hadronic interaction models describe them separately. Since the approaches of diffraction implemented in the models based on phenomenological model, besides, it is difficult to measure the diffractive processes experimentally, the diffractive interaction is neither theoretically nor experimentally well known yet. Certain fractions of model uncertainties are caused because of the limitation understanding of diffractive processes. Therefore, an adequate understanding of diffractive processes is extremely important for improvement of hadronic interaction models.

1.3 Forward physics at the LHC

1.3.1 Forward measurement at the LHC

In general, there are three methods to measure the forward observables at the LHC based on the minimum bias, Roman Pots (RP) and Zero Degree Calorimeter (ZDC) techniques. Minimum bias method is usually adopted as a part of central detector,

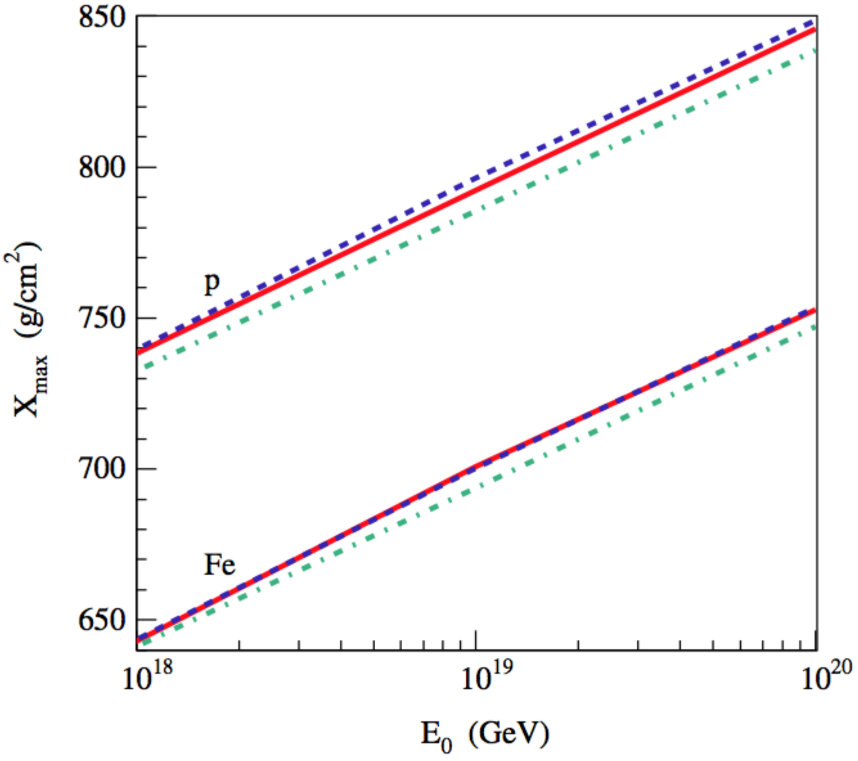

FIGURE 1.11: The average X_{max} calculated by default QGSJET-II-04 model (solid), option SD+ (dashed), and option SD- (dot-dashed) [30].

such as ATLAS [31] and CMS [32], by installing the detector close to the beam pipe in the forward region. For instance, the minimum bias trigger scintillator and forward calorimeters in ATLAS and CASTOR in CMS. They are widely used in the measurements of total and differential cross-section as well as multiplicity, etc.. In proton-proton collisions, RP is a powerful technique to measure total, elastic and inelastic cross-section. The minimum bias method can also be used to measure these cross sections, but it needs the extrapolation of very-forward phase space based on MC predictions. Methodology of total and elastic cross-section measurements by RP based on the optical theorem, which needs extrapolation of the differential cross-section $d\sigma/dt$ to the optical point at the four-momentum transfer squared $t = 0$. The RP system usually installs the proton detector on movable beam-pipe insertions. It is possible to access smaller $|t|$-values via the alignment of the detector to the proton beam to measure the elastic or diffractive protons. TOTEM [33] and ATLAS/ALFA [31] are the two RP experiments at the LHC. ZDC is the detector dedicate to measuring the neutral particles emitted in the very forward regions including zero degree, which is not accessible by neither a minimum bias detector nor a RP detector. It can be used to evaluate the beam luminosity. Besides, the corresponding forward particle production is the most interested data for the studies of cosmic-ray air showers. The detectors are usually installed between two beam-pipe just after their separation. LHCf [34] detector is one of the ZDC detectors at the LHC.

1.3.2 Impact of the forward measurement to the air-shower observation

Accelerator data is capable of constraining the inherent uncertainties of modelling the hadronic interactions between CRs and the atmosphere. After the upgrade of the collision energy, the Large Hadron Collider (LHC) has realised $\sqrt{s} = 13$ TeV the highest energy ever reached by a man-made accelerator. The laboratory equivalent collision energy is approximately 10^{17} eV, which is close to the highest energy of observed UHECRs ($\sim 10^{20}$ eV).

Figure 1.12 shows (a) multiplicity and (b) energy flow as a function of pseudorapidity in p-p collisions at $\sqrt{s} = 13$ TeV. Most of the final state particles are produced in the central rapidity regions covered by ATLAS and CMS detectors. On the other hand, abundant of energy flow ($\sim 50\%$ concentrated on the LHCf acceptance) is emitted in the very forward regions even with a small number of particles. Accordingly, these particles are the most energetic secondaries in the hadronic collisions. As discussion in section 1.2, total cross-section, inelasticity, and forward baryon and meson productions play an important role to the air-shower development. Total cross-section can be precisely measured by TOTEM and ALFA experiments. Since LHCf covers the very forward regions, it is sensitive to the measurement of inelasticity and forward baryon and meson productions (mainly neutron, π^0 and η meson).

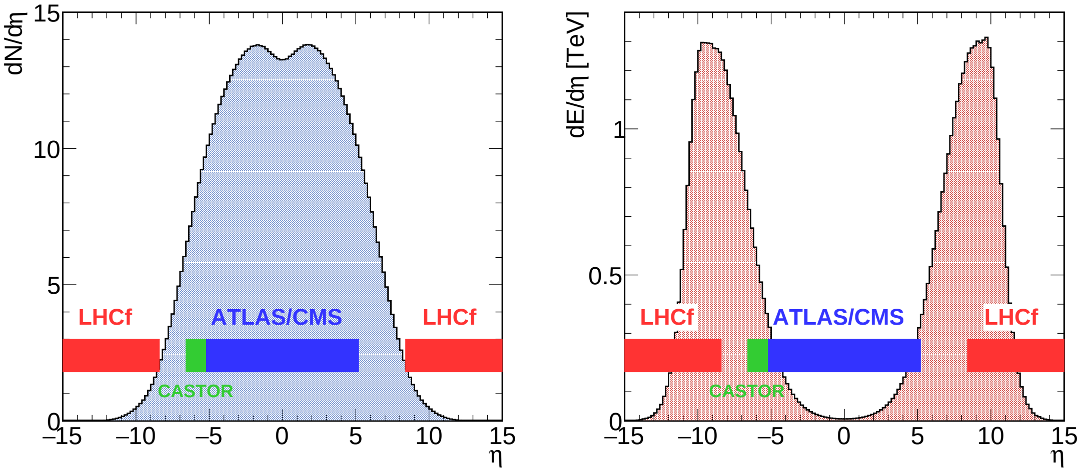

(a) Multiplicity (b) Energy flow

FIGURE 1.12: Multiplicity and energy flow as a function of pseudorapidity in p-p collisions at $\sqrt{s} = 13$ TeV. The color bands corresponding to the detector acceptance.

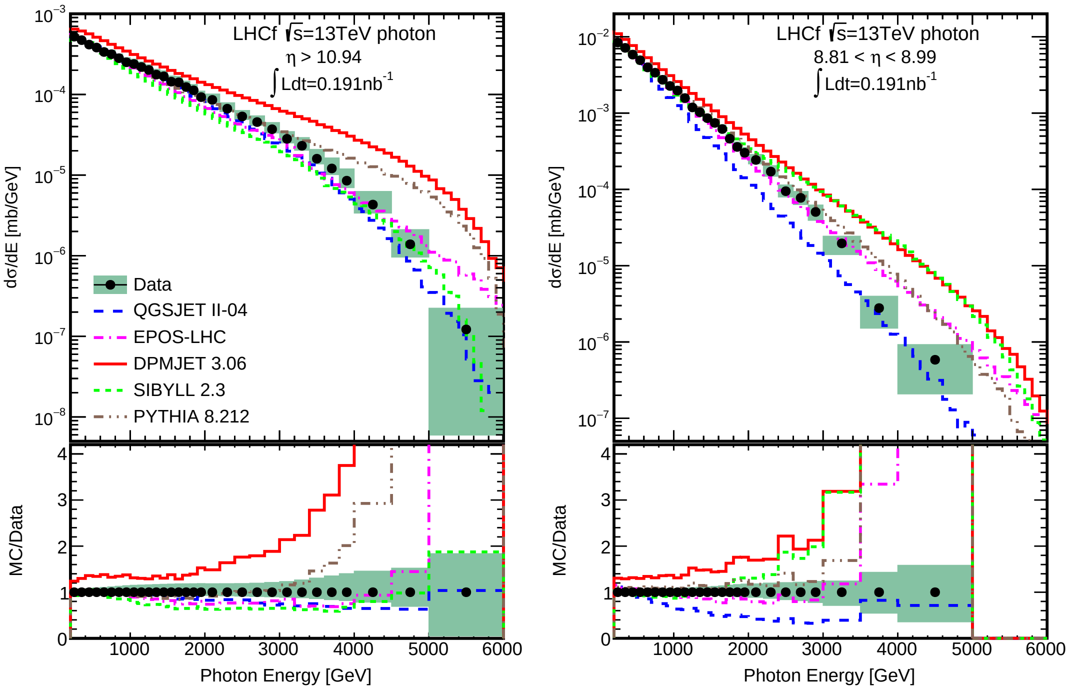

FIGURE 1.13: The photon energy spectra in *p*-*p* collisions at $\sqrt{s} = 13$ TeV. The left and right pads corresponding to the spectra at $\eta > 10.94$ and $8.81 < \eta < 8.99$, respectively. The points associated with green area show the data with systematic uncertainties and colour lines represent the MC predictions [37].

1.3.3 The LHCf experiment

LHCf [34] is a unique experiment dedicated to measuring the neutral particles production cross-section in the very forward region of the LHC. LHCf has so far published the differential cross-section of photons in $\sqrt{s} = 0.9$ TeV [35], 7 TeV [36], and 13 TeV [37] *p*-*p* collisions. The very forward neutron production was measured by LHCf in *p*-*p* collisions at $\sqrt{s} = 7$ TeV [38] and 13 TeV [39], as well as the differential cross-section of neutral pions have been measured in *p*-*p* collisions at $\sqrt{s} = 2.76$ TeV, and 7 TeV and in *p*-*Pb* collisions at $\sqrt{s_{NN}} = 5.02$ TeV [40–42]. The designed purpose of LHCf is to take data in *p*-*p* collisions at 13 TeV. From 10^{th} to13^{th}, June 2015, LHCf has succeed the operation in $\sqrt{s}$ =13 TeV proton-proton collisions at the LHC. Meanwhile, the operation was scheduled for 5 days with very low luminosity $\sim 10^{29} cm^{-2} s^{-1}$, and collaborated with the ATLAS experiment. The first physics analysis has already been published. These data-sets allow to test and improve the hadronic interaction models in a very wide energy range.

Figure 1.13 and 1.14 shows differential cross-section of photons and neutrons in *p*-*p* collisions at $\sqrt{s} = 13$ TeV measured by LHCf, respectively. Photon cross-section at $\eta >$ 10.94 and $8.81 < \eta < 8.99$, and neutron cross-section at $\eta > 10.94$, $8.99 < \eta < 9.22$, and

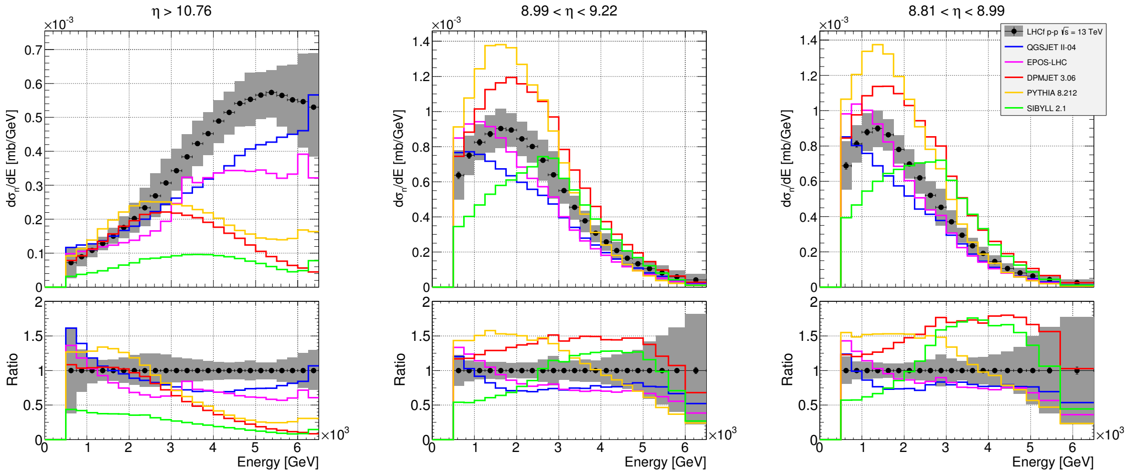

(a) $\eta > 10.94$ (b) $8.99 < \eta < 9.22$ (c) $8.81 < \eta < 8.99$

FIGURE 1.14: The neutron energy spectra in p-p collisions at $\sqrt{s} = 13$ TeV measured by LHCf Arm2 detector. The left, middle, and right pads corresponding to the spectra at $\eta > 10.94$, $8.99 < \eta < 9.22$, and $8.81 < \eta < 8.99$, respectively. The markers associated with grey area show the data with systematic uncertainties and colour lines represent the MC predictions [39].

$8.81 < \eta < 8.99$ are compared with the predictions of pre and post LHC models. No MC simulation model predicts the experimental data perfectly. The post-LHC models, EPOS-LHC and QGSJET-II-04 which are widely used in the air-shower experiments, have roughly agreement with the data by comparing with the other models. On the other hand, PYTHIA8 which is widely used for the simulations of high-energy collisions in collider experiments, it does not reproduce the LHCf data well, especially, for the neutron production cross-section. It is mainly because the predictions of the particle production in LHCf phase space dominated by phenomenological models, besides, the lack of data for the tuning of soft interaction processes.

1.3.4 The ATLAS-LHCf common experiment

Diffractive dissociation contributes approximately 25-30% of the inelastic cross section in p-p collisions. The forward neutral particle production measured by LHCf is inclusive cross-section, which contains the particles derived from diffractive and non-diffractive processes. Because the diffractive contribution to forward particle production is still a unknown phenomenon, and it plays an extremely important role to control the global characteristics of air-shower profile development, it is necessary to identify the LHCf observables either as diffraction or as non-diffraction at event-by-event basis. The categorized LHCf data would be powerful to provide more specific constraints to inherent uncertainties of the modelling of hadronic interactions.

The ATLAS-LHCf common experiment is designed to measure the diffractive dissociation in the $\sqrt{s}$=13 TeV p-p collisions. Hereby, the common data acquisition with ATLAS could explore the potential of the data from both experiments. ATLAS could provide the central particle production data to classify the LHCf observables into diffraction and non-diffraction. On the other hand, ATLAS can analyze the differences of central particle production between with and without LHCf trigger. In addition, there is still no direct measurement for the observations of low mass diffractive dissociation. since, the ATLAS-LHCf common experiment has unique sensitivity to such low-mass diffraction, it can provide the world's first low-mass diffraction data.

1.4 Introduction to this research

In Chapter 2, the detail description and theoretical approach implemented in the models of diffractive dissociation are discussed. Current status of measurement of diffraction is introduced. Then we discuss the motivation of the ATLAS-LHCf common experiment.

In Chapter 3, an introduction about the LHCf experiment is described in detail. In particular, the framework of common data acquisition and the development of new trigger system for the common experiment is discussed. The main issue of new trigger system, and the strategy of how to solve them are explained.

In Chapter 4, firstly, the differences of diffractive contribution to the forward particle production are investigated by comparing the simulation predictions. Then, we exploit a method to classify the LHCf observables into diffractive and non-diffractive interactions at event-by-event bias based on the ATLAS rapidity gap data. The performance of this method and the corresponding sensitivity of ATLAS-LHCf common experiment are evaluated. Finally, we also discuss the possibility of identification of diffractive events to further single and double diffractions by using the ATLAS minimum bias trigger scintillator data.

In Chapter 5, we discuss how the first ATLAS-LHCf joint analyses are proceeded. Forward photon differential cross-section derived from low-mass diffractive interactions is analyzed and compared with several MC predictions.

In Chapter 6, the discussion about the key parameter to the implementation of diffractive dissociation is carried out based on a tuning work of SIBYLL2.3c. We also investigate how is the diffractive dissociation effect to the air-shower development and evaluate the impact to the mass determination of UHECRs. Finally, we discuss the future prospects of the ATLAS-LHCf joint analyses for solving the "muon excess" problem.

At last, the conclusion from these results is summarized in Chapter 7.

Chapter 2

Diffractive dissociation

2.1 Diffractive dissociation

In high-energy proton-proton interactions, Regge theory describes diffractive processes as a t-channel reaction, which is dominated by the exchange of an object with vacuum quantum numbers called *pomerons* [43]. The total diffractive interactions contribute approximately 25-30% of the total inelastic cross section at the LHC energies. A general definition of hadronic diffractive processes can be summarized as follow:

- At high energies, an interaction in which no quantum numbers are exchanged between the two colliding particles is a diffractive reaction.
- A diffractive interaction can be characterized by a large, non exponentially suppressed, rapidity gap in the final state [44]. Here the rapidity gap is defined as a rapidity region where no final state particle is produced.

According to the signature of final state particles, it is usually recognized that diffractive processes are composed of single-diffraction (SD; Fig. 2.1a), double-diffraction (DD; Fig. 2.1b), and central-diffraction (CD; Fig. 2.1c) terms. The CD (in some models, it is double-pomeron exchange process) is a more complex interaction, and its rate is suppressed by the SD process at high energies [44]. In the SD case, the scattered proton flies to the very forward angle, at the same time, the other proton breaks to several secondary particles which also consentrate in the forward region. An operational characteristic of diffractive interactions is the large angular separation between the final state systems called the rapidity gap $\Delta\eta$. The size and location of $\Delta\eta$ in pseudorapidity phase space can be used to determine the type of diffraction.

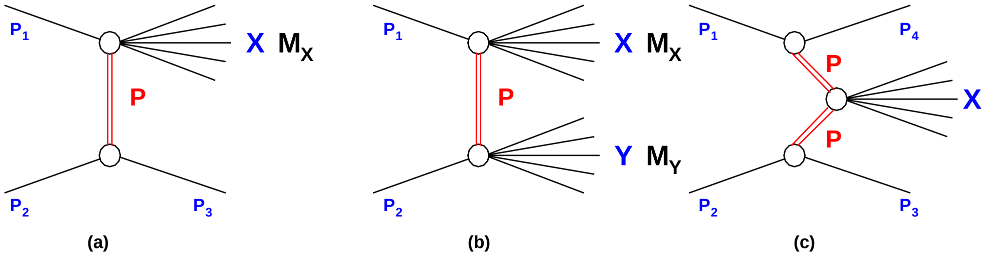

FIGURE 2.1: Schematic illustration of (a) single diffraction, (b) double diffraction, and (c) central diffraction with the pomeron exchanged in a proton-proton collision. M_X and M_Y are the invariant masses of the dissociated systems X and Y.

As illustrated in Figure 2.1 (a), for the single diffractive reactions, the invariant mass (M_X) of the X system which is so-called diffractive mass can be defined as.

$$M_X^2 = (\mathbf{p_1} + \mathbf{p_2} - \mathbf{p_3})^{\mathbf{2}}, \tag{2.1}$$

Here **p1**, **p2** and **p3** mean the four momenta of the incoming particles and the outgoing particle without dissociation. In the center of mass (CM) system the four-momenta of these three particles can be written as,

$$\begin{aligned} \mathbf{p_1} &= (E_1, \mathbf{p}) = (E_1, 0, 0, p_z), & (2.2)\\ \mathbf{p_2} &= (E_2, -\mathbf{p}) = (E_2, 0, 0, -p_z), & (2.3)\\ \mathbf{p_3} &= (E_3, \mathbf{p}') = (E_1, \mathbf{p}_\perp, p'_z). & (2.4) \end{aligned}$$

The term of the CM energy squared s can be written as

$$s = (\mathbf{p_1} + \mathbf{p_2})^2. \tag{2.5}$$

In the high energy limit ($s \to \infty$) the masses can be neglected,

$$\begin{aligned} |\mathbf{p}| &= p_z \simeq \frac{\sqrt{s}}{2}, \quad E_1, E_2 \simeq \frac{\sqrt{s}}{2}, & (2.6)\\ |\mathbf{p}'| &\simeq \frac{s - M_X^2}{2\sqrt{s}}, \quad E_3 = \frac{1}{2\sqrt{s}}(s + m_3^2 - M_X^2) \simeq \frac{s - M_X^2}{2\sqrt{s}}. & (2.7) \end{aligned}$$

For a particle of energy E and the momentum p_z along the z-axis, the rapidity is defined as

$$y = \frac{1}{2} ln \frac{E + p_z}{E - p_z}. \tag{2.8}$$

Here, the transverse mass $m_\perp$ is defined as

$$m_\perp = \sqrt{m^2 + \mathbf{P^2_\perp}}, \tag{2.9}$$

$$E = \sqrt{m^2_\perp + p^2_z}. \tag{2.10}$$

For the particles ($p_z \gg m$) the rapidity equation 2.8 becomes

$$y \simeq ln\frac{2p_z}{m_\perp}. \tag{2.11}$$

Coming back to the single diffractive process, as the pseudorapidity distribution illustrated in Figure 2.2, when $\mathbf{p}_\perp$ is 0 and M_X is 0, according to 2.4, 2.7, 2.9 and 2.11 the maximum value of rapidity of the outgoing particle 3 is

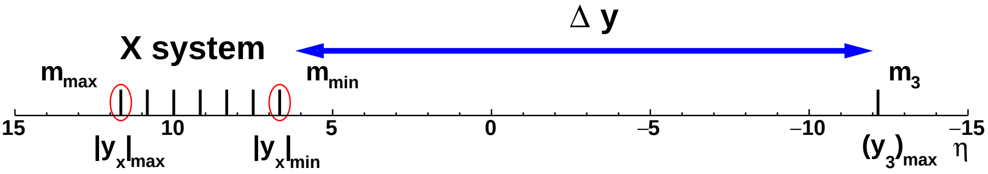

FIGURE 2.2: Pseudo-rapidity distribution image of single diffractive dissociation. The X system consists of many secondary particles produced by the incident particle.

$$(y_3)_{max} \simeq ln\frac{\sqrt{s}}{m_3}. \tag{2.12}$$

As for the system X, same as $(y_3)_{max}$, $|y_X|_{max} \simeq ln\frac{\sqrt{s}}{m_{max}}$. Here m_{max} is the mass of the particle determining the $|y_X|_{max}$ in the X system. Whereas the minimum value can be defined as

$$|y_X|_{min} \simeq ln\frac{m_{min}\sqrt{s}}{M^2_X}, \tag{2.13}$$

for the particle with momentum $\sim (m/M_X)\sqrt{s}/2$ and the transverse mass $\sim M_X$. Here m_{min} is the mass of the particle having the smallest rapidity.

Finally, the rapidity gap between the particle 3 and the edge of the rapidity distribution of the X system is given by

$$\triangle y \simeq ln\frac{\sqrt{s}}{m_3} + ln\frac{m_{min}\sqrt{s}}{M^2_X}. \tag{2.14}$$

For the massless particles and the case $|\mathbf{p}_\perp| \gg m$, it can be written as

$$\triangle y \simeq ln\frac{s}{M^2_X}. \tag{2.15}$$

As the rapidity gap $\triangle\eta$ indicated by Equation 2.15, in the diffractive process, the larger rapidity gap observed in the experiment, the lower diffractive mass M_X produced in this collision. In the SD case, it is known that the relationship between the observables $\Delta\eta$ and ξ_X is shown as equation below, according to Equation 2.15.

$$\Delta\eta \simeq -\ln(\xi_X), \tag{2.16}$$

where $\xi_X = M_X^2/s$ with $\sqrt{s}$ being the total energy in the center-of-momentum frame.

In the frame of Reggeon Field Theory, the high-mass diffractive dissociation ($s \gg M_X^2 \gg |t|$) is conventionally described by enhanced multi-Pomeron diagrams [45], with parameterizing the term of triple-Pomeron coupling. Simply, without considering the absorptive corrections, the SD cross section can be expressed as

$$\frac{d\sigma^{SD}}{d\xi_X dt} = f_{\mathbb{P}}(\xi_X, t)\sigma_{\mathbb{P}}(M_X^2) = \frac{1}{16\pi}\beta^2(t)\xi_X^{1-2\alpha_{\mathbb{P}}(t)}[\beta(0)G_{3\mathbb{P}}(t)(M_X^2)^{\alpha_{\mathbb{P}}(0)-1}]. \tag{2.17}$$

The term of $f_{\mathbb{P}}(\xi_X, t) = \frac{1}{16\pi}\beta^2(t)\xi_X^{1-2\alpha_{\mathbb{P}}(t)}$ represents the pomeron flux, and $\sigma_{\mathbb{P}}(M_X^2) = \beta(0)G_{3\mathbb{P}}(t)(M_X^2)^{\alpha_{\mathbb{P}}(0)-1}$ is the cross section of pomeron, where $\beta(t)$ is the coupling of the Pomeron and dissociating proton. $G_{3\mathbb{P}}(t)$ is the triple-Pomeron coupling. $\alpha_{\mathbb{P}}(t)$ is the Pomeron trajectory which is given by

$$\alpha_{\mathbb{P}}(t) = \alpha_{\mathbb{P}}(0) + \alpha'_{\mathbb{P}}t = 1 + \Delta + \alpha' t. \tag{2.18}$$

The default value of variable parameters Δ and α' are 0.085 and 0.25 GeV^{-2} [46], respectively. The σ^{SD} is a fraction of the total cross section which as the expectation of Regge theory $\sigma^{tot} \sim s^{\Delta}$, $\sigma^{SD} \sim s^{2\Delta}$, and $\sigma^{SD}/\sigma^{tot} \sim s^{\Delta}$. An intercept $\alpha_{\mathbb{P}}(0) = 1 + \Delta$ represents the soft pomeron, can be obtained from the fits to cross section data. The growth of total and diffractive dissociation cross section are reduced by the contribution of the intercept term, otherwise the theoretical prediction would rise quicker than the measurement data. The triple-Pomeron coupling $G_{3\mathbb{P}}(t)$ can be also obtained from a fit of measurement data. In the lower energies, the fit result indicates that it is almost independent of t [47], so that $G_{3\mathbb{P}}(t) \simeq G_{3\mathbb{P}}(0)$. However, $G_{3\mathbb{P}}(t) \simeq G_{3\mathbb{P}}(0)$ is inadequate to describe the high energy data, for instance, the partial cross sections of high-mass diffractions would be overestimated in the LHC energies by using the $G_{3\mathbb{P}}(t)$ constrained based on the low energy data. Importantly, the number of multiple interactions grows as the energy increases. It is necessary to include the absorptive corrections to keep the theoretical consistency of the approach, for instance the s-channel unitarity, otherwise the diffractive cross section would rise quicker than the total cross section [48]. On the other hand, the low-mass diffractive dissociation is usually described by using the optimized Good-Walker approach[49], which uses multi-channel eikonal model to describe a set of elastic scattering eigenstates, as each eigenstate corresponds to a simple one-channel eikonal. The partial cross sections of low-mass diffractive dissociations are related to the assumption of Pomeron-hadron coupling.

2.2 Current status of diffraction measurement

The rapidity gap distributions in p-p collisions at $\sqrt{s}$ =7 TeV have already been measured by ATLAS based on the minimum bias trigger data. Figure 2.3 shows the differential cross sections as a function of rapidity gap $\triangle\eta^F$ compared with several MC predictions. The different colour of the histograms shown in (a), (b) and (c) of Fig. 2.3 corresponding to the different types of diffractions identified according to the flags from the MC models. Maximum rapidity gap, $\triangle\eta^F = 8$, which comes from the limit pseudorapidity of the ATLAS sensitivity ($\eta = \pm 4.9$). Hereby, $\triangle\eta^F$ is measured mainly by the tracking system; MBTS and FCal detectors of ATLAS. Fiducial regions of this measurement are $0 < \triangle\eta^F < 8$ and $p_T > 200$ MeV. The uncertainties of this $\triangle\eta^F$ measurement are different depending on the ranges of $\triangle\eta^F$, they are typically less than 8% for $\triangle\eta^F > 3$ and reach to around 20% at $\triangle\eta^F = 1.5$.

Partial cross sections of high-mass diffractive dissociations were measured by ATLAS [50, 51], CMS [52, 53], and ALICE [54] Collaborations at Large Hadron Collider (LHC) energies. For instance, partial inelastic cross sections as a function of ξ_{Cut} have been measured by ATLAS are shown in Figure 2.4, where ξ_{Cut} indicates the rapidity gap size from 0 to an cut variable (refer to Equation 2.16). The limit range of measured differential cross sections is up to $\xi_{Cut} \sim 10^{-5.5}$, due to the limited acceptance of ATLAS detector. For obtaining the overall inelastic cross section, the cross section of low-mass diffractive dissociation is estimated by extrapolation based on MC simulations.

The cross section of low-mass diffraction ($M_X < 3.4$ GeV) was reported by the TOTEM collaboration, 2.62 ± 2.17 mb [55], at $\sqrt{s} = 7$ TeV. The methodology of measuring the cross section of low-mass diffraction by TOTEM is to subtract the differential cross sections based on minimum bias measurement from the overall inelastic cross section. Therefore, the corresponding cross section of low-mass diffraction is from indirect measurement.

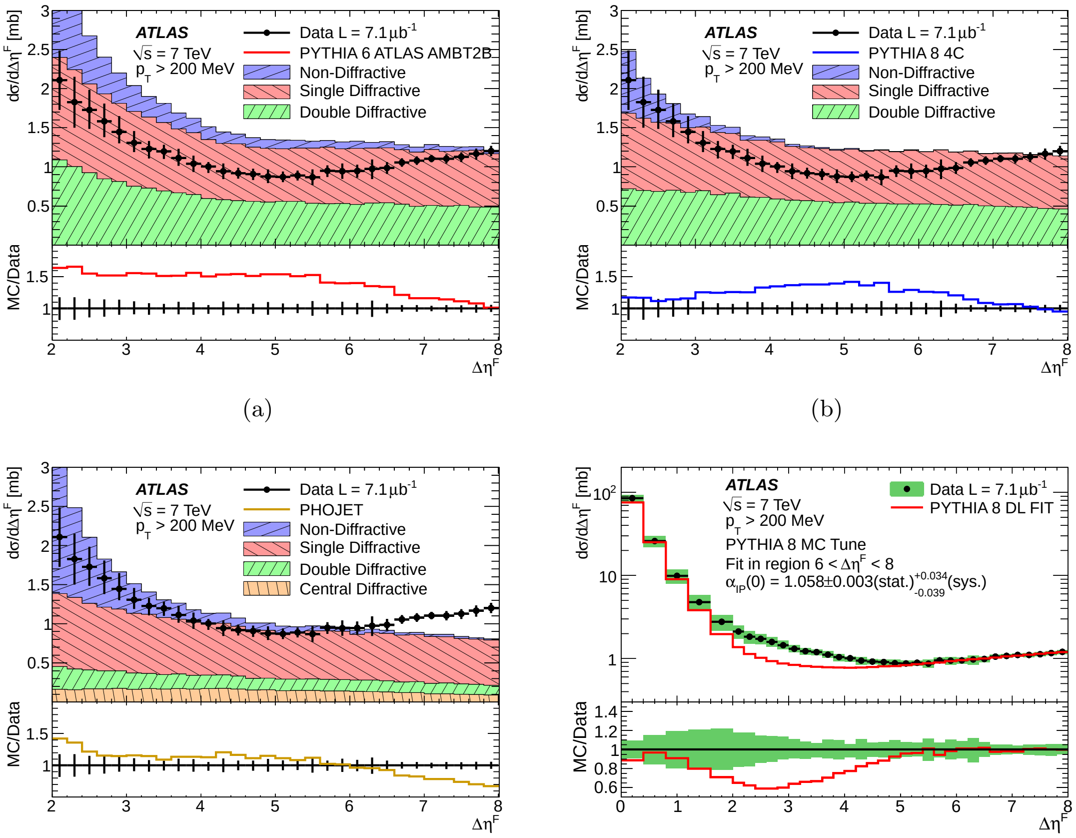

(a) (b) (c) (d)

FIGURE 2.3: Cross-section of rapidity gap measured with the ATLAS detector in p-p collisions at $\sqrt{s}$=7 TeV. Inelastic differential cross-section shown as a function of forward gap size $\triangle\eta^F$ for particles with $p_T > 200$ MeV. The hatched area indicates the total uncertainties. The full lines represent the MC simulations by using PHOJET and the default versions of PYTHIA6 and PYHTIA8. The dashed lines show the different contributions of the SD, DD and ND processes according to the models [50].

2.3 Background of the LHCf-ATLAS common experiment

Diffractive and non-diffractive interactions are very different mechanisms in hadronic collisions. The ideal observation of diffractive processes is to measure all final state particles based on an omnidirectional detector. Since there is no such detector existed until now, combined measurement between the central detector and the forward detector can contribute to the observation of diffractive processes, such as the ATLAS-LHCf and CMS-TOTEM apparatus.

As mentioned in previous section, the measurement of diffractive collisions including the identification of rapidity gaps and the observations of dissociation system. Limitation of rapidity gap measurement comes from the pseudorapidity acceptance of central detector. Since the production of dissociating system concentrate on the very forward direction of the collisions, it is also difficult to measure the production due to the limitation of

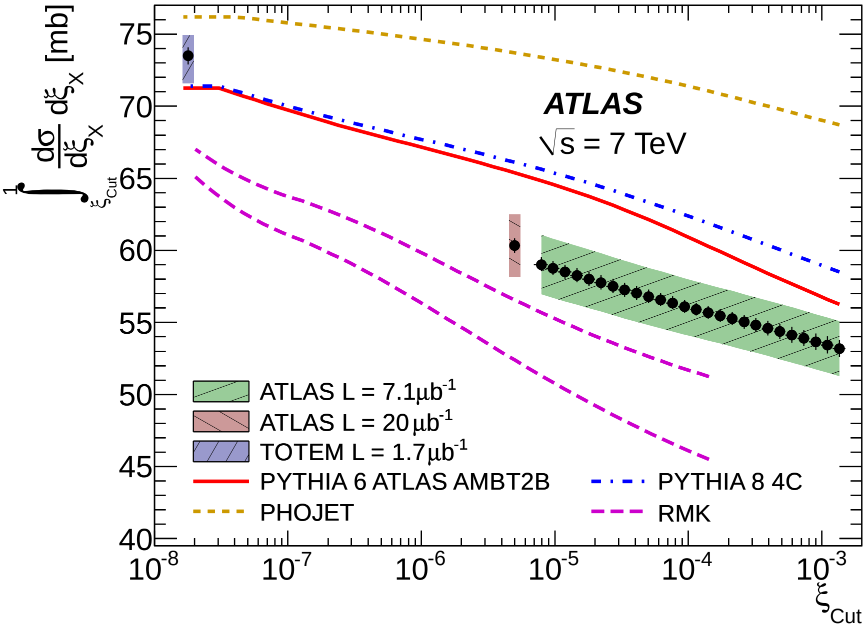

FIGURE 2.4: Inelastic cross-section shown as a function of $\xi_X < \xi_{Cut}$. It is calculated by integrating the differential cross-section from rapidity gap sizes of zero to a certain variable, excluding the diffractive dissociation with $\xi_X < \xi_{Cut}$. The results are carried out by using the data measured by ATLAS detector at $\sqrt{s} = 7$ TeV (ATLAS L = 7.1 μb^{-1}). TOTEM results and ATLAS results from different data set are shown as references at different integration ranges.[50].

forward detector acceptance. Here, one of the powerful apparatus for the diffraction measurement is the ATLAS-LHCf common experiment. Because LHCf can cover the most forward region of $|\eta| > 8.4$ and ATLAS has sensitivity to the central region $|\eta| < 5$, the LHCf-ATLAS common experiment complements the pseudorapidity coverage of two experiments. Especially, the common experiment is capable of measuring the low-mass diffractions, which are expected to have a large $\triangle\eta$ in the rapidity distribution. In the current setup of independent ATLAS and LHCf experiments, ATLAS do not have sensitivity to such low-mass diffractive events, besides, LHCf can detect the low-mass diffractive events but they are mixed together with the other events. Owing to the LHCf trigger system was treated as a part of ATLAS trigger system, the common experiment can use the sensitivity of low-mass diffraction of LHCf to detect such events, and use ATLAS data to identify these events. The common experiment can provide the first direct experimental data of low-mass diffraction at the LHC energies. In addition, the low mass diffractive dissociation is the effective process that can control the development of air shower into the very deep place of atmosphere. In other words, the higher rate of low-mass diffractive dissociation in hadron collisions, the larger X_{max} in the air shower development.

Though the total inelastic cross section is precisely measured by the TOTEM and ATLAS ALFA experiments using the Roman Pot (RP) technique [33, 56], the cross section fractions among non-diffractive, high-mass diffractive, and low-mass diffractive dissociations are still open questions in the hadronic process. Very forward (VF) detectors, covering zero-degree collision angles, have unique sensitivity to low-mass diffractive processes. Accordingly, applying the rapidity gap information based on central detector, it is possible to access pure low-mass diffractive processes. Such forward particle cross sections derived from the pure low-mass diffractive cases can provide an opportunity for constraining hadronic interaction models relevant for air shower development. The ATLAS-LHCf common experiment is dedicated to measuring and classifying diffractive dissociation. The common experiment can not only enhance the trigger efficiency for inelastic processes but also address some specific processes with each other's tagging information.

2.3.1 Acceptance of ATLAS and LHCf detector

In this thesis, parts of the ATLAS detector [56] and the LHCf detectors [57] located at interaction point 1 (IP1) of the LHC are considered to be representatives of the central detectors and VF detectors, respectively.

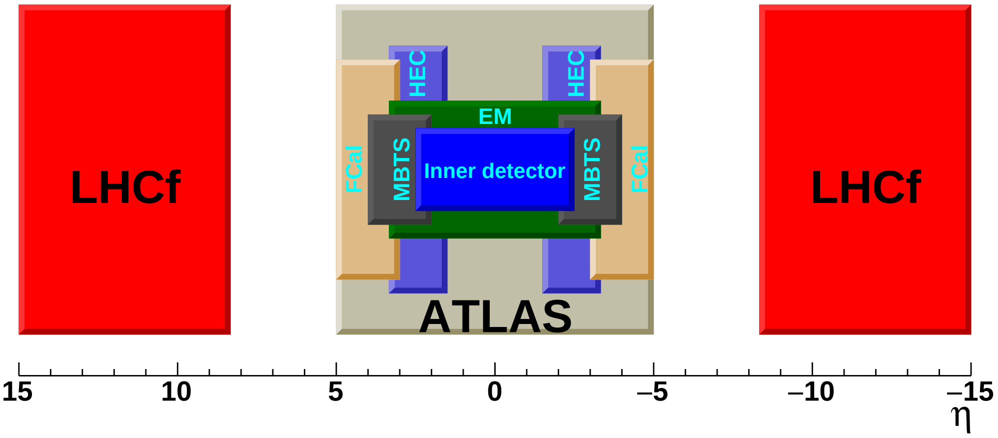

FIGURE 2.5: Pseudo-rapidity acceptance image of ATLAS and LHCf detectors

The ATLAS experiment and the LHCf experiment are located around IP1. As shown in Fig. 2.5, ATLAS is composed of the central tracking system so-called inner detector (ID, $|\eta| \leq 2.5$), ElectroMagnetic liquid argon sampling calorimeters (EM, $|\eta| \leq 3.2$). It also consists of hadronic end-cap (HEC, $1.5 \leq |\eta| \leq 3.2$), forward calorimeters (FCal, $3.1 \leq |\eta| \leq 4.9$) and the muon spectrometers (MS, $|\eta| \leq 2.7$) accord to [56]. The ID measures particle momentum and vertex information with full azimuthal (ϕ) and $|\eta| < 2.5$ pseudorapidity coverage. For studies of minimum-bias measurements, this detector can provide information on charged tracks with a p_T threshold as low as 100 MeV. In addition, the Minimum Bias Trigger Scintillator (MBTS) detectors are widely used for minimum bias measurement. MBTS are mounted in front of the end-cap calorimeters on both sides ($2.1 \leq |\eta| \leq 3.8$). It consists of inner and outer rings. There are LUCID detectors for measuring relative luminosity, using Cerenkov Imaging Detector located at 17 m from IP1, covering $5.6 < |\eta| < 6.0$. By contrast, the ALFA (Absolute Luminosity for ATLAS) detectors [56] are roman pot detector located at ± 237 m from IP1 made of scintillating fibers. The main purposes of them are measuring elastic scattering parameters, the total cross section and the studies of diffraction.

The LHCf detectors were installed in the target neutral absorber (TAN) located ±140 m from IP1. The detectors were designed to measure forward neutral particles (e.g., neutrons, photons, and π^0s) over a pseudorapidity range $|\eta| > 8.4$. The photon and hadron energy thresholds are 200 and 500 GeV, respectively.

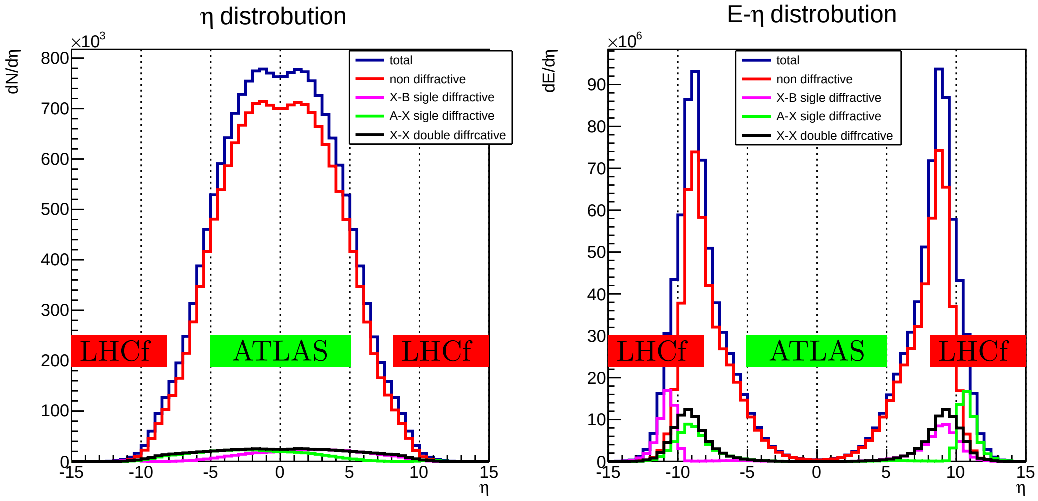

FIGURE 2.6: Pseudo-rapidity distributions for particle density and energy flow in p-p inelastic collisions at $\sqrt{s}$ = 13 TeV predicted by the PYTHIA8185 model. The events was classified by non diffractive, X-B single diffractive, A-X single diffractive, X-X double diffractive. The covered pseudo-rapidity regions by various detectors are shown.

Figure 2.6 indicates multiplicity (left) and energy flow (right) of the secondary particles as a function of pseudorapidity in $\sqrt{s}$=13 TeV proton-proton collisions. Blue, red, magenta, green and black histograms correspond to the particles originated from non-diffraction, X-B (X: dissociating system, B: projectile proton) single diffraction, A-X (X: dissociating system, A: target proton) single diffraction and double diffraction, respectively. The red and green horizontal bars illustrate the pseudorapidity coverages of the LHCf and ATLAS experiments, respectively. The central detectors such as ATLAS and CMS see most of the charged particles from the final states of collisions with a pseudorapidity $|\eta| < 5$, but still a significant amount of particles escape above η= 5. Moreover, most of the energy flow of the final state particles emitted in the very forward regions beyond their reach. Therefore, the central detector cooperates with forward instrumentations are expected to contribute to the diffraction physics.

LHCf has so far published the photon and neutron spectra in proton-proton collisions at $\sqrt{s}$=7 TeV [36, 38]. There is no model reproducing the LHCf results perfectly. To investigate why these differences exist in the previous results, the different contributions from the diffractive and non-diffractive processes are considerable effect. Therefore, it is necessary to investigate the influence of diffraction to the LHCf observables by the ATLAS-LHCf joint analyses.

Chapter 3

The LHCf experiment

3.1 The Large Hadron Collider

The Large Hadron Collider (LHC) [58] is the world's largest man-made particle accelerator which can accelerate the particle to the centre-of-mass energy $\sqrt{s} = 14$ TeV. It is the most powerful tool to test the Standard Model (SM) and to explore the new particle beyond the SM in high energy particle physics. Meanwhile, it also provides multiple usage for the study of phenomenon in high-energy particle physics and heavy ion physics. For instance, one of the big achievement obtained by LHC is that it found the last piece of SM particles, the Higgs particle in 2012. As shown in Fig. 3.1, the LHC is a circular hadron collider with a 27 kilometers tunnel in circumference. The tunnel contains two parallel beam pipes to let the beams accelerated in the opposite directions. 1232 dipole magnets keep the beams accelerated on their circular path, while another 392 quadrupole magnets are used to keep the beams focused. The maximum number of beam bunches is 2808, so the bunch crossing rate is 40 MHz at maximum. There are four interaction points which are (Interaction Point:IP) IP1, IP2 IP5, IP8. The four big experiments are located at these points, which are ATLAS (A Toroidal LHC Apparatus), ALICE (A Large Ion Collider Experiment), CMS (Compact Muon Solenoid), LHCb (LHC beauty). The other three smaller experiments are LHCf (LHC forward), TOTEM(Total Cross Section,Elastic Scattering and Diffraction Dissociation) and MoEDAL (Monopole and Exotics Detector At the LHC). After the injection, the proton beams are firstly accelerated by the Proton Synchrotron Booster, then the Proton Synchrotron, and the Super Proton Synchrotron (SPS). The protons will be accelerated from 50 MeV to 450 GeV in SPS, then injected to the LHC rings from SPS and accelerated up to 14 TeV at maximum. Under the designed full operating power, it can collide proton beams at centre-of-mass energy of 14 TeV with a peak luminosity of $\mathcal{L} = 10^{34}\text{cm}^{-2}\text{s}^{-1}$.

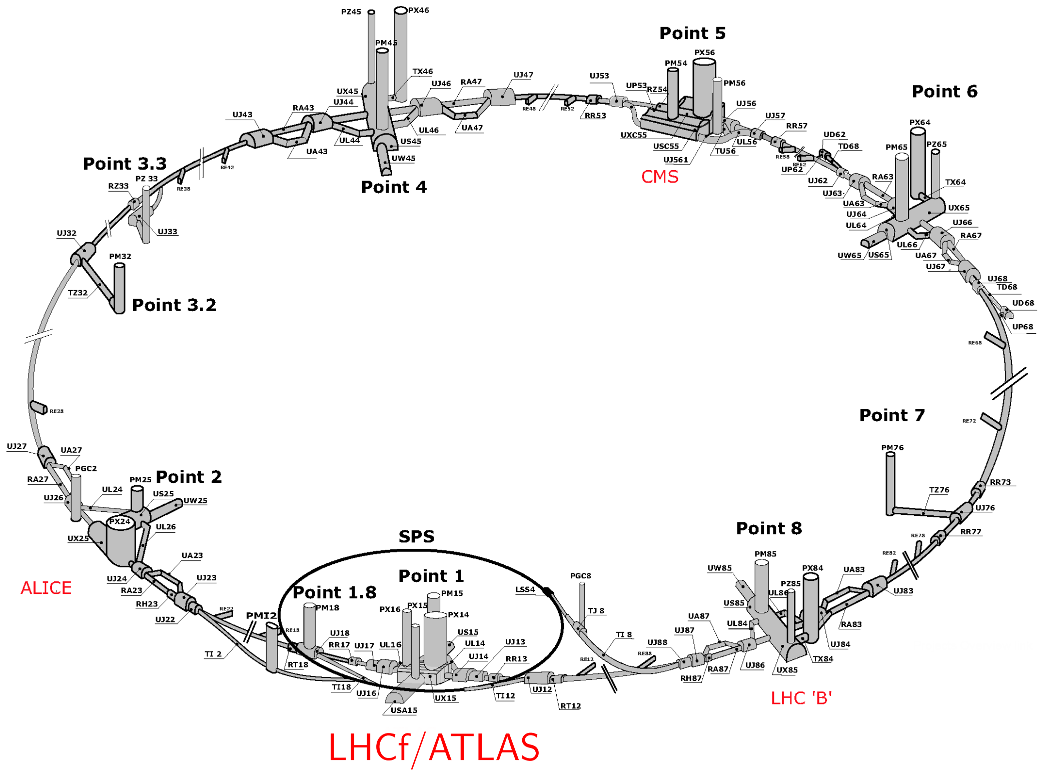

FIGURE 3.1: The LHC underground layout. The ring circumference is 26.7 km.

3.2 The LHCf detectors

3.2.1 The detectors

Figure 3.2 (a) shows the layout of the LHC tunnel around the interaction point1 (IP1). The ATLAS detector is located just around the interaction point then the beam-pipe on both side lies in the tunnel shown from left-top to right bottom of Fig. 3.2 (a). At ±140 m from the IP1, massive zero degree neutral absorbers (Target Neutral Absorber: TAN) are installed. The TAN is neutral beam absorber designed to absorb the flux of forward high energy neutral particles which are produced in IP1. Besides, the special purpose is to protect superconducting magnets from the radiation and to prevent them from quenching. The total weight of the TAN is approximately 30 Tonnes, and they are located ±140 m on each side of IPs 1 and 5. The location is just in front of the second beam separation dipole D2 and contains the Y-shaped transition from two beam tubes connecting to the LHC arc to a single common beam tube facing to the IP. Figure 3.2 (b) illustrates the schematic view of TAN. Each TAN contains a 96 mm^w× 607 mm^h× 1000 mm^l slot just behind the crotch of the Y-beam vacuum chamber. The zero degree horizontal angle just locates at the center of the slot, and the normal beam hight is 67 mm

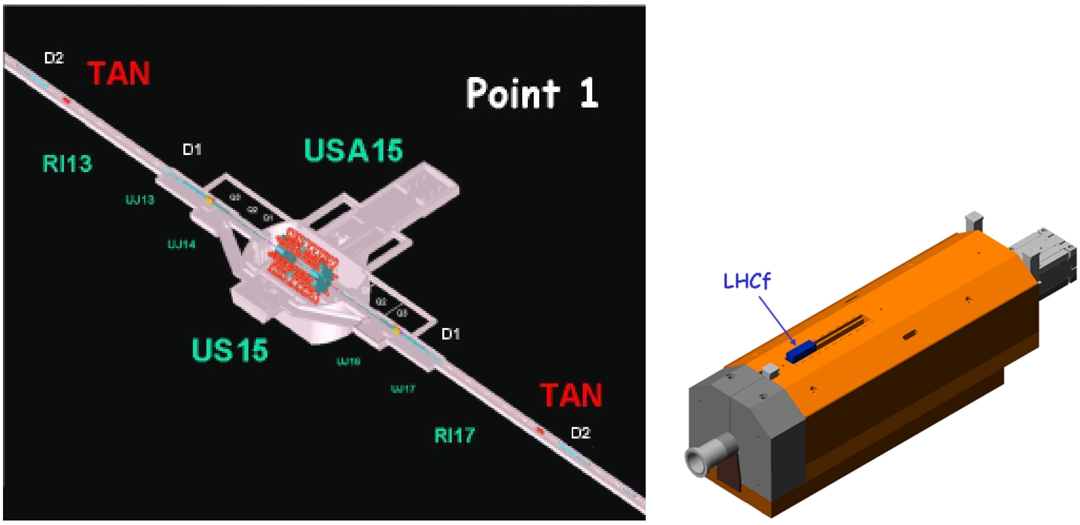

(a) Geometry of IP1 area of LHC (b) Schematic view of the TAN

FIGURE 3.2: The left figure shows the structure seen in the center represents the ATLAS detector, The LHCf detectors are installed at the places marked ”TAN” at both sides of IP1. A schematic view of the TAN is shown in right figure

from bottom of the slot. The LHCf detectors were just installed in the instrumentation slot of TANs.

LHCf has two independent detectors called Arm1 and Arm2 as shown in Fig. 3.3. Each detector consists of two sampling and imaging calorimeters (the small tower: TS and the large tower: TL) made of tungsten plates, GSO scintillators and position sensitive sensors. The detectors had been upgraded for the $\sqrt{s}$=13 TeV operation. Major differences from the previous ones are replacement of plastic scintillators with Gd_2SiO_5 (GSO) scintillators and realignment of the Arm2 calorimeter shape and the silicon sensors. These calorimeters allow to measure neutral particles (e.g. E_γ >200 GeV) emitted in the phase space of $|\eta| > 8.4$. As shown in Figs. 3.4, the structures of the calorimeters are similar, each calorimeter consists of two towers; 20 mm×20 mm, 40 mm×40 mm for Arm1 detector and 25 mm×25 mm, 32 mm×32 mm for Arm2 detector. There are 16 pieces of GSO scintillators in one tower, and each of Arm1 and Arm2 contains 32 Photo-Multiplier Tubes (PMTs) for all scintillators. Both detectors contain the position sensitive sensors, while the position sensors of two detectors are quite different. Arm1 is using 4 layers of X-Y hodoscopes made by arrays of 1 mm×1 mm GSO bars. They are installed at the depths of 6, 10, 30 and 42 X_0, where X_0 is a radiation length. In case of tungsten, it is equivalent to 3.5 mm. Multi-Anode PMTs (MAPMTs) and the Front End Circuit (FEC) for MAPMTs are used as their readout system. On the other hand, Arm2 uses silicon strip sensors installed at 6 (X-Y) and 12 (X-Y), 18 (Y), 24 (X), 32 (Y) and 40 (X) X_0. They are used to provide transverse position information of the showers. The first two layers are optimized to detect the shower maximum of gamma-ray

(a) Arm1 (b) Arm2

FIGURE 3.3: LHCf detectors Arm1 and Arm2. Calorimeter components including scintillators, tungsten plates and PMTs, position sensors and their front-end electronics are packed in a 92 mm^w× 620 mm^h× 280 mm^l aluminum box.

induced showers, and the other layers are used for hadronic showers developed deep in the calorimeters. The detectors were supported by the manipulators which can remotely move the vertical position of the detectors by ±50 mm with 100 μm accuracy. Front Counters (FC) are installed in the most forward position in the TAN slot, made by thin plastic scintillators.

The incident position provided by the position sensors is not only for obtaining the transverse momentum but also for correcting the effect of leakage from the edges of the calorimeters. Thanks to the small Moliere radius (= 0.93 cm) of tungsten comparable with the transverse calorimeter dimensions, the designed small calorimeters can contain electro-magnetic showers, but still need calibration of the shower leakage effect.

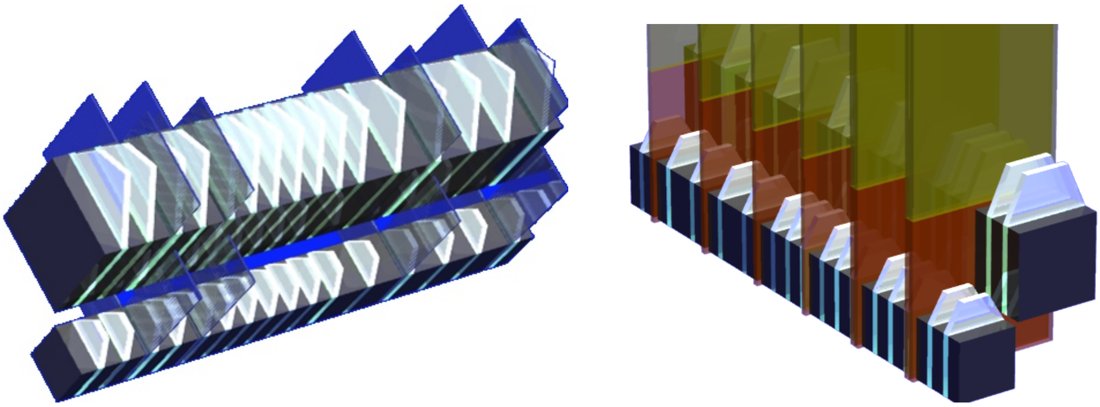

(a) Arm1 (b) Arm2

FIGURE 3.4: A schematic view of the towers of Arm1 and Arm2. They are composed of two individual tower of sampling calorimeters stacked layer by layer.

3.2.2 LHCf detector acceptance

In case of $\sqrt{s}$=13 TeV operation, because the beams collide with a 145 μrad downward crossing angle, resulting that the zero degree position at the LHCf detector moves downward by 20.46 mm. Two essential limitations let the acceptance of the LHCf detectors limited. According to [34],

- The first comes from the structure of the slot itself. It has a just 67mm free space region downward related to the beam line center in the vertical direction. The width of the slot is 96mm due to the distance between the two beam pipes near the recombination chamber.
- The second limitation comes from the beam pipe between IP1 and the TAN location. The maximum aperture for neutral particle trajectories between IP1 and the TAN are fully contained inside the vacuum pipe. The acceptance is limited by the structure of the pipe itself in the D1 dipole region located at around ±84.5 m from IP. The projection of the D1 aperture to the LHCf location at ±140 m is an ellipse with horizontal and vertical axises of 211.8 mm and of 87.7 mm, respectively. Alignment of the detector position is shown in Fig. 3.5. ”Beam center” indicated in the figures shows the extrapolated beam direction considering the 145 μrad crossing angle.

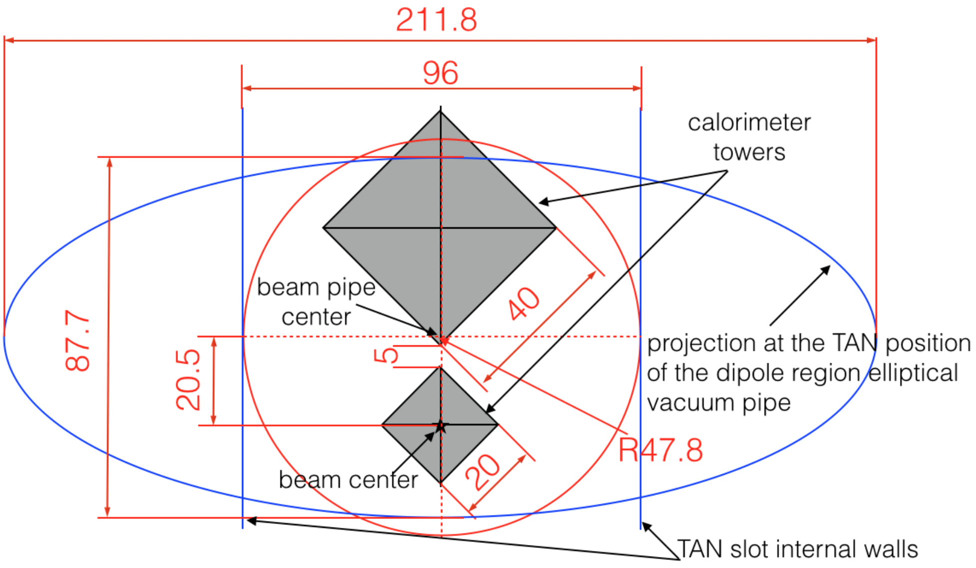

(a) Transverse projection of arm1

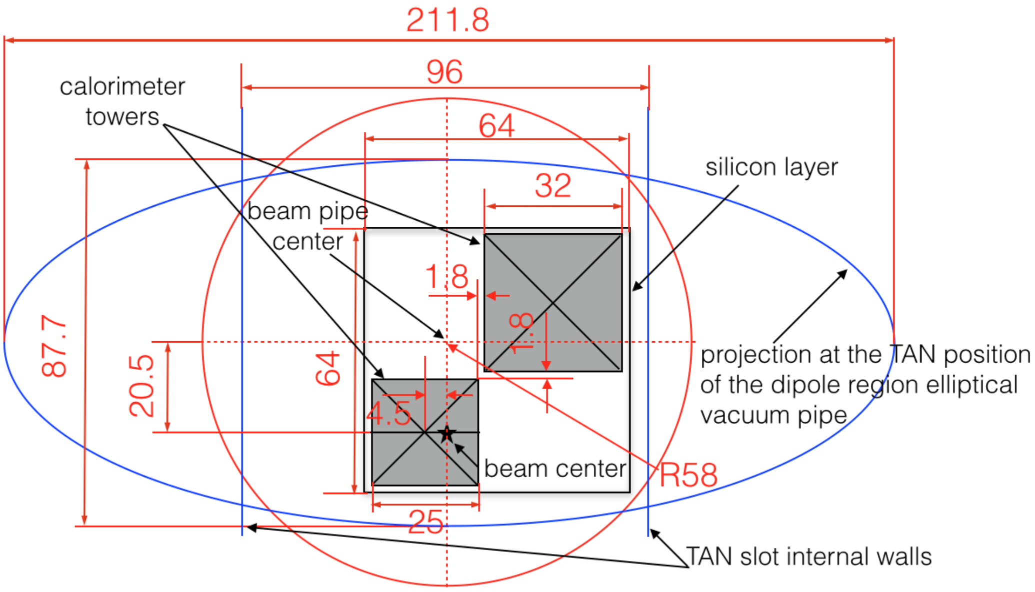

(b) Transverse projection of arm2

Figure 3.5: Acceptances of the LHCf calorimeters. In $\sqrt{s}$ =13 TeV operation, the elliptical structure of the beam pipe between IP1 and the TAN location (the main limitation to the acceptance of LHCf) and the internal walls of the TAN.

3.3 DAQ system

3.3.1 DAQ overview

The signals of PMTs were amplified then transferred from TAN to the counting room in USA15 via 200-m coaxial cables. At USA15, each signal was divided by using the FANOUT module, one divided signal entered to the discriminator and the other one for

ADC. The output signals of discriminator were fed to the FPGA module for the trigger logic. The data of each detector was separately read-out by a front-end PC through a VME-PCI bus interface (SBS; bit-3). The data acquisition software has been developed by using the MIDAS package [59]. Current data acquisition (DAQ) system of the LHCf experiment was designed for the dedicate LHCf runs, optimized only with special low luminosity ($\sim 10^{29}\mathrm{cm}^{-2}\mathrm{s}^{-1}$) run within the bunch-spacing not larger than 2μs. The limits of the DAQ rate of Arm1 and Arm2 were 0.6 kHz and 0.5 kHz, respectively. These limits come from the DAQ dead time from the FEC for Arm1 and read-out system of silicon strip sensors for Arm2. The DAQ system was housed at the space in USA15, and it could be remotely operated from the control room on the ground.

3.3.2 Trigger logic

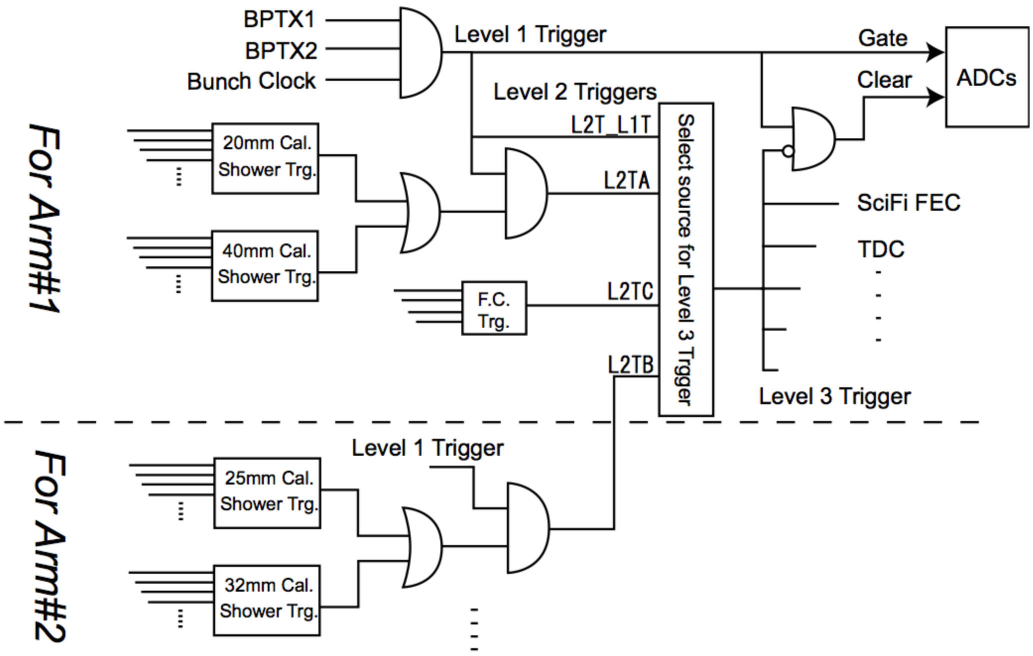

FIGURE 3.6: The schematic trigger logic diagram of the Arm1 detector.

The LHCf trigger system used the 40 MHz LHC clock as a source clock. The logic was designed by using FPGA technology, and it was load on a FPGA chip mounted on a VME board (GN0324) which was accessible through VME bus. Figure 3.6 indicates the schematic trigger logic diagram of Arm1. A Level-1 trigger is issued with two bunch crossing signals BPTX1, 2, then creates an ADC gate signal. A L2T trigger is generated by using Arm1 shower signal (L2TA), the Arm2 shower signal (L2TB), the front counters (L2TC) and the first level trigger (L2T_L1T). The shower signal is created by a coincidence of hit-signal from any adjoining 3 scintillator layers in any one of the two calorimeters. A L3T triggers are created according to the combinations of the L2T triggers, meanwhile, the generated third level trigger signal is sent to all modules. In addition, in case that the higher background noise than estimated value was observed, the coincidence of the shower trigger and the front counter belonging to the other detector can be used to reduce these background events.

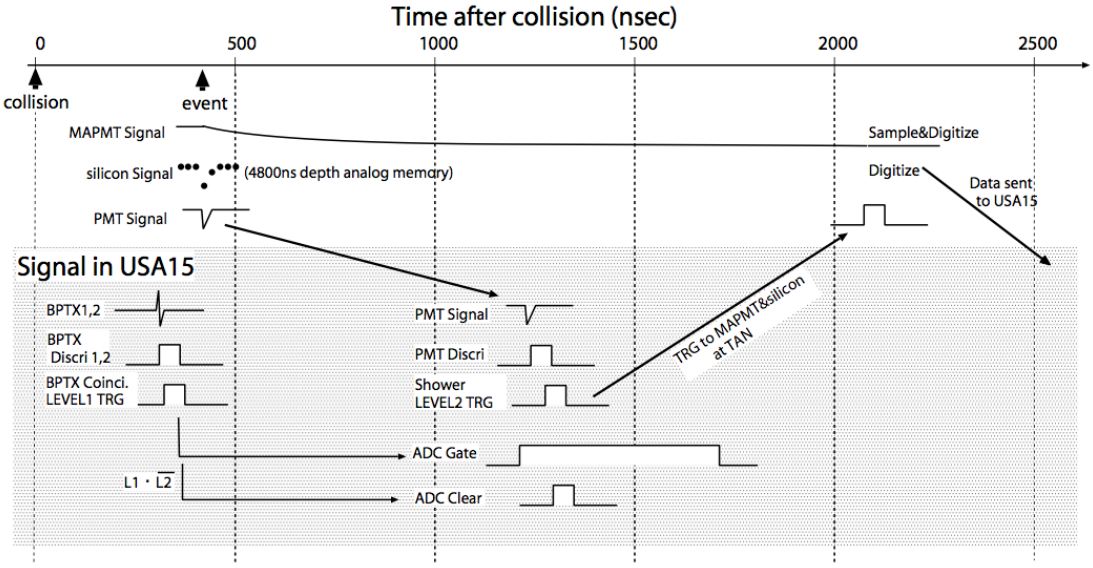

FIGURE 3.7: The time chart of the trigger and data acquisition of LHCf.

Figure 3.7 indicates the time chart of the LHCf trigger and data acquisition. Based on the timing of collision, the timing of several important stages are plotted. It takes about 0.47 μs for the secondary particles to fly from IP1 to the TAN. Then the PMT signals are transferred via cables from the LHCf detector to USA15 within 0.86 μs. From the PMT discriminator signal input to the trigger logic board, it takes approximately 300 ns to generate the LHCf final trigger signal for each module.

3.4 ATLAS-LHCf common data acquisition

3.4.1 Trigger system

In general, the common trigger system was based on the current LHCf and ATLAS trigger systems. Figure 3.8 illustrates the outline of the common trigger system. According to [31], the ATLAS trigger system is divided into three levels. The first-level trigger (Level-1) is issued with a subset of information of calorimeters and muon detectors, and the peak rate of Level-1 is 200 kHz. All of the information from the detector must be stored in pipeline memories until the Level-1 decision is available. At the Level-2 stage,

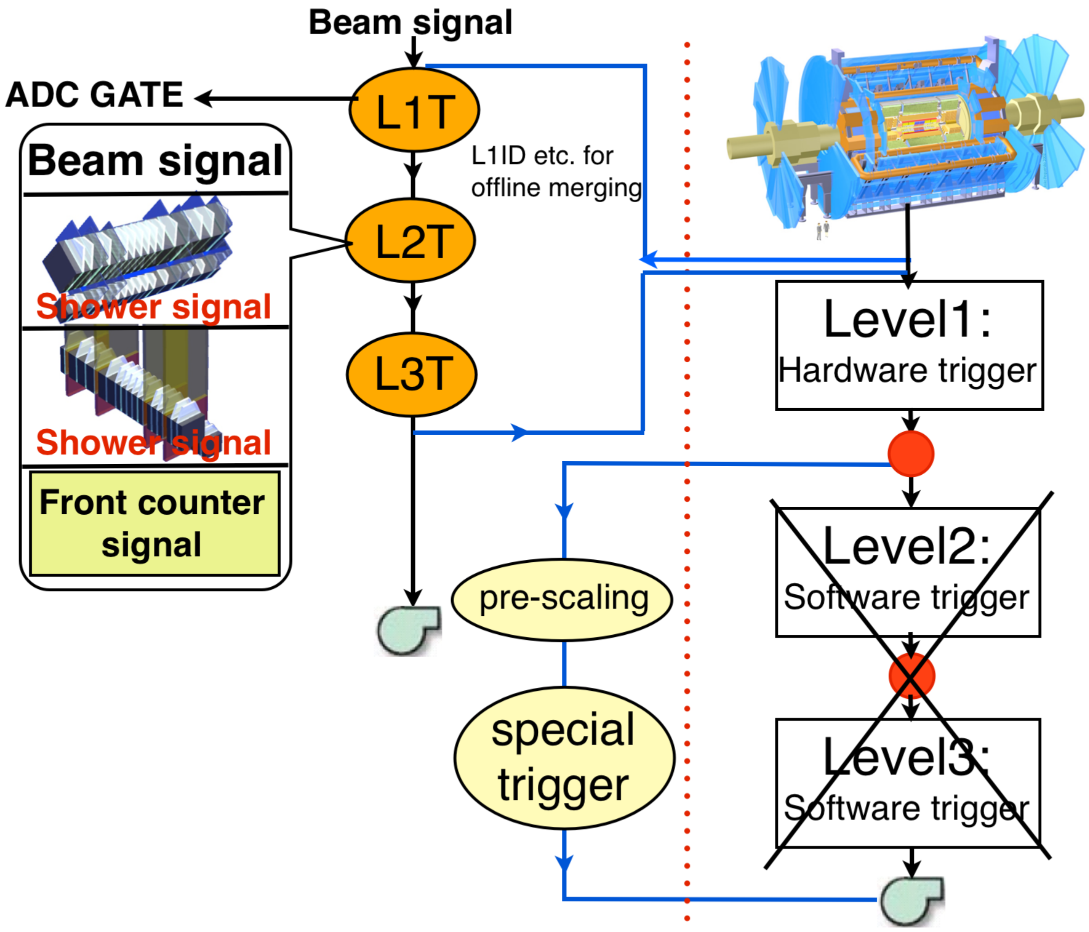

FIGURE 3.8: High-light of LHCf-ATLAS trigger system. LHCf trigger system can be one part of ATLAS trigger system, Common data acquisition will operate by pre-scaling the LHCf final trigger signals.

the data for Level-1 selected events are transferred to the readout buffers. The Level 2 trigger selectively accesses the data which is from the interest regions defined by the Level-1 trigger. At the Level-3 stage, the Event Builder assembles all event fragments from the readout buffers for events accepted by Level-2. The Level-3 output rate is kept constant at the level of 450 Hz.

Similarly, the LHCf trigger system also had three levels as explained in the last subsection. To cooperate with ATLAS,

- Firstly, LHCf has to send the final trigger signal to ATLAS before ATLAS L1A (Level-1 Acceptance: decided before 1.6μs after a collision). In principle this means that the LHCf trigger system can be a part of the ATLAS trigger system in the common trigger system.

- Secondly, once ATLAS receives the final trigger signal from LHCf, ATLAS will issue a special trigger by skipping Level-2 and Level-3, so that all the events triggered by LHCf will be directly recorded by ATLAS.

This conception allows LHCf and ATLAS to take the common events which two experiments are interested, such as diffractive events. According to this design, even no particle track is observed by the ATLAS detector as expected in the case of low mass diffractive dissociation, ATLAS can record null-track data triggered by LHCf. Finally, LHCf and ATLAS will identify the common events offline by using information like L1ID, serial number assigned to the Level-1 events.

3.4.2 Issues of the LHCf-ATLAS trigger system

For the LHCf-ATLAS trigger system, on the LHCf side, LHCf has to send the final trigger signal to ATLAS before ATLAS L1A. So the biggest issue is limited amount time for the LHCf trigger logic. The trigger logic takes about ∼200 ns in the previous version of trigger system, but to cooperate with ATLAS, it has to be reduced to ∼45 ns. As indicated in Fig. 3.9 and Table 3.1, the timing of ATLAS L1A, 1.6 μs after a collision, gives the time requirement to the LHCf trigger logic. The LHCf final trigger signal must be sent to ATLAS within 1.6 μs after the collision. However, there is an approximately 1.46 μs time latency not related to the trigger logic. Within 1.6μs, the time for particles flight to the detectors (Figure 3.9: orange bar), the scintillator signals through the amplifier and the cable latency between LHCf and ATLAS (Figure 3.9: magenta bar) and the latency of 200-m coaxial cable (Figure 3.9: yellow bar) are ∼470ns, ∼170ns and ∼820ns, respectively. Here, the latency of 200-m coaxial cable is the time of signal propagation from the LHCf detector to USA15 (the underground counting room) where the trigger system is housed. Since the 200-m coaxial cables have different lengths, the different cable length leads to the difference of transfer time ($\triangle t_1$), approximately 50 ns. Excluding the unavoidable latency mentioned above, the allowed latency ($\triangle T$) from the timing of PMT's signals arriving at USA15 to the timing of the LHCf final trigger signal output must be <140 ns. Moreover, remaining 140ns can be divided into three parts. The first two parts are the latency of signal through FANOUT, discriminator and input/output of the trigger module ($\triangle t_2$ ∼35 ns as shown in Fig. 3.9 with a green bar) and time-walk[1] ($\triangle t_3$ ∼60 ns as shown in Fig. 3.9 with a white bar). Finally, the time latency allowed for the trigger logic is extremely short, approximately ∼45ns ($\triangle t_4$, $\triangle T = \triangle t_2 + 2\times \triangle t_3 + \triangle t_4 = \sim 140$ ns).

---

[1] The scintillator pulses have identical rise times that are much longer than the desired temporal resolution. This will influence the threshold trigger timing, and the trigger timing will depend on the signal's peck height. this effect called time walk.

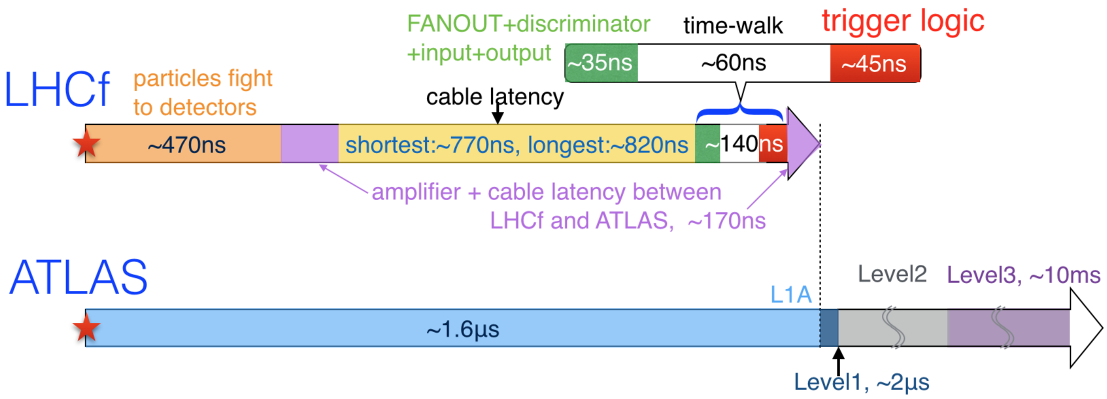

FIGURE 3.9: Trigger timing of LHCf and ATLAS relate to the collision timing.

TABLE 3.1: The timing correspondence table between LHCf and ATLAS

LHCf		ATLAS	
Collision	0 ns	Collision	0 ns
Particles fly to detectors	∼470ns	L1A: 1.6μs	
Amplifier + cable latency between LHCf and ATLAS	∼170ns		
200-m coaxial cable latency	shortest: ∼770ns		
	longest: ∼820ns		
FANOUT + discriminator input + output	∼35ns		
Time-walk	∼60ns		
Trigger logic	∼45ns		
		Level-1	2μs
		Level-1 + Level 2 + Level 3	10ms

The latency of time-walk which is ∼60ns estimated by a following measurement. The test result of time-walk of the signal from a LHCf GSO scintillator is illustrated in Figure 3.10. The three signals shown in the figure are the outputs from the oscilloscope, which were measured in the SPS beam test. The experiment was done under the same situation of 13 TeV operation. Firstly, to develop a electromagnetic cascade inside the calorimeters by incident the electron beams, then the signals went through the electronics and 200-m cable, corresponding to the timing of signals input to the discriminator, the wave form of the three signals are recorded as shown in Figure 3.10. Depending on the peck height, the time-walk can reach ∼30ns. Finally, considering the latency of time-walk, the estimated margin for it in this design have to be ∼60ns ($2\times \triangle t_3 = \sim 60$ ns).

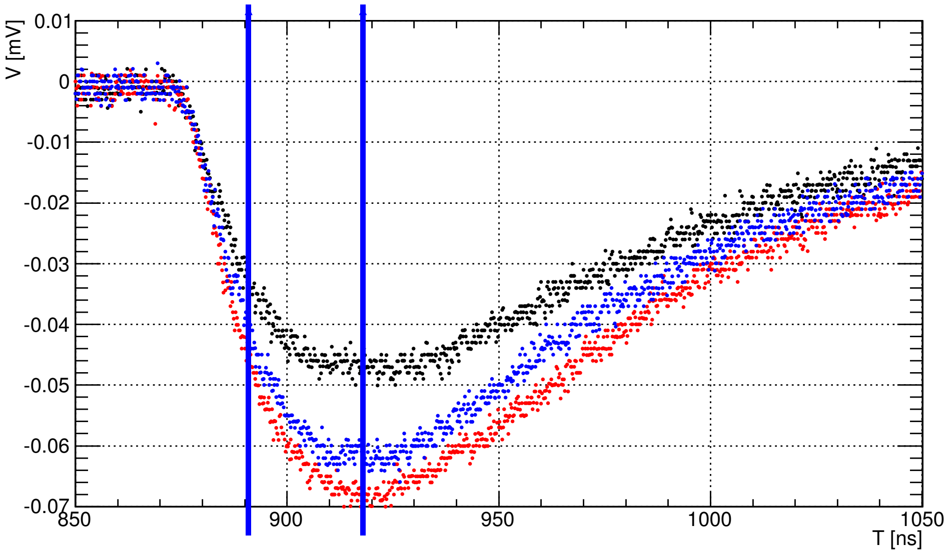

FIGURE 3.10: The output signals from oscilloscope, these 3 signals indicate the time walk of signals from scintillators.

3.4.3 Strategies to solve the timing issue

To solve the very tight timing constraints for the trigger logic, following strategies was applied;

- Use a single logic board with enough I/O pins to replace the previous two logic boards,
- Use doubled frequency clock (40 MHz → 80 MHz) inside the new main logic board,
- Tune the trigger logic with narrow width window and reduce a number of clock synchronized module used inside the logic.

In the design of the LHCf trigger system, numbers of input channels for the scintillator signals and FC signals of both arms require 64 and 16, respectively, excluding the communicating signals. Including other signal channels, such as beam signals, data transfer signals and so on, it needs approximately 120 I/O (90 inputs/ 30 outputs) pins to satisfy the requirement of logic. Figure 3.11 (a) shows the logic located inside the GPIO boards (GN0324) used in the the previous LHCf trigger logic. Due to the limited I/O (input/output) pins, the previous version of LHCf trigger logic had been divided into two parts, the LHCF LOGIC and LHCF L1T LOGIC. The LHCF LOGIC was mainly in charge of the decision of the showers inside the calorimeters. In contrast, the coincident events of Arm1 and Arm2 were decided by LHCF L1T LOGIC. Each part of the logic was loaded onto one different GPIO board. Therefore, the data transfer between two

GPIO boards lost ∼5 ns per signal I/O. As marked by red circles in Fig. 3.11 (a), it lost 20 ns in total. On the other hand, Figure 3.11 (b) indicates the image on the new FPGA board (CAEN V1495) used in the new LHCf trigger logic. Basically, the new logic board is chosen by considering that it has to satisfy the requirements of the numbers of I/O pin and gate. General functions as the previous ones, such as remote control via VME access, are also required. The LHCF LOGIC of Arm1 and Arm2 together with LHCF L1T LOGIC can be loaded onto the new single FPGA board, until generating the LHCf final trigger signal to ATLAS. Thus, using the new FPGA board save signal transfer time between two previous GPIO boards and the time for synchronization of transferred signals. In the new design, the final trigger signals for the modules belonging to each detector are individually generated inside the GN0324 board as shown in Figure 3.11 (b). Also, the COUNTER data of Arm1 and Arm2 inside the CAEN V1495 has to be transferred to GN0324 boards belonging to Arm1 and Arm2, respectively. The data transfer between CAEN V1495 and GN0324 is the new issue to solve together with replacing the previous boards by CAEN V1495.

In principle, the logic inside the FPGA chip runs synchronously with the global clock. So the usage of the doubled frequency clock (40 MHz→ 80 MHz) in the new trigger logic is able to reduce the operation time for each clock synchronized module from 25 ns to 12.5 ns. Additionally, it will also improve the trigger logic time tuning resolution by using the doubled frequency clock with 12.5 ns accuracy. Moreover, we must reduce the number of the clock synchronized module inside the logic.

3.4.4 Time chart of the new trigger logic

Finally, using the generated signals described in the previous section, the new logic is tuned and tested precisely. The time of the signals running through the discriminator and the cable between a discriminator and the FPGA board is also considered in this test. The Figure 3.12 illustrates the time chart of the new trigger logic. The several listed signals are generated at important stages which indicate the timing process in the trigger logic. Starting from the timing of $A1\_DSC_{Discriminator\_out}$, the latency of the LHCf final trigger signal for ATLAS (A1_ATLAS) is 139 ns, satisfying the time limit requirement (140 ns: $\triangle t_2 + 2 \times \triangle t_3 + \triangle t_4$) of the new logic mentioned in section 4.2. The latency of time-walk estimated to be $2\times \triangle t_2$: 60 ns was set to be 75 ns in this test design taking enough margin in the extreme case. Corresponding to the time limit requirement of the trigger logic (45 ns), it takes extremely short 26 ns (A1_ATLAS: 101 ns - A1_DL1T: 75 ns) to run the new trigger logic in this test. Additionally, a snapshot of the oscilloscope screen showing the signals A1_DSC2(7), A1_L3T2, A1_L3T and A1_ATLAS in the test is shown in Figure 3.13. From A1_DSC(7)$_{GPIO\_out}$ to A1_ATLAS, the latency is 101 ns which includes the latency of time-walk and trigger logic.

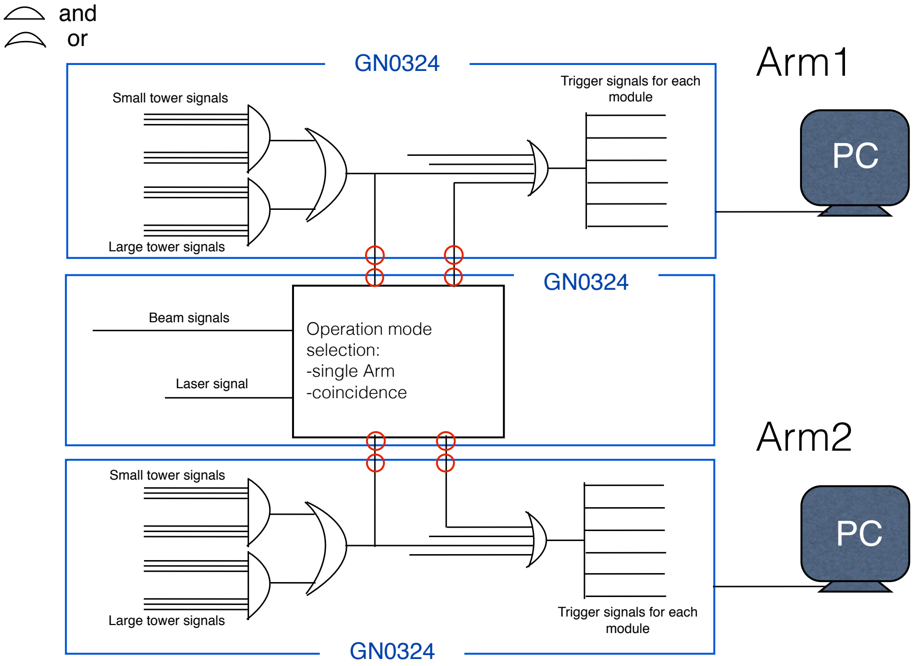

(a) The location image of previous LHCf trigger logic

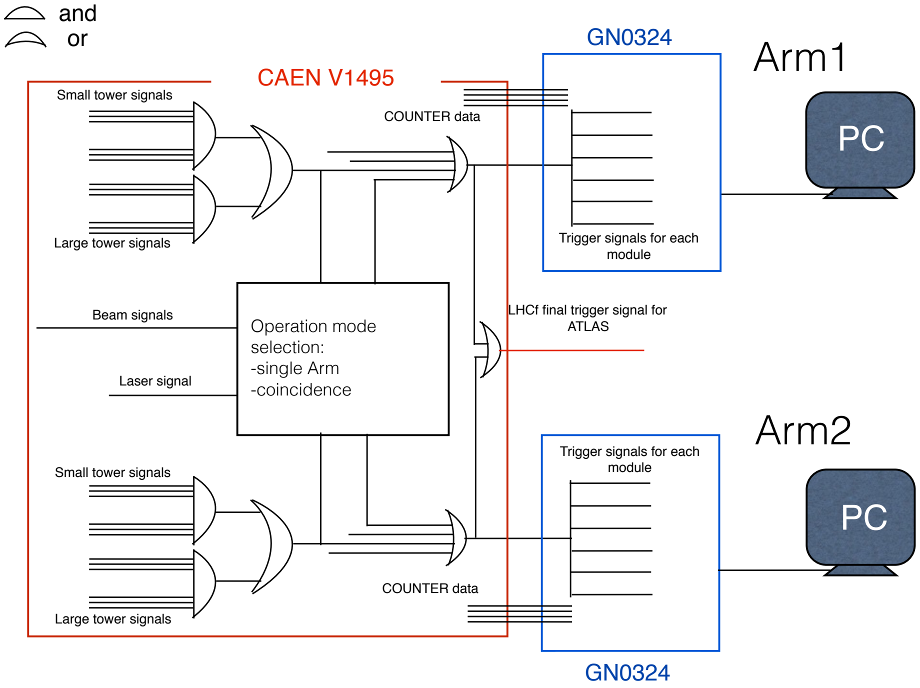

(b) The location image of new LHCf trigger logic

FIGURE 3.11: The modification of location image between previous and new LHCf trigger logic.

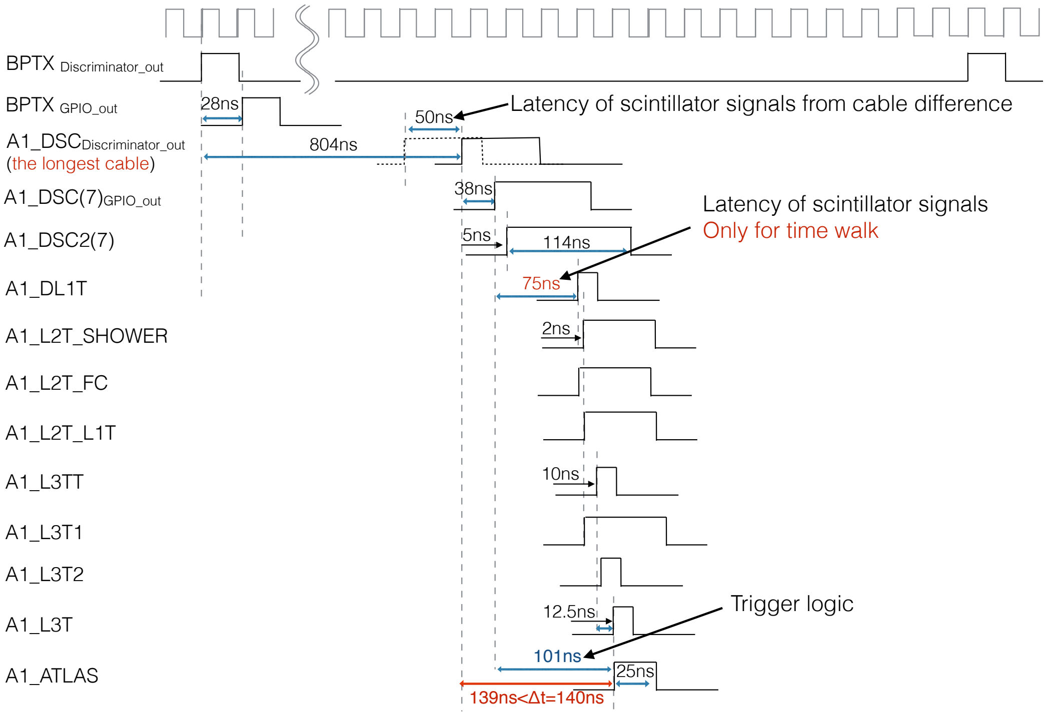

Figure 3.12: Measured time chart of the new trigger logic in the test.

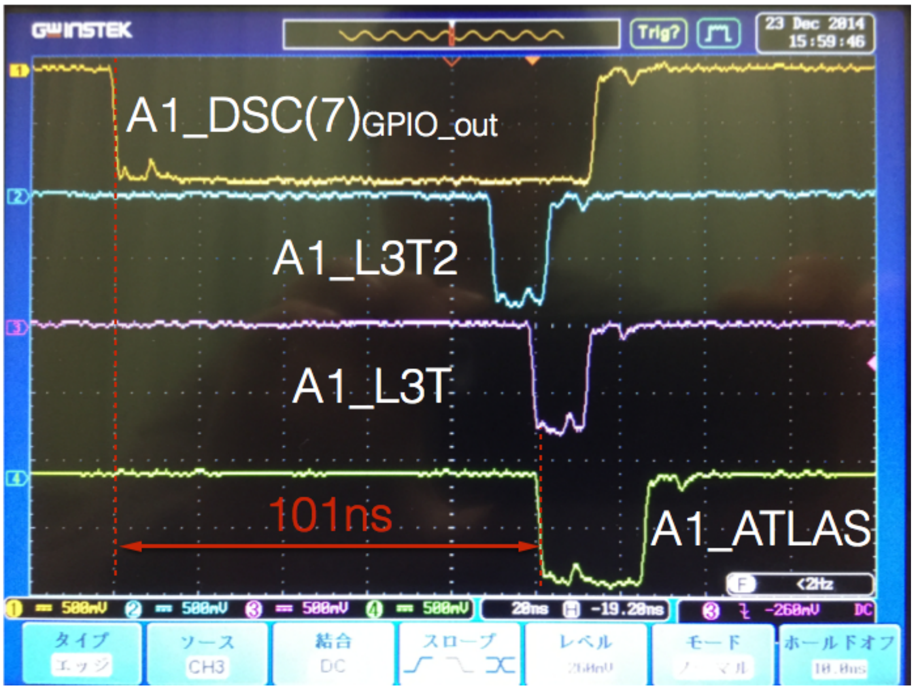

Figure 3.13: Oscilloscope output result of trigger logic timing test

Chapter 4

Monte Carlo study of particle production in diffractive p-p collisions at $\sqrt{s} = 13$ TeV with the ATLAS-LHCf detector

4.1 Setup for the Monte Carlo study

In this Chapter, parts of the ATLAS detector [31] and the LHCf detectors [34] located at interaction point 1 (IP1) of the LHC are considered to be representatives of the central detectors and Very Forward (VF) detectors, respectively. The ATLAS inner detector (ID) measures particle momentum and vertex information with full azimuthal (ϕ) and $|\eta| < 2.5$ pseudorapidity coverage. For studies of minimum-bias measurements, this detector can provide information on charged tracks with a p_T threshold as low as 100 MeV. The LHCf detectors were installed in the target neutral absorber (TAN) located ±140 m from IP1. The detectors were designed to measuring forward neutral particles (e.g., neutrons, photons, and π^0s) over a pseudorapidity range $|\eta| > 8.4$. The photon and hadron energy thresholds are 200 and 500 GeV, respectively.

4.2 Monte Carlo simulation

In this analysis, MC simulation samples were produced using four interaction models for comparison. p–p collision events at $\sqrt{s} = 13$ TeV were simulated by each model, and trigger conditions of a VF-detector were applied based on the energy, particle type, and

η according to the LHCf case. Four MC generators are extensively used in cosmic-ray observations and high-energy experiments: EPOS-LHC [21], QGSJET-II-04 [22], SIBYLL 2.3 [23, 24], and PYTHIA 8212 [25, 26]. All these models are post-LHC generators tuned by using the LHC Run1 data. The first three simulation samples were generated by using the integrated interface tool CRMC v1.6.0 [60], whereas for PHYHIA, its own front-end was used.

For the PYTHIA8 generator, Monash event tuning [61] was employed in this analysis. Minimum-bias data and underlying event data from the LHC were used for constraining the parameters. The new NNPDF2.3 LO PDF set was adopted in the event tuning. By default, PYTHIA8 uses the Schuler and Sjöstrand (SS) parameterization [62] of the pomeron flux. In addition, an alternative pomeron flux model, the Donnachie and Landshoff (DL) [63] model, with a linear pomeron trajectory $\alpha_P(t) = 1 + \Delta + \alpha' t$ is also implemented. The default value of variable parameters Δ and α' are 0.085 and 0.25 GeV^{-2} [46], respectively. According to the ATLAS minimum-bias measurement in p–p collisions at $\sqrt{s} = 13$ TeV, the PYTHIA8212DL model gives the best description of the number of hits detected by the minimum-bias trigger scintillators [64]. Therefore, the PYTHIA8212DL model was employed in this analysis. The total inelastic cross sections in p–p collisions at $\sqrt{s} = 13$ TeV implemented in each model were 78.984, 80.167, 78.420, and 79.865 mb, corresponding to EPOS-LHC, QGSJET-II-04, PYTHIA8212DL, and SIBYLL2.3, respectively.

Given the model differences in the treatments of diffractive components, not only the predicted diffraction cross sections but also the diffractive mass distributions are important. Figure 4.1 shows the SD ($pp \to pX$) cross sections in each ξ_X interval predicted by several models. The different spectral shapes come from the different approaches to the diffraction treatment implemented in the models. There are large differences among models in both the high and low diffractive mass regions. The flat distribution of SD cross section of the SIBYLL2.3 model, which corresponds to a diffractive mass distribution described as dM_X^2/M_X^2 [65]. The PYTHIA8212 model (SS pomeron flux) uses a treatment similar to that of SIBYLL2.3 for the diffractive mass distribution [62]. In the high diffractive mass regions, EPOS-LHC tuned $d\sigma^{SD}/d\Delta\eta$ [21] by comparing with the data of the ATLAS rapidity gap distribution shown in [50]. The inset of Fig. 4.1 shows the low-mass SD cross sections of each model in the ξ_X interval $-8.5 < \log_{10}(\xi_x) < -5.5$. The QGSJET-II-04 model uses different transverse profiles for pomeron emission vertices by different elastic scattering eigenstates [22, 66]. This leads to the larger cross sections in the low-mass regions at very high energies.

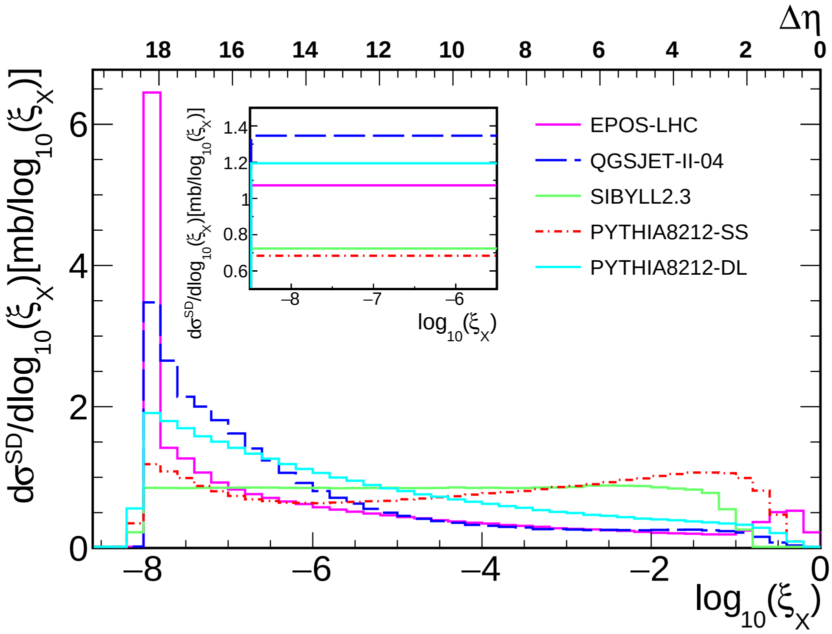

FIGURE 4.1: SD ($pp \to pX$; blue) cross section shown as a function of $\log_{10} \xi_X$. MC predictions with EPOS-LHC (magenta), QGSJET-II-04 (blue dashed), SIBYLL2.3 (green), PYTHIA8212-SS (red dotted-dashed), and PYTHIA8212-DL (cyan) compared with each other. The comparison of low-M_X SD cross section predicted by models is shown in the inset.

4.3 Diffractive and non-diffractive contributions to the LHCf particle production

The LHCf collaboration has published several forward neutral particle spectra at different collision energies, but no hadronic interaction model can describe the LHCf results perfectly [36–38, 40, 42]. To address the origin of the differences between the experimental data and the model predictions, separating the VF-triggered events to diffractive and non-diffractive contributions is important. In this analysis, all the events from each simulation are classified into non-diffractive and diffractive collisions by using MC flags, where the SD, DD, and CD events are together treated as diffraction. It is noted that the SIBYLL2.3 model does not implement CD processes. The simulated VF-photon and neutron spectra are shown in the top four panels of each side of Figs. 4.2 and 4.3 for two fiducial areas, $|\eta| > 10.94$ (left) and $8.81 < \eta < 8.99$ (right), respectively. Meanwhile, Fig. 4.4 shows the π^0 p_z spectra at the fiducial p_T phase spaces of $0 < p_T < 0.2$ GeV (left) and $1.2 < p_T < 1.4$ GeV (right), respectively. The spectra of total, non-diffractive, and diffractive components of four MC samples are compared with each other. In the bottom three panels of Figs. 4.2, 4.3, and 4.4, the ratios of the spectra divided by the EPOS-LHC results are plotted separately for total, non-diffractive, and diffractive components. Clearly, the non-diffraction and diffraction implemented in each model are very different. Especially, PYTHIA8212DL predicts the largest diffractive contribution at high photon

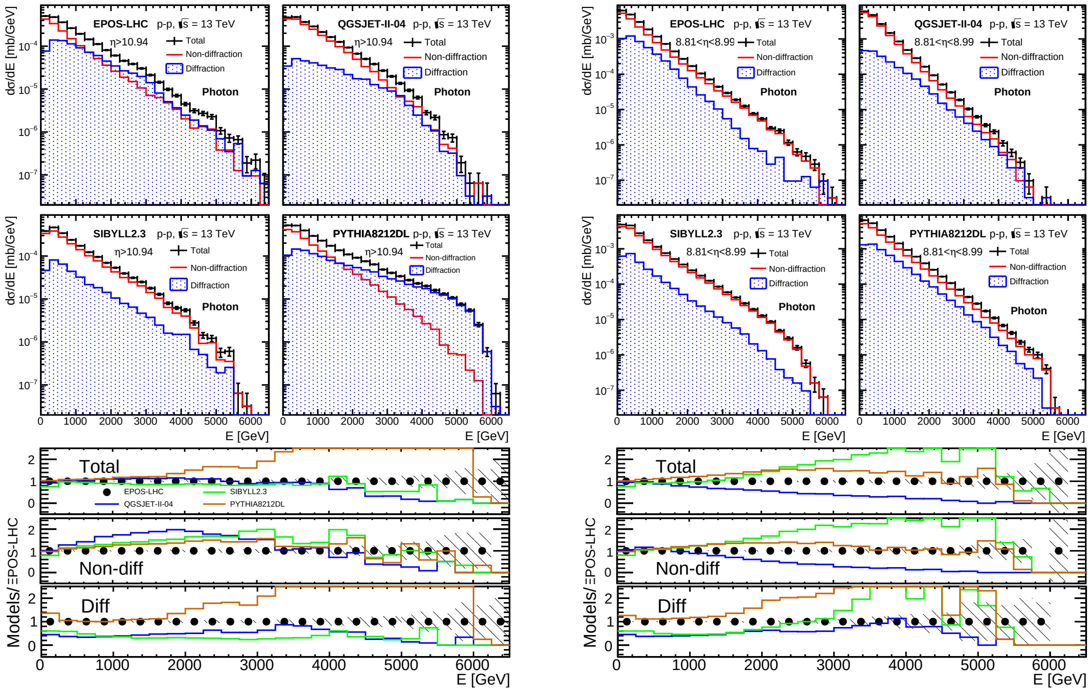

Figure 4.2: Photon spectra at $\eta > 10.94$ (left) and $8.81 < \eta < 8.99$ (right) (top four panels in each set). These are generated by EPOS-LHC, QGSJET-II-04, SIBYLL 2.3, and PYTHIA 8212DL, respectively. The total photon spectra (black) were classified by non-diffraction (red) and diffraction (blue) according to MC true flags. The bottom three plots show the ratios of the spectra of EPOS-LHC (black markers), QGSJET-II-04 (blue lines), SIBYLL 2.3 (green lines), and PYTHIA8212DL (orange lines) to the spectrum of EPOS-LHC. The top, middle, and bottom plots correspond to total, non-diffraction, and diffraction, respectively.

energies at $|\eta| > 10.94$ and in the π^0 p_z spectrum at $0 < p_T < 0.2$ GeV. There is no large difference among models of the neutron total spectra at $|\eta| > 10.94$. In contrast, comparing the individual contribution of non-diffractive and diffractive components, one sees that the neutron spectra of EPOS-LHC and PYTHIA8212DL are dominated by diffraction, but those of QGSJET-II-04 and SIBYLL2.3 are dominated by non-diffraction at high energies. As shown in Fig. 4.4, SIBYLL2.3 predicts a larger contribution for all components at $1.2 < p_T < 1.4$ GeV. It is also found that the larger the value of p_T is, the larger is the contribution from all components predicted by SIBYLL2.3. Additionally, in Figs. 4.3 and 4.4, neutron and π^0 spectra of EPOS-LHC and QGSJET-II-04 exhibit a bump or kink structure at ∼3 TeV. In the EPOS-LHC model, this structure is due to the simple approach used for the pion-exchange process, whereas in QGSJET-II-04 it is due to the selected kinematics, which is $\eta > 10.94$ or $p_T > 0.2$ GeV. Low-mass diffraction mainly contribute to these selected kinematics regions.

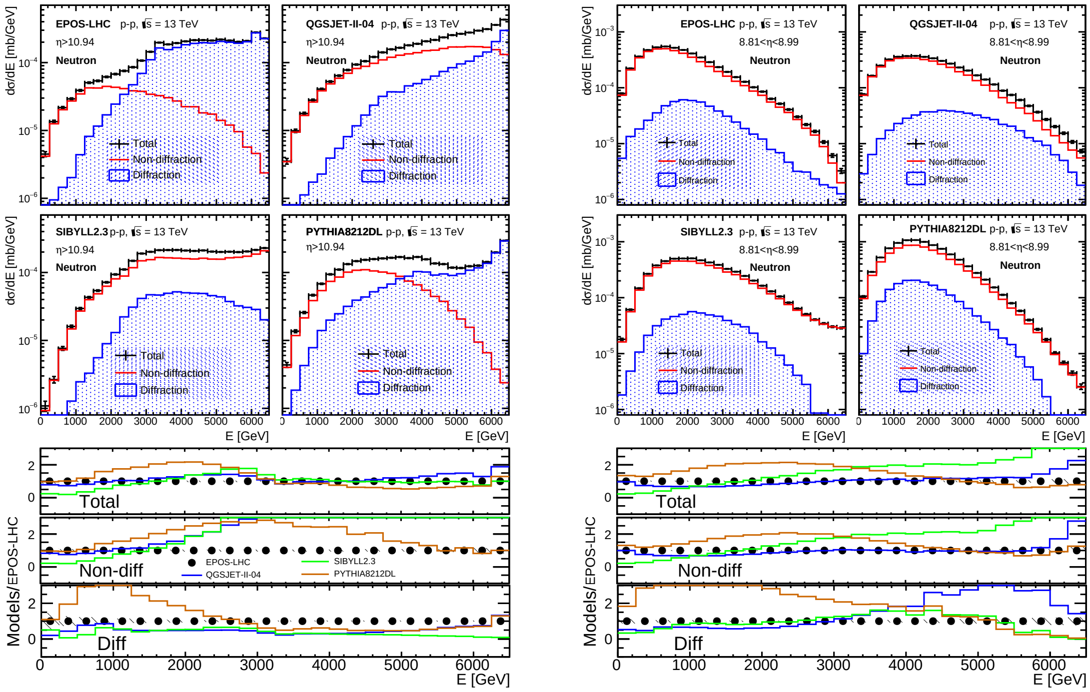

FIGURE 4.3: Neutron spectra at $\eta > 10.94$ (left) and $8.81 < \eta < 8.99$ (right) (top four panels in each set). These are generated by EPOS-LHC, QGSJET-II-04, SIBYLL 2.3, and PYTHIA 8212DL, respectively. The total neutron spectra (black) were classified by non-diffraction (red) and diffraction (blue) according to MC true flags. The bottom three plots show the ratios of the spectrum of EPOS-LHC (black markers), QGSJET-II-04 (blue lines), SIBYLL 2.3 (green lines), and PYTHIA8212DL (orange lines) to the spectrum of EPOS-LHC. The top, middle, and bottom plots correspond to total, non-diffraction, and diffraction, respectively.

4.4 Identification of diffraction with the ATLAS track information

Because of the large differences found among different hadronic interaction models, it is important to classify the observed VF-spectra into non-diffraction or diffraction by using central measurement data. Although, in principle, diffractive collisions can be identified by measuring the rapidity gap of the final state, it is experimentally difficult to measure rapidity gaps precisely because of the limited pseudorapidity coverage and energy threshold of the detectors. However, improved experimental techniques have helped in reaching lower p_T thresholds and larger rapidity ranges. The results from measurements of rapidity gaps over limited pseudorapidity ranges have been reported by ATLAS [50], CMS [53], and ALICE [54] Collaborations. Similarly, such rapidity gap techniques can be adopted for diffractive event identification.

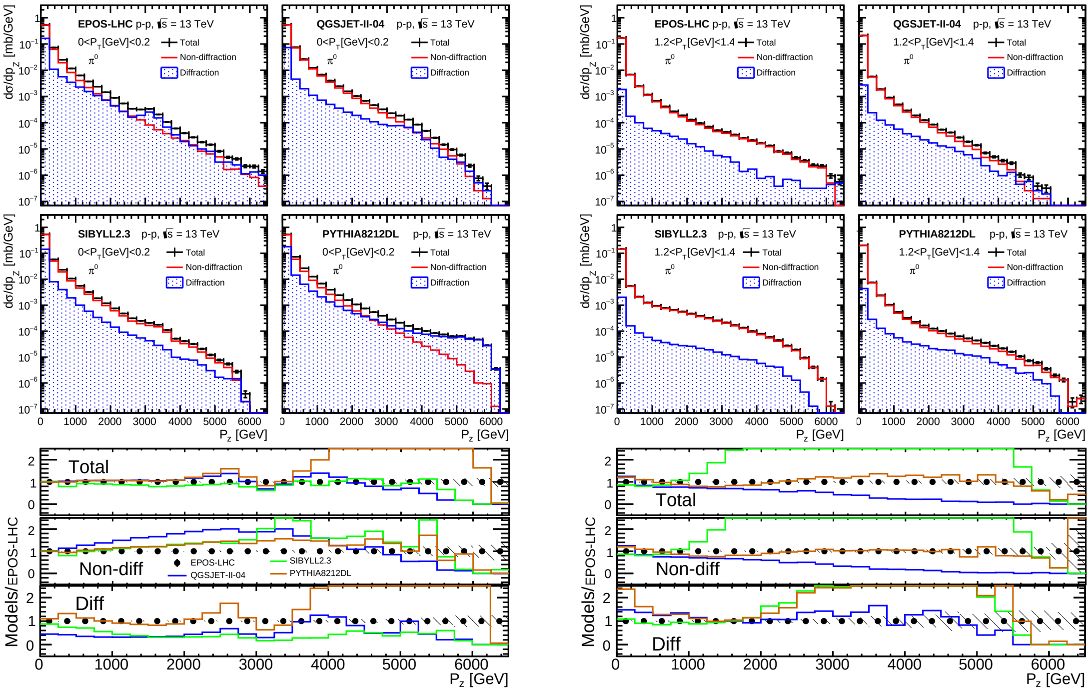

FIGURE 4.4: π^0 spectra shown with $0 < P_T < 0.2$ GeV (left) and $1.2 < P_T < 1.4$ GeV (right) for comparison. In each P_T phase region, the top four panels show π^0 spectra generated by EPOS-LHC, QGSJET-II-04, SIBYLL 2.3, and PYTHIA 8212DL, respectively. The total π^0 spectra (black) were classified by non-diffraction (red) and diffraction (blue) according to MC true flags. The bottom three plots show the ratios of the spectrum of EPOS-LHC (black markers), QGSJET-II-04 (blue lines), SIBYLL 2.3 (green lines), and PYTHIA8212DL (orange lines) to the spectrum of EPOS-LHC. The top, middle, and bottom plots correspond to total, non-diffraction, and diffraction, respectively.

TABLE 4.1: Efficiency and purity of central-veto selection with different track conditions.

Parameter	$N_{track} = 0$	$N_{track} \leq 1$	$N_{track} \leq 2$	$N_{track} \leq 5$
Efficiency (ϵ)	0.493	0.556	0.619	0.691
Purity (p)	0.995	0.991	0.982	0.950

4.4.1 Diffraction selection criteria

The identification of the type of diffraction requires detection of a large rapidity gap because small rapidity gaps may be produced by fluctuations in non-diffractive particle production [67]. Consequently, a small number of particles is expected in the central detector, for instance, the ATLAS detector. If an event has a small number of tracks, N_{track}, it is more likely to be a diffractive event. This is the basic idea in this analysis used to identify diffractive events. In other words, having a small number of charged tracks in the central region is used to *veto* non-diffractive events. It is assumed that the central

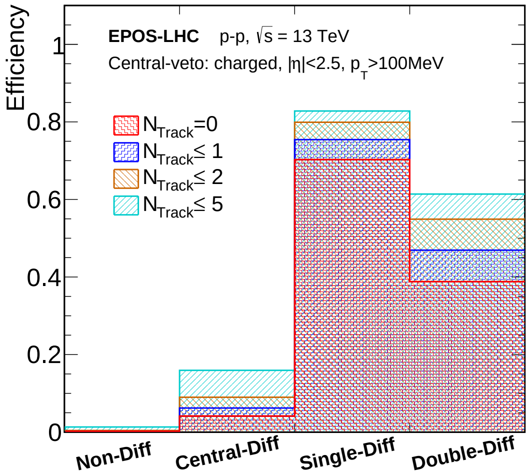

FIGURE 4.5: Diffraction selection efficiency with different central-veto selection conditions: $N_{track} = 0$ (red), $N_{track} \leq 1$ (blue), $N_{track} \leq 2$ (brown), and $N_{track} \leq 5$ (cyan) charged particles at $|\eta| < 2.5$ with $p_T > 100$ MeV.

detector can count N_{track} with $p_T > 100$ MeV at $|\eta| < 2.5$. The performance of central-veto event selection was studied for different criteria of N_{track}, $N_{track} = 0$, $N_{track} \leq 1$, $N_{track} \leq 2$, and $N_{track} \leq 5$ in [68]. If the event survives central-veto selection, it is classified as a diffractive-like event; otherwise, it is classified as a non-diffractive-like event. According to MC true flags, events can be classified as non-diffraction (ND), CD, SD, and DD. By applying central-veto selection to each event, the selection efficiency (ϵ) and purity (κ) of diffractive event selection are defined as

$$\epsilon = \frac{(N_{CD} + N_{SD} + N_{DD})_{central\ veto}}{N_{CD} + N_{SD} + N_{DD}}, \tag{4.1}$$

$$\kappa = \frac{(N_{CD} + N_{SD} + N_{DD})_{central\ veto}}{(N_{ND} + N_{CD} + N_{SD} + N_{DD})_{central\ veto}}, \tag{4.2}$$

where N_{ND}, N_{CD}, M_{SD}, and N_{DD} indicate the number of events triggered by a VF detector in each event category. The suffix *central veto* signifies number of events after applying central-veto event selection.

Figure 4.5 shows a comparison of the central-veto selection efficiency with the four criteria, which are calculated by using the EPOS-LHC simulation samples. It is clear that the efficiency rises as the N_{track} threshold increases. SD selection efficiency, for instance, increases from about 70% to 80% as $N_{track} = 0$ changes to $N_{track} \leq 5$. The efficiency and purity of the central-veto selection for the four criteria are summarized in Table 4.1. High selection purity (99.5%) is achieved when the criterion is $N_{track} = 0$ while it decreases only by 5% when $N_{track} \leq 5$ is applied. To aid our discussion using a simple analysis, we adopt the following criterion for the central veto (diffraction selection): *There are no charged particles ($N_{track} = 0$) in the kinematic range $|\eta| < 2.5$ and $p_T > 100$ MeV.*

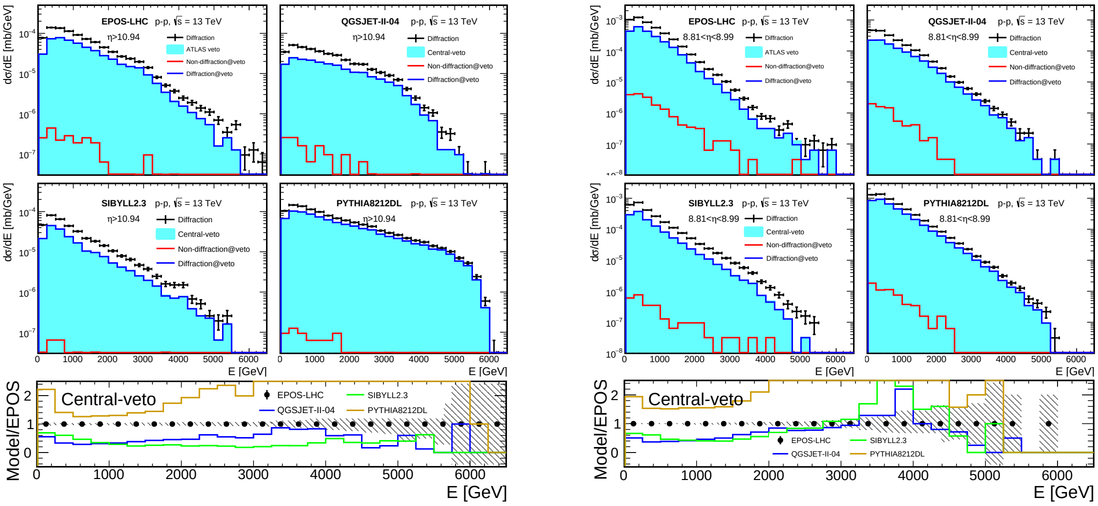

(a) $\eta > 10.94$

(b) $8.81 < \eta < 8.99$

Figure 4.6: Photon spectra at (a) $\eta > 10.94$ and (b) $8.81 < \eta < 8.99$ generated by EPOS-LHC, QGSJET-II-04, SIBYLL 2.3, and PYTHIA 8212DL. The top four panels show the spectra of true diffraction (black lines) and diffractive-like events corresponding to central-veto selection (filled gray areas), which are defined as events without any $P_T > 100$ MeV charged particles at $|\eta| < 2.5$; in addition, the central-veto events were classified by non-diffraction (red) and diffraction (blue) again according to MC true information. The bottom plot shows the ratios of the central-veto spectrum of each model to the central-veto spectrum of EPOS-LHC.

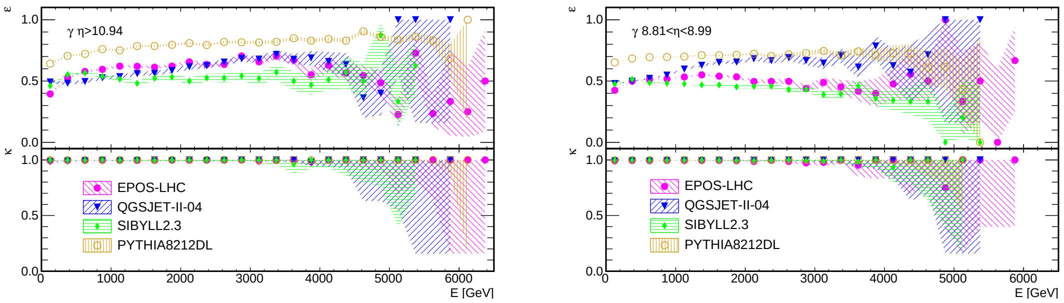

(a) $\eta > 10.94$

(b) $8.81 < \eta < 8.99$

Figure 4.7: Efficiency (top) and purity (bottom) of diffraction selection for the VF ((a) $\eta > 10.94$ and (b) $8.81 < \eta < 8.99$) photon spectra obtained by using the central-veto technique.

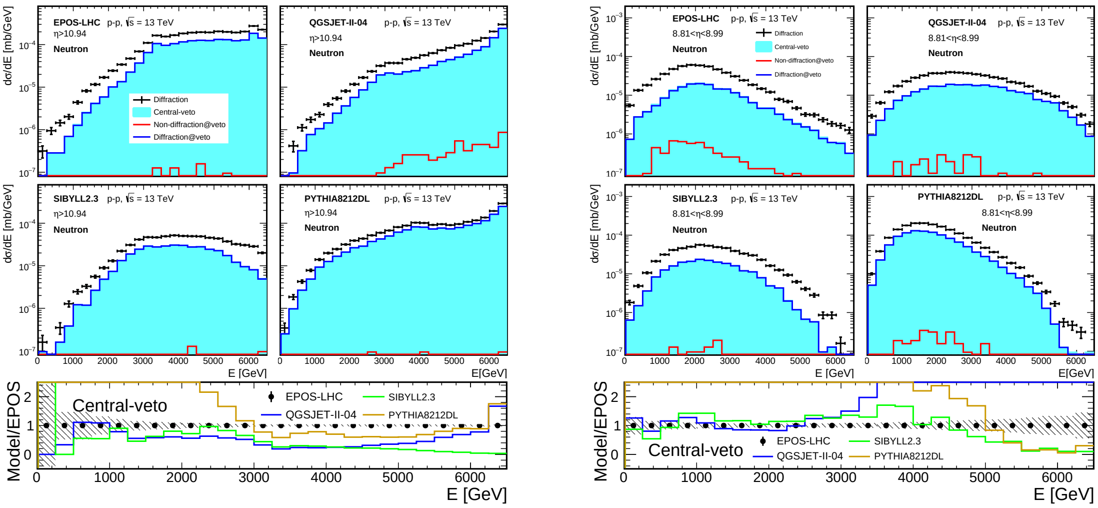

(a) $\eta > 10.94$

(b) $8.81 < \eta < 8.99$

FIGURE 4.8: Neutron spectra at (a) $\eta > 10.94$ and (b) $8.81 < \eta < 8.99$ generated by EPOS-LHC, QGSJET-II-04, SIBYLL 2.3, and PYTHIA 8212DL. The top four panels show the spectra of true diffraction (black lines) and diffractive-like events corresponding to central-veto selection (filled gray areas), which are defined as events without any $P_T > 100$ MeV charged particles at $|\eta| < 2.5$; in addition, the central-veto events were classified by non-diffraction (red) and diffraction (blue) again according to MC true information. The bottom plot shows the ratios of the central-veto spectrum of each model to the central-veto spectrum of EPOS-LHC.

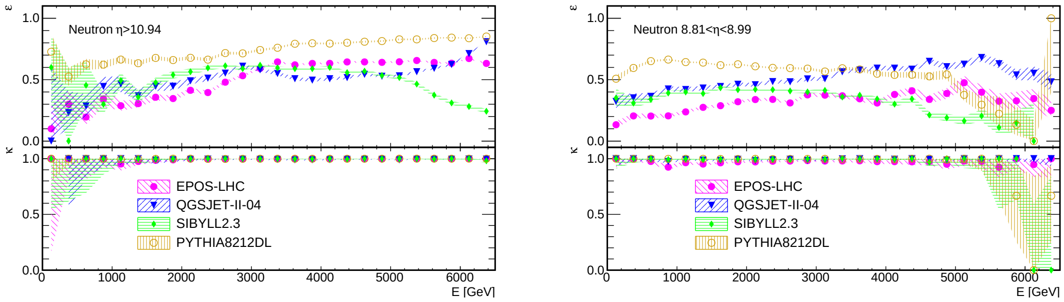

(a) $\eta > 10.94$

(b) $8.81 < \eta < 8.99$

FIGURE 4.9: Efficiency (top) and purity (bottom) of diffraction selection for the VF ((a) $\eta > 10.94$ and (b) $8.81 < \eta < 8.99$) neutron spectra obtained by using the central-veto technique.

4.4.2 Performance of ATLAS-veto selection

To evaluate the performance of central-veto selection based on the VF spectra, the VF spectra were classified as non-diffractive-like and diffractive-like. A comparison of the VF neutron and π^0 spectra in the VF regions is shown in Figs. 4.8 and 4.10, respectively. They indicate that the spectra corresponding to events surviving central-veto selection keep almost the same shapes as the VF true diffractive spectra. Moreover, the number of misidentified diffractive-like events is very small, as shown by the red histograms. Comparisons of the differential cross sections of surviving events from central-veto selection are shown in the bottom plots of Figs. 4.9 and 4.11. The differences among models are expected to be constrained directly by using experimental data. The efficiency and purity of central-veto selection as function of energy were calculated with Eq. 4.1 and Eq. 4.2, as shown in Figs. 4.9 and 4.11. It is clear that selection purity stays constantly high (at $\approx$ 100%), independent of particle type, energy, and MC simulation model, whereas selection efficiency has a tendency to increase with increasing energy. In contrast to selection purity, selection efficiency exhibits differences among MC simulation models. In particular, the bump structure in EPOS-LHC and QGSJET-II-04 mentioned above still remains on the efficiency spectra. In such a case, comparing measured data with the MC samples as shown in Figs. 4.8 and 4.10 can not only constrain the diffraction cross sections in the VF region but also help in identifying the inherent problems in the model.

4.4.3 Low-mass diffraction

The high-mass diffraction cross sections $d\sigma^{SD}/d\Delta\eta$ at the LHC energies were measured by ATLAS [50, 51], CMS [52, 53], and ALICE [54]. Due to the limited acceptance of these detectors, the typical rapidity gap signatures identified by these detectors are around $-6 < \log_{10}(\xi_x) < -2$. In the case of ATLAS, such signatures correspond to the lower and upper limits of M_X of ~13 and 1300 GeV at $\sqrt{s} = 13$ TeV, respectively. This fiducial region excludes the measurement of low-mass diffraction for determination of the total inelastic cross sections. While, low-mass diffraction is the main source of systematic uncertainties [51, 52] in the determination of inelastic cross sections.

Roman Pot detectors and VF-detector have sensitivities to low-mass diffractive processes. Roman Pot detectors are able to measure the differential cross sections based on the indirect method, which subtract the cross sections of high-mass diffraction from the total inelastic collisions. On the other hand, VF-detector is capable of direct measurements, such as the differential cross sections of $d\sigma/dE$, $d\sigma/d\eta$. To evaluate the performance of VF-detector for the detection of low-mass diffraction, the LHCf detector

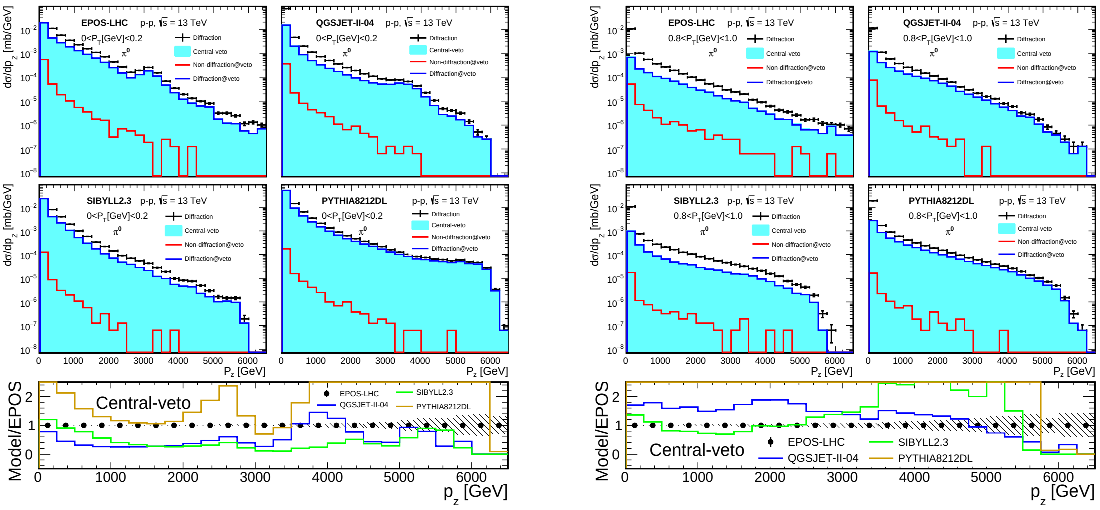

(a) $0 < p_T < 0.2$ GeV (b) $0.8 < p_T < 1.0$ GeV

FIGURE 4.10: π^0 spectra at (a) $0 < p_T < 0.2$ GeV and (b) $0.8 < p_T < 1.0$ GeV generated by EPOS-LHC, QGSJET-II-04, SIBYLL 2.3, and PYTHIA 8212DL. The top four panels show the spectra of true diffraction (black lines) and diffractive-like events corresponding to central-veto selection (filled gray areas), which are defined as events without any $p_T > 100$ MeV charged particles at $|\eta| < 2.5$; in addition, the central-veto events were classified by non-diffraction (red) and diffraction (blue) again according to MC true information. The bottom plots show the ratios of the central-veto spectrum of each model to the central-veto spectrum of EPOS-LHC.

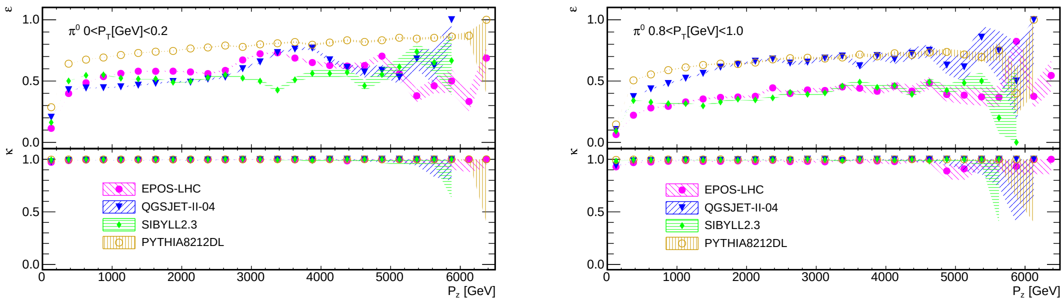

(a) $0 < p_T < 0.2$ GeV (b) $0.8 < p_T < 1.0$ GeV

FIGURE 4.11: Efficiency (top) and purity (bottom) of diffraction selection for the VF ((a) $0 < p_T < 0.2$ GeV and (b) $0.8 < p_T < 1.0 GeV$) π^0 p_z spectra obtained by using the central-veto technique.

is considered as representative. The acceptances of the LHCf detector for the forward neutral particles predicted by MC interaction models are shown in Fig. 4.12. In the region of $\log_{10}(\xi_x) > -5.5$, the SD detection efficiency of the LHCf detector is only a few percent. The detection efficiency, however, increases below $\approx\log_{10}(\xi_x) = -6$ and reaches a maximum of $\sim$40% at $\log_{10}(\xi_x) = -8$. In contrast, central detectors exhibit a totally opposite tendency of detection efficiency. For instance, the ATLAS detector has almost 100% SD detection efficiency in the region of $\log_{10}(\xi_x) > -5$ but decreases rapidly to 0 at $\log_{10}(\xi_x) = -7$ [69]. Therefore, the common experiment using central and VF detectors can enhance detection efficiency, especially for low-mass processes.

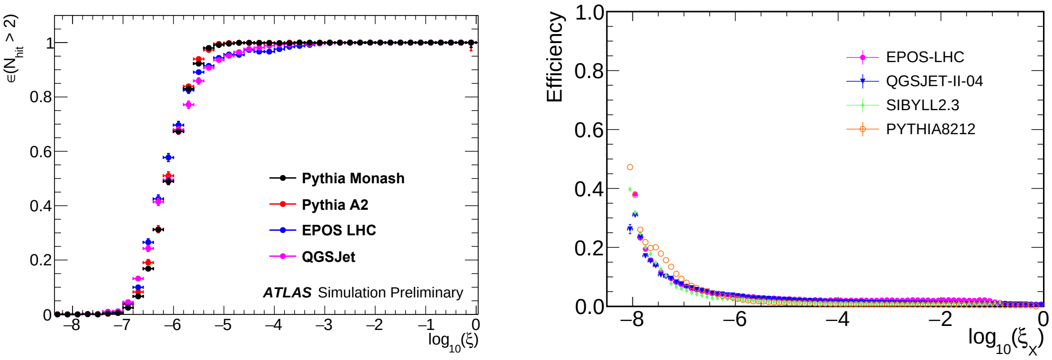

(a) ATLAS trigger efficiency [69]

(b) LHCf trigger efficiency

FIGURE 4.12: LHCf and ATLAS detection efficiency as a function of $\log_{10}\xi_X$, which is simulated by four MC simulation samples. The trigger conditions for LHCf detectors at $\sqrt{s} = 13$ TeV are $E_\gamma > 200$ GeV and $E_h > 500$ GeV. Only the SD ($pp \to pX$) component is used for this calculation. The trigger conditions for ATLAS are described [69].

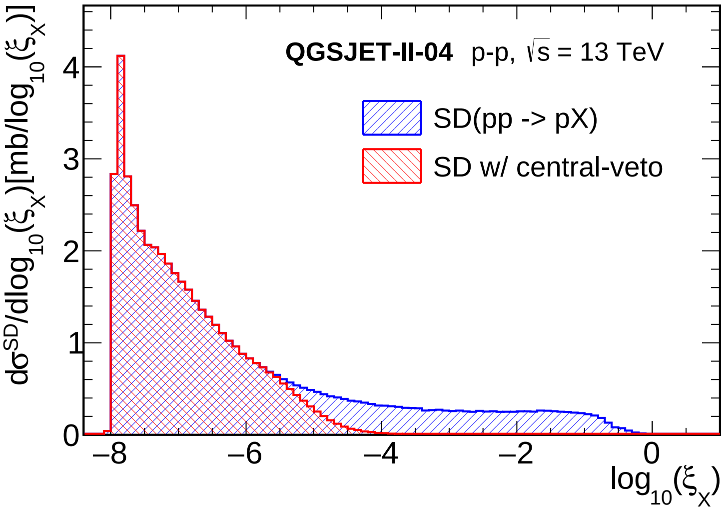

FIGURE 4.13: SD ($pp \to pX$; blue) cross section as a function of $\log_{10}\xi_X$ predicted by QGSJET-II-04 MC samples. This is compared with the SD cross section after applying the central-veto selection (red).

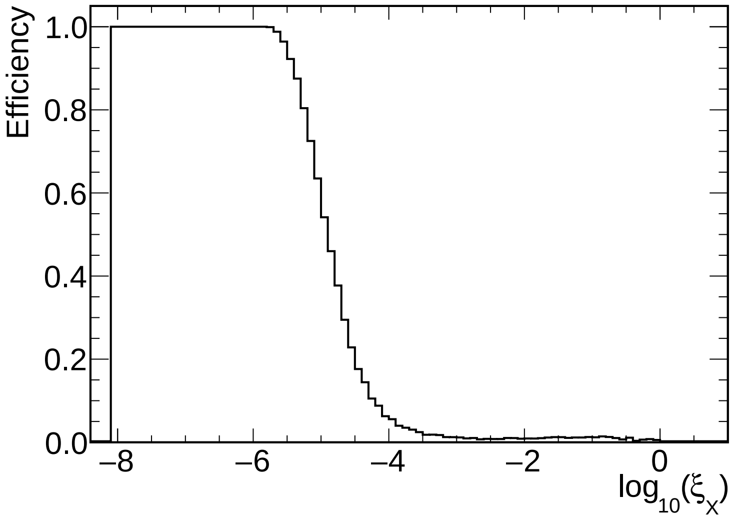

FIGURE 4.14: The detection efficiency of SD ($pp \to pX$; blue) based on central-veto selection, as a function of $\log_{10}\xi_X$ predicted by QGSJET-II-04 MC samples. The selection efficiency is about 100% for $M_X < 20$ GeV ($\log_{10}\xi_X <$ -5.6) and decreases to $\sim$ 10% for $M_X = 100$ GeV ($\log_{10}\xi_X \sim$ -4.2).

According to the predictions of QGSJET-II-04 and PYTHIA8212DL, most of the events survived from the central-veto selection are from the low-mass diffraction independent of the types of diffractions, as shown in Fig. 4.13 and Fig. 4.15. The blue hatched histogram shown in Fig. 4.13 indicates the SD cross section as a function of $\log_{10}(\xi_X)$ predicted by QGSJET-II-04, the red hatched histogram shows the SD cross section of the events selected by applying the central-veto. Similarly, the DD cross section as a function of $\log_{10}(\xi_i)$ was shown as a scatter plot in Fig. 4.15 (a), Figure 4.15 (b) indicates the DD cross section of the events survived from the central-veto selection. In particular, according to Fig. 4.14 and Fig. 4.16, all the low-mass diffractive events at $\log_{10}(\xi_i) < -5.5$ detected by VF-detector survived from the central-veto selection, whereas all the high-mass diffractive events at $\log_{10}(\xi_i) > -4$ were excluded. In other word, the filled histogram in Figs. 4.8 and 4.10 are mostly derived from the low-mass diffractive processes at $\log_{10}(\xi_x) < -5.5$. Therefore, the common experiment by combining VF and central detectors can provide a unique chance to access the low-mass diffraction region directly, which has been already measured indirectly by TOTEM [55]. Such measurement is able to give the first constraint on the treatment of low-mass diffraction implemented in MC simulation models, through VF neutral particle spectra.

As shown in Fig. 4.1, there are big discrepancies among the cross sections of low-mass diffraction predicted by several models. Such discrepancies can directly affect the predictions of forward neutral particle production measured by LHCf. To investigate the different implementation of low-mass diffraction in the MC simulation models,

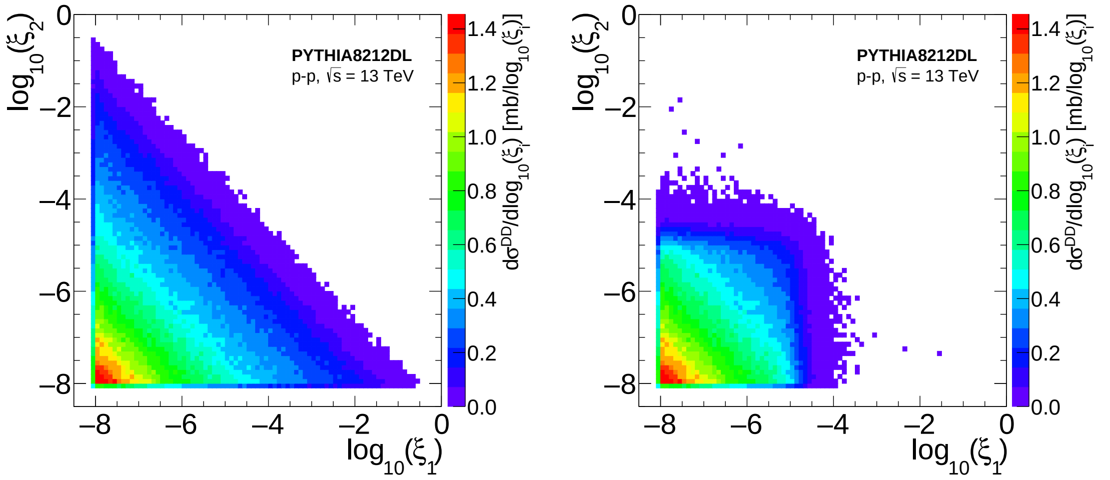

(a) Double diffraction cross sections

(b) Double diffraction cross sections selected by central-veto

FIGURE 4.15: DD ($pp \rightarrow X_1X_2$) cross section as a function of $\log_{10}\xi_i$ predicted by PYTHIA8212DL MC samples (a). Figure (b) indicates the DD cross section after applying the central-veto selection.

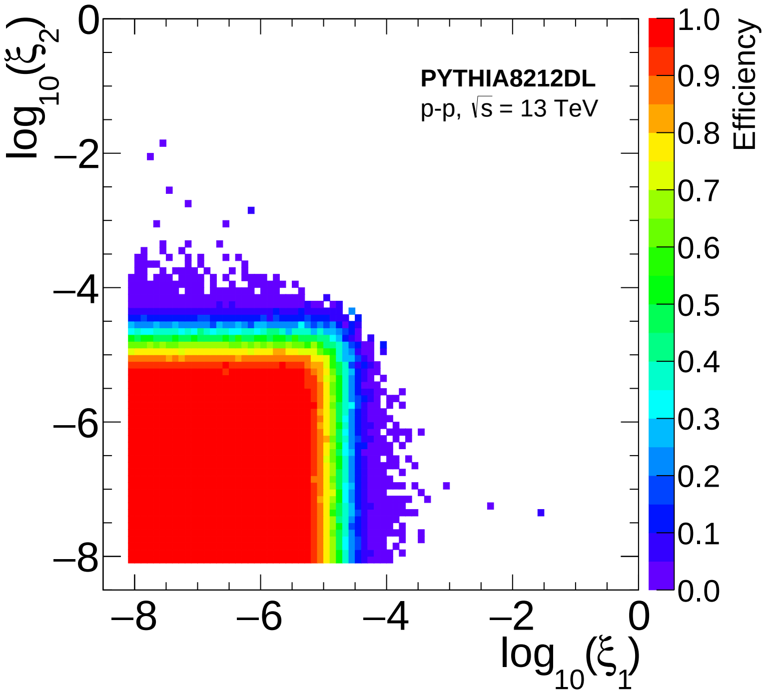

FIGURE 4.16: The detection efficiency of DD ($pp \rightarrow X_1X_2$) by applying the central-veto selection, as a function of $\log_{10}\xi_i$ predicted by PYTHIA8212DL MC samples.

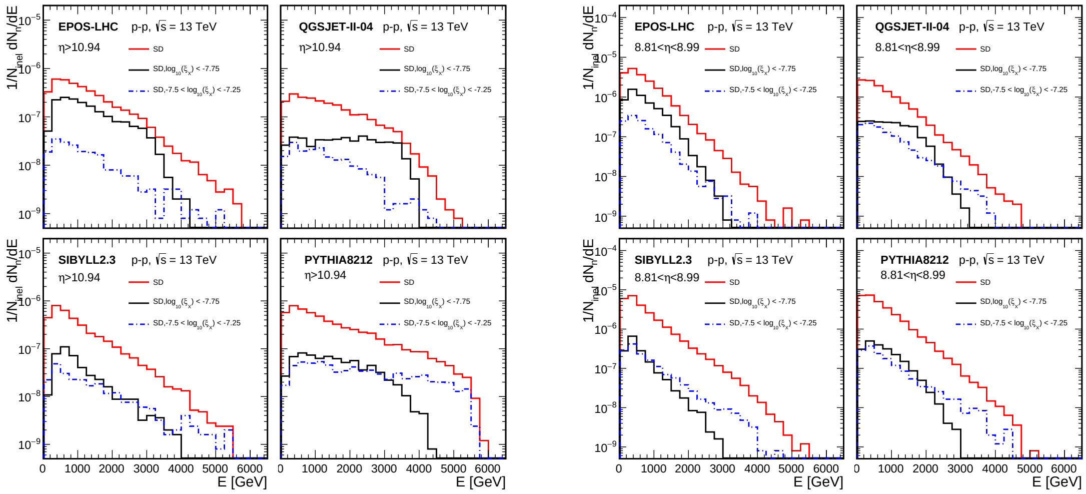

(a) $\eta > 10.94$

(b) $8.81 < \eta < 8.99$

FIGURE 4.17: Photon spectra at (a) $\eta > 10.94$ and (b) $8.81 < \eta < 8.99$ generated by EPOS-LHC, QGSJET-II-04, SIBYLL 2.3, and PYTHIA 8212. The four panels show the spectra of true diffraction (red line) and diffractive-like events in the region of $\log_{10}(\xi_x) < -7.75$ (black line) and $-7.5 < \log_{10}(\xi_x) < -7.25$ (blue dot-dash line) corresponding to central-veto selection, which are defined as events without any $p_T >$ 100 MeV charged particles at $|\eta| < 2.5$.

a study was done to compare VF neutral particle spectra at the dedicate low-mass interval. As shown in Fig. 4.17 and Fig. 4.18, the photon and neutron spectra at (a) $\eta > 10.94$ and (b) $8.81 < \eta < 8.99$, were predicted by EPOS-LHC, QGSJET-II-04, SIBYLL2.3 and PYTHIA8212. The red histogram shows the spectra from SD processes, the black and blue histograms from SD with diffractive mass of $\log_{10}(\xi_x) < -7.5$ and $-7.5 < \log_{10}(\xi_x) < -7.25$, respectively. Both black and blue histograms show the contribution from very low-mass SD. There are big discrepancies among the models. In particular, the neutron spectra derived from the SD in the mass range of $\log_{10}(\xi_x) < -7.5$ have a large contribution at $\eta > 10.94$, while, almost have no contribution at $8.81 < \eta < 8.99$. The different treatments of the resonances in each models are assumed to make the corresponding differences. Therefore, the differential cross sections of neutral particles derived from low-mass diffraction can point out the specific problems implemented in the models.

4.4.4 Identification of low-mass single and double diffractive processes

As described in the last section, the central-veto selection based on ATLAS ID data is an effect way to categorize the LHCf observables into low-mass diffraction or the others. In the ATLAS-LHCf joint analyses, it will turn the LHCf data more powerful by also using the ATLAS MBTS data. The MBTS hit data can be used to classify

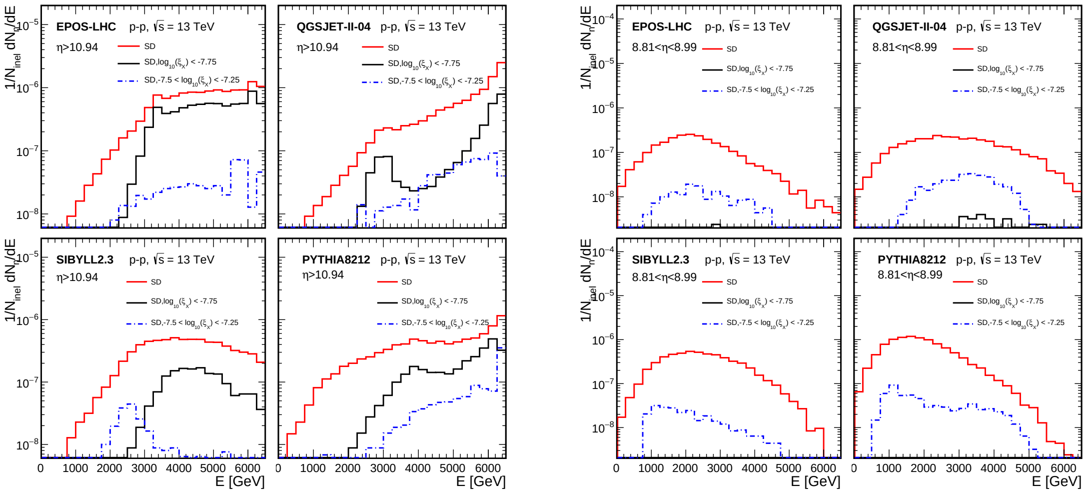

(a) $\eta > 10.94$

(b) $8.81 < \eta < 8.99$

FIGURE 4.18: Neutron spectra at (a) $\eta > 10.94$ and (b) $8.81 < \eta < 8.99$ generated by EPOS-LHC, QGSJET-II-04, SIBYLL 2.3, and PYTHIA 8212. The four panels show the spectra of true diffraction (red line) and diffractive-like events in the region of $\log_{10}(\xi_x) < -7.75$ (black line) and $-7.5 < \log_{10}(\xi_x) < -7.25$ (blue dot-dash line) corresponding to central-veto selection, which are defined as events without any $p_T >$ 100 MeV charged particles at $|\eta| < 2.5$.

the low-mass diffractions into furthermore specific diffractive types; single and double diffractions. The ATLAS MBTS data has already been widely used in the measurement of total inelastic cross section and charged particle production at $\sqrt{s} = 13$ TeV *p*-*p* collisions [68, 70]. As illustrated in Fig. 4.20, MBTS covers the pesudorapididty range of -3.86 < η < -2.08 and 2.08 < η < 3.86, respectively. If we assume the dissociated system of projectile proton was observed by LHCf Arm1 detector, similarly there is no charged particle observed in ATLAS ID detector, then MBTS on LHCf Arm2 side detected hits from the dissociated system of target proton, accordingly the corresponding event can be identified as double diffraction. So that the particles observed by LHCf Arm1 detector can be identified as that they are derived from low-mass double diffraction.

Figure 4.19 shows the comparisons of LHCf photon spectra which are classified into non-diffraction, single-diffraction, and double-diffraction based on the MC true flags at $\eta > 10.94$ and $8.81 < \eta < 8.99$. The spectra of SD and DD predicted by each model have similar shapes. However, QGSJET-II-04 give the most close differential cross-section between SD and DD. SIBYLL2.3 predicted more SD photons than DD photons in the LHCf phase space, while, EPOS-LHC and PYTHIA8212DL predicted the opposite tendency. The differences of photon production from SD and DD processes in the very forward regions are very large among models.

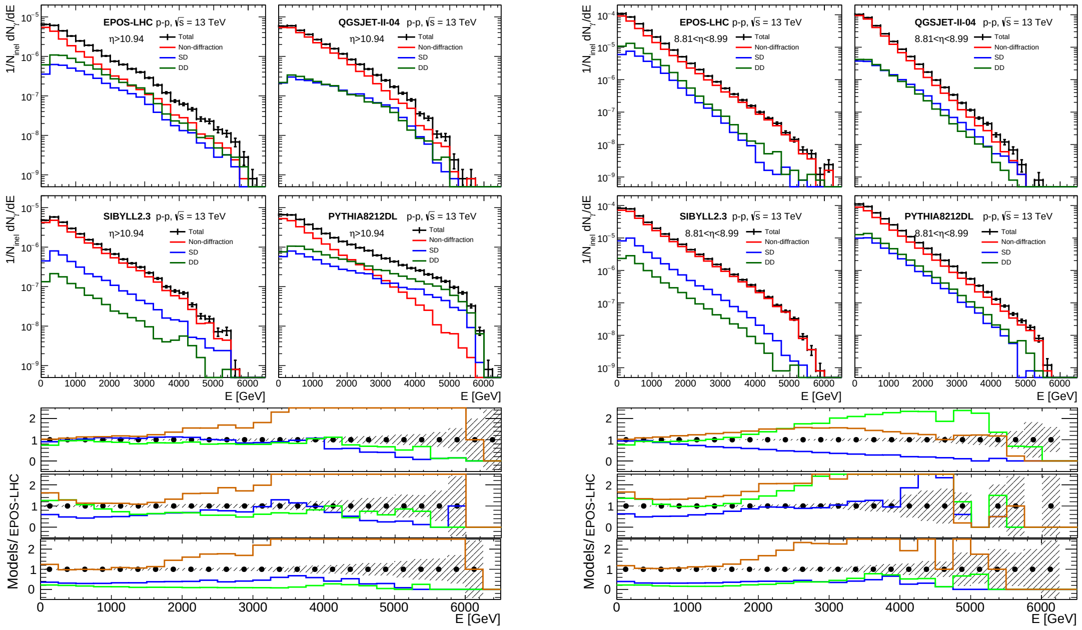

(a) $\eta > 10.94$

(b) $8.81 < \eta < 8.99$

FIGURE 4.19: Photon spectra at $\eta > 10.94$ (left) and $8.81 < \eta < 8.99$ (right) (top four panels in each set). These are generated by EPOS-LHC, QGSJET-II-04, SIBYLL 2.3, and PYTHIA 8212DL, respectively. The total photon spectra (black) were classified by non-diffraction (red) and single-diffraction (blue) and double-diffraction (green) according to MC true flags. The bottom three plots show the ratios of the spectra of EPOS-LHC (black markers), QGSJET-II-04 (blue lines), SIBYLL 2.3 (green lines), and PYTHIA8212DL (orange lines) to the spectrum of EPOS-LHC. The top, middle, and bottom plots correspond to total, single-diffraction, and double-diffraction, respectively.

To investigate the dedicated fiducial diffractive mass range by applying the MBTS selection, a study was done based on the prediction of PYTHIA8212DL. The scatter plot of Fig. 4.21 shows the DD cross section as a function of $\log_{10}\xi_i$, where ξ_i is momentum fraction lost by proton defined in Eq. 2.16. The selected events are triggered by LHCf Arm1 detector and passed central-veto selection, besides there are hits detected by MBTS on LHCf Arm2 side. X axis ($\log_{10}\xi_1$) indicates the diffractive mass of the dissociated system on LHCf Arm1 side, the MBTS hits requirement do not effect it.

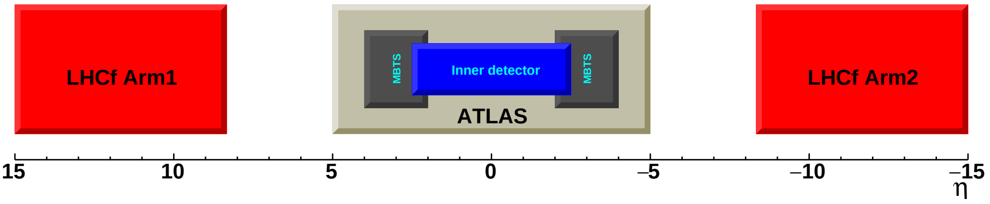

FIGURE 4.20: Pseudo-rapidity acceptance of ATLAS Inner detector, MBTS and LHCf detectors.

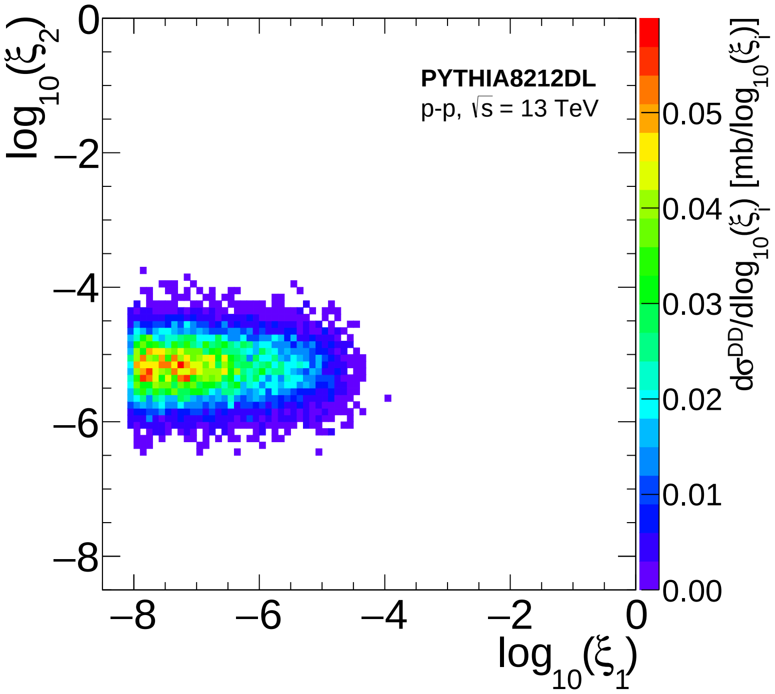

FIGURE 4.21: DD ($pp \to X_1X_2$) cross section as a function of $\log_{10}\xi_i$ detected by LHCf based on the prediction of PYTHIA8212DL MC samples, The corresponding events are detected by LHCf and passed the central-veto selection and MBTS selection.

While, y axis corresponding to the diffractive mass of the dissociated system on LHCf Arm2 side, the central-veto selection and MBTS hits requirement selected the events only have diffractive mass at the range of -6 < $\log_{10}\xi_2$ < -4. Figure 4.22 shows the detection efficiency of low-mass double diffraction, by comparing Fig. 4.21 and Fig. 4.15 (a). Only 1-5% of events derived from low-mass double diffraction survived from the requirement of triggering by LHCf Arm1 detector and passing the selection of ATLAS ID and MBTS selection.

4.5 Summary

We studied the non-diffractive and diffractive contributions to VF particle production using MC predictions in *p*–*p* collisions at $\sqrt{s} = 13$ TeV. For the forward photon and π^0 energy spectra, PYTHIA8212DL predicts the largest diffractive contributions at high energies. In the cases of neutron differential cross sections at high energies, EPOS-LHC and PYTHIA8212DL are dominated by diffraction at $|\eta| > 10.94$ while QGSJET-II-04 and SIYBLL2.3 are dominated by non-diffraction.

The identification of diffraction based on the rapidity gap technique has been investigated. We studied the performance of an effective selection criterion for diffractive events

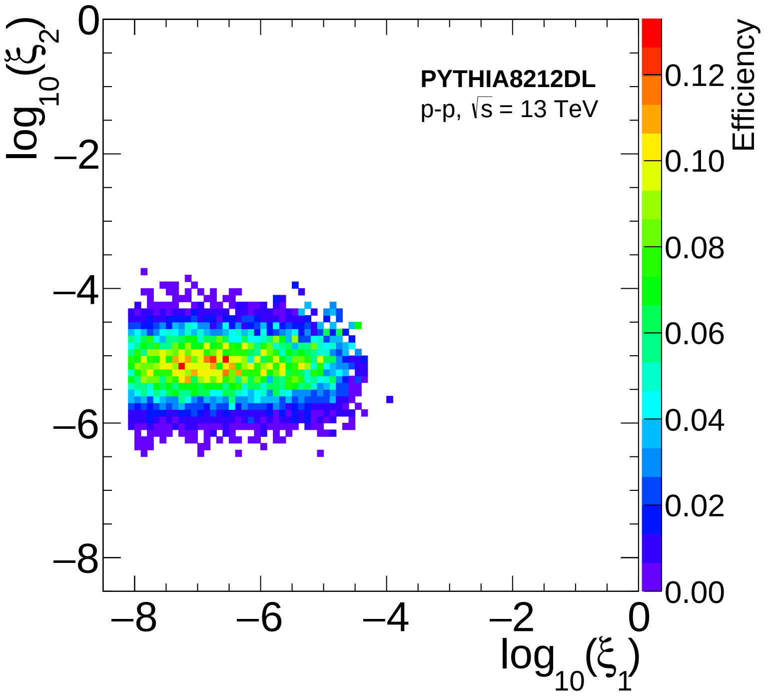

FIGURE 4.22: The efficiency of DD ($pp \to X_1X_2$) as a function of $\log_{10}\xi_i$ detected by LHCf based on the predictions of PYTHIA8212DL MC samples. The selected events are detected by LHCf and passed the central-veto selection and MBTS selection.

(central-veto selection): "There are no charged particles ($N_{track} = 0$) in the kinematic range $|\eta| < 2.5$ and $p_T > 100$ MeV". Such a selection has ≈100% purity, independent of particle type, energy, and interaction model whereas selection efficiency increases from ∼30% to 70% with increasing energy. The surviving events from central-veto selection are mostly low-mass diffraction events in the phase space of $\log_{10}(\xi_x) < -5.5$. This indicates that the combined experiment can purify the detection of low-mass diffraction. Such mass range was not accessible by the experiments using the changed particle tracker. Furthermore, it can turn the VF data more powerful by using the larger pesudorapidity data of central detector, such as the ATLAS MBTS data. The MBTS hit data can be used to identify the low-mass diffractions into furthermore specific diffractive types; single and double diffractions.

Clearly, non-diffraction and diffraction have different contributions in the VF regions, while hadronic interaction models also exhibit big differences among each other. The rapidity gap measurement (central-veto technique) using central information is an effective way to identify diffractive events and classify the forward productions to non-diffraction and diffraction. Furthermore, using the observed events, it is capable of both constraining the differential cross sections ($d\sigma/dE$, $d\sigma/d\eta$) of low-mass diffraction and helping to identify the inherent problems in the models corresponding to low-mass diffraction.

In this study, we focus on the diffraction issues by using the combinations of VF observables and central tagging information. Such apparatus is also capable of contributing to several unique measurements, for instance, the p–π^+ and π^+–π^+ cross sections [71–73] by tagging the leading neutrons derived from the pion–exchange processes in VF detector. The coincidence analysis of data from two arm detectors will be a possibility to identify the type of diffraction. Furthermore, the common experiment of central-VF-RP detectors could be a more powerful apparatus for diffraction study.

Chapter 5

Measurement of contributions of diffractive processes to forward photon spectra in p-p collisions at $\sqrt{s} = 13$ TeV with the ATLAS-LHCf detector

5.1 Overview

The ATLAS [56] and LHCf [34] experiments had a common data acquisition in p-p collisions at the centre-of-mass energy of $\sqrt{s} = 13$ TeV. In a joint analysis between ATLAS and LHCf experiments studied the diffractive contribution to very forward neutral particle production for the first time, especially, the joint analysis is the first direct measurement of the very low-mass diffractive dissociations at very high energies. The results are based on data collected in 2015 with a corresponding integrated luminosity of 0.191 nb^{-1}. The forward photon energy spectra are measured by the LHCf-Arm1 detector in the pseudorapidity range of $8.81 >|\eta| < 8.99$ or $|\eta| > 10.94$, for events originating predominantly from low-mass diffraction with no reconstructed charged-particle tracks measured by the ATLAS inner tracker with $p_T > 100$ MeV and $|\eta| < 2.5$. The results are compared to predictions from several hadronic interaction models.

5.2 The LHCf and ATLAS detectors

The detail information about the LHCf detectors is described in Ref. [34], and also summarised in Chapter 3. The ATLAS detector is described in detail in Ref. [56]. The ATLAS inner tracker consists of a silicon pixel detector (pixel) located close to the beam line and a silicon microstrip detector (SCT) surrounding the pixel detector. The transition radiation detector (TRT) is located outside the SCT. The tracker covers the full azimuthal angle region and the pseudorapidity range of $|\eta| < 2.5$ and is immersed in a 2 T solenoidal magnetic field. ATLAS uses a two-level trigger system to select events as already mentioned in Chapter 3. The first-level trigger (hardware trigger system) is implemented with a subset of information from each sub-detector system. This is followed by the high-level trigger system, which is software-based and can run the offline reconstruction and calibration software, further reducing the event rate to an average of 1 kHz.

5.3 Data set

The experimental data used in this analysis was obtained during the run taken from 22:32 to 1:30 (CEST) on June 12-13, 2015 during pp collisions at $\sqrt{s} = 13$ TeV. The run was delivered as a special low luminosity run, which accomplished by controlling the separation of two beams to keep the mean number of interactions per a bunch crossing, μ, around 0.01. As shown in Fig. 5.1, the instantaneous luminosity recorded by ATLAS experiment during these data-taking conditions was $(3-5)\times 10^{28}$ cm^{-2}s^{-1}. Considering that the live fraction of the LHCf DAQ system [74] which are defined as the ratio of the number of the LHCf recored events over the number of triggers including those lost due to dead-time of the DAQ system, is about 50%, the total integrated luminosity of the analyzed data-set is estimated to be (0.191 ± 0.04) nb^{-1}. In this analysis, 2.1×10^6 events triggered by the LHCf-Arm1 detector are used.

The LHCf triggers were issued when any successive three layers in the calorimeters have energy deposit over a certain threshold. The trigger efficiency was 100 % for photons with energy over 200 GeV. All LHCf final triggers except the pedestal and calibration triggers were sent to the trigger processor of ATLAS and generated ATLAS first-level triggers without pre-scaling the LHCf trigger signals. The LHCf triggered event passed through the ATLAS high-level trigger process without any reconstructions and selections. The obtained data by LHCf and ATLAS was independently recorded in each local disk. Matching the events recorded on both LHCf and ATLAS data was performed offline after the event reconstruction discussed in Sec. 5.6. LHCf recorded one of the ATLAS

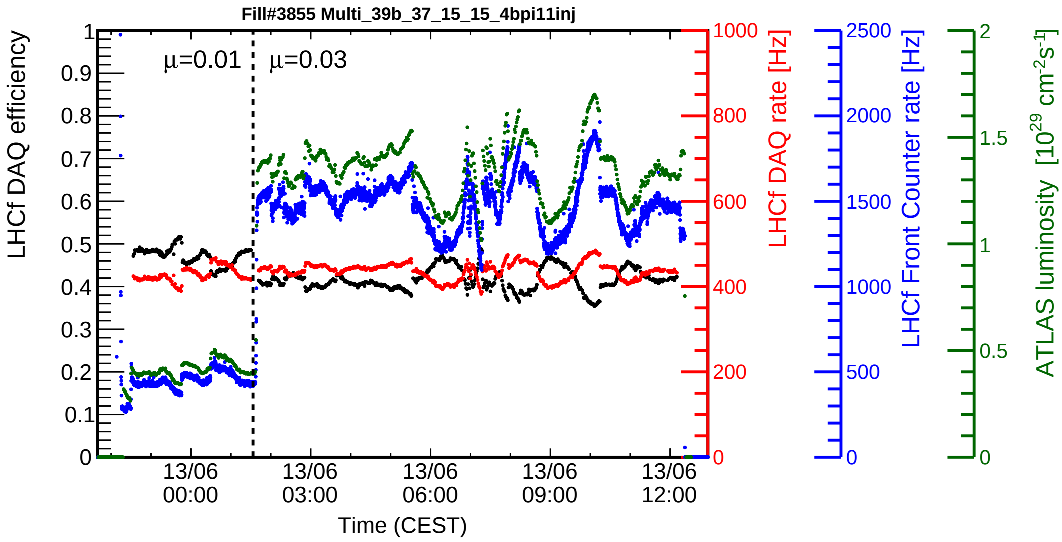

FIGURE 5.1: LHCf DAQ performance and ATLAS recorded luminosity during Fill 3855. The DAQ live time (black), DAQ rate (red), count rate of Front Counter (blue) of the LHCf experiment and the luminosities (green) measured by the ATLAS experiment are shown, respect ively. The beam condition was changed at the time around the vertical dotted line shown in the plot, the pile up parameter μ was tuned form 0.01 to 0.03. The data used in the joint analysis corresponding to the period with μ=0.01.

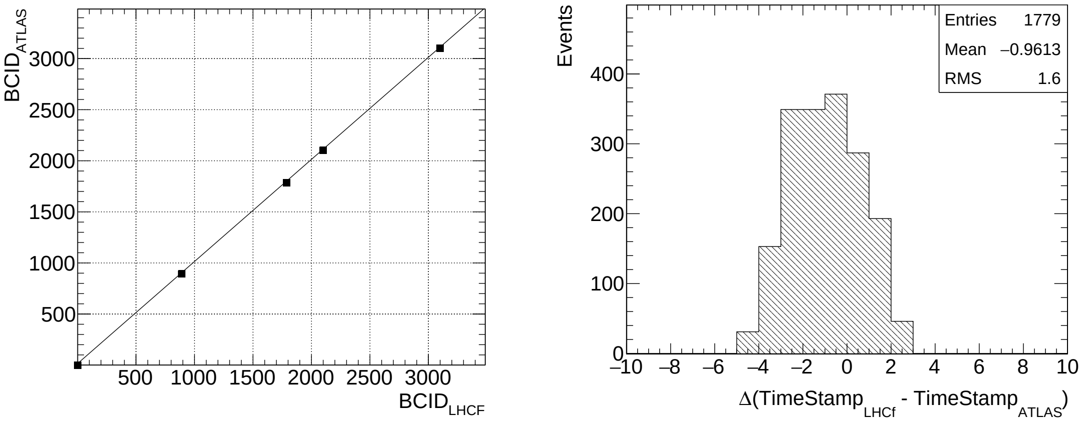

(a) Bunch ID

(b) Differences of time stamp

FIGURE 5.2: (a) Bunch ID of matched events recorded by LHCf and ATLAS, (b) Differences of time stamp recorded by ATLAS and LHCf for the matched events. The event matching was correctly done confirmed by using bunch ID and time stamp.

event-ID's, Level1-ID, event-by-event. The ATLAS Level1-ID was used for the event matching. Additionally, as shown in Fig. 5.2 the time stamp and the bunch ID of each matched event were checked confirming that the matching was successfully done.

5.4 MC simulation

Several Monte Carlo (MC) samples were produced to compare to the experimental data and to correct the data for detector effects.

The MC samples are based on four hadronic interaction models EPOS-LHC[21], QGSJET-II-04 [22], SYBILL 2.3 [23, 24], and PYTHIA 8212DL [25, 26]. 2×10^7 pp inelastic collisions at $\sqrt{s} = 13$ TeV for each hadronic interaction model were generated. The first three models are widely used to simulate the cosmic-ray air-shower in the atmosphere, where as PYTHIA8 is widely used in collider physics. The pp event simulation samples were generated by using the integrated interface tool CRMC v1.6.0 [60], whereas for PYTHIA, its own front-end was used. The Monash event tuning [61] is used for the PYTHIA8 MC samples. In addition, the Donnachie and Landshoff (DL) model [63] with a linear pomeron trajectory $\alpha_P(t) = 1 + \Delta + \alpha^{'} t$ was used to define the diffractive dynamics. According to the ATLAS inelastic cross section measurement in pp collisions at $\sqrt{s} = 13$ TeV, the PYTHIA 8212DL model with these parameters gives the best description of the number of hits detected by the minimum-bias trigger scintillators which is very sensitive to the diffractive cross section [70]. The default values of the parameters Δ and $\alpha^{'}$ are 0.085 and 0.25 GeV^{-2} [46], respectively. In these pp event simulations, only decays of produced particles with a mean lifetime smaller than 30 ps are treated.

The LHCf detector simulation [37] is used to estimate detector response and corrections to the fiducial measurement of the photon energy spectrum. For these purposes, 10^8 and 5×10^7 events of pp inelastic interactions were generated using the QGSJET-II-04 and EPOS-LHC MC generators, respectively. These two models were selected as baseline event generators since both show relatively good agreement with the LHCf inclusive photon and π^0 data at $\sqrt{s} = 7$ TeV [36, 42]. The data and MC simulated events are passed through the same reconstruction and analysis software.

To estimate the efficiency of the track reconstruction of the ALTAS inner detector, the η- and p_{T}-dependent response functions is determined using a simulation of ATLAS detector based on GEANT4 [75, 76] and a PYTHIA8 simulated events. A special track reconstruction algorithm to reconstruct low-momentum tracks with a transverse momentum of $p_{\mathrm{T}} > 100$ MeV was applied during the event reconstruction. The track detection efficiency is defined as the ratio of the number of reconstructed tracks matched to generated primary charged particles to the number of generated primary charged particles. The hits are weighted such that all subdetectors have the same weight in the sum. A track is considered to be matched to a generated particle if the weighted fraction of track hits originating from that particle exceeds 50%. Primary charged particles are defined as charged particles with a mean lifetime greater than 300 ps, either produced directly

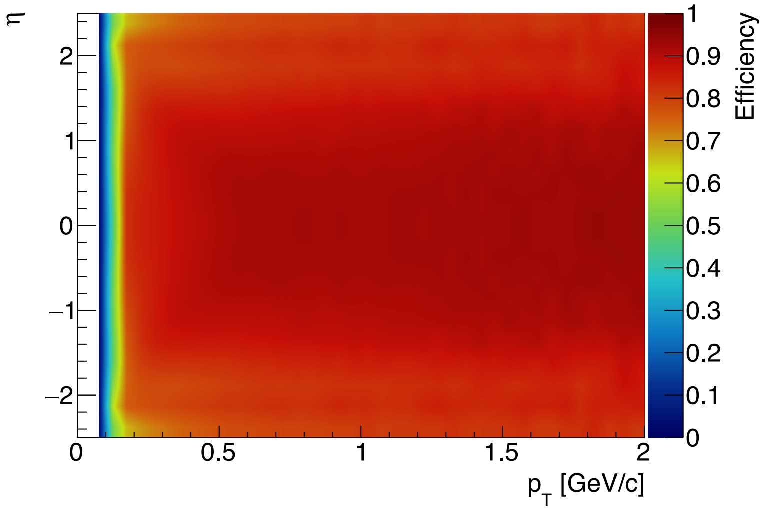

FIGURE 5.3: The detection efficiency of ATLAS Inner detector for π^+ as functions of η and p_T.

in a pp interaction or from subsequent decays of directly produced particles with lifetime smaller than 30 ps. Figure 5.3 shows the estimated track detection efficiency of π^+'s as functions of p_T and η. The efficiency for charged particles with p_T over 2.0 GeV/c was assumed as the same efficiency at 2.0 GeV/c. The six functions were prepared for π^+, π^-, K^+, K^-, p and $\overline{p}$. If a charged particle generated in a collision was other than the six particles, the function for the particle-type with the same charge and the closest mass to the particle in the six particle-types, was used. For example, the function for π^-'s was used for electrons. The track reconstruction efficiency increases from about 23-59% at p_T = 100 MeV depending on η and the particle type to about 90% at p_T = 400 MeV and becomes constant for $p_\mathrm{T} >$ 400 MeV.

The detector simulations are also used to derive several systematic uncertainties. The output of event generators for the pp collisions is labeled as "MC samples" in the following, if not stated otherwise. In several cases, it was not possible to apply the full ATLAS detector simulation to the generator predictions. In these cases, dedicated response functions describing the track reconstruction efficiency of the ATLAS inner tracker system have been applied directly to the generator level MC samples. Those will be labeled as "MC-folded samples" in the following.

5.5 The inclusive photon spectrum measured by LHCf

The inclusive photon spectra measured by LHCf was reported in Ref. [37]. The observables measured by the LHCf calorimeters are mainly photons and neutrons. In the LHCf

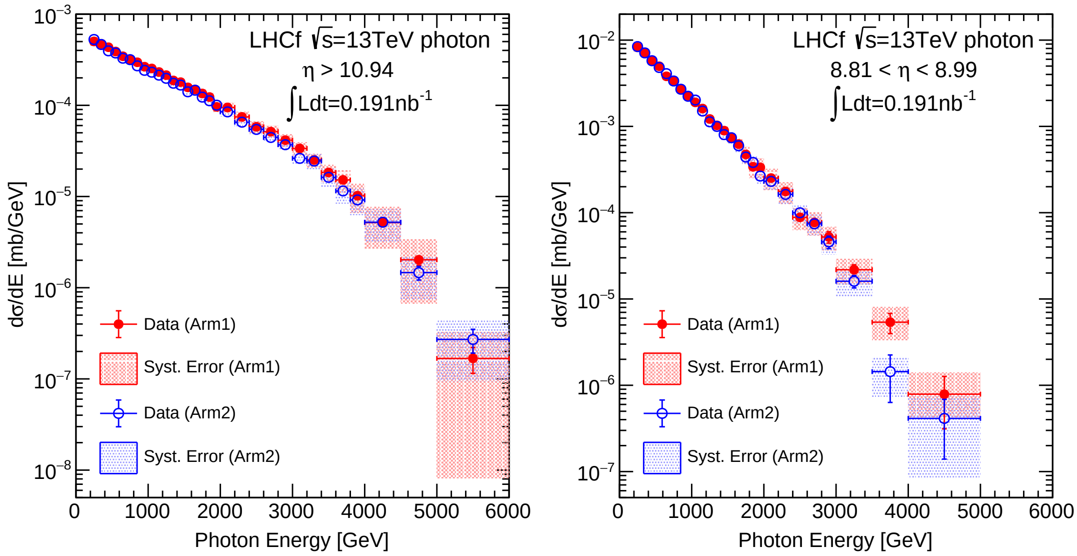

FIGURE 5.4: The photon energy spectra in *p*-*p* collisions at $\sqrt{s} = 13$ TeV. The left and right pads corresponding to the spectra at RegionA and RegionB, respectively. The red and blue markers associated with color area show the Arm1 and Arm2 data with systematic uncertainties, respectively.

standalone photon analysis, the reconstructed events were selected which passed the selection criteria of particle identification (PID) of photon. Due to the LHCf calorimeters are single pixel detectors, the multi-hit events which two or more particles hit a single calorimeter tower were rejected. The number of hits was counted by using the position sensitive detectors. Two fiducial regions located on each small and larger calorimeters were defined to select the photons, which correspond to pseudorapidity regions of $|\eta| > 10.94$ and $8.99 > |\eta| > 8.81$. The inefficiency of the detection of multi-hit events and the contamination of hadrons due to the mis-PID, were corrected based on the MC simulation. The detector biases in the obtained spectra were corrected by using the unfolding technique. Figure 5.4 shows the photon energy spectra measured by LHCf two independent detectors Arm1 and Arm2. By comparing the results of two detector, we found they agree with each other within the given uncertainties. Then two independent results were combined by using an approach that assumed the systematic uncertainties are both bin-by-bin corrected and Arm1-Arm2 no corrected, except the systematic uncertainties from luminosity and unfolding. The combined results of two detector are shown in Fig. 5.4, the data are compared with model predictions.

5.6 Analysis

5.6.1 Analysis strategy

As shown in Fig. 5.4, the inclusive energy spectrum of forward photons in the 200 GeV $< E_\gamma <$ 6 TeV range, has been measured in two well-defined kinematic regions of the LHCf -Arm1 detector. In this analysis, the main goal is to classify the inclusive photon spectrum into the photons derived from the diffractive-like or non-diffractive-like processes, according to the presence of at least one charged particle track with p_T >100 MeV and $|\eta| < 2.5$ (ATLAS-veto: no change particle track with p_T >100 MeV and $|\eta| < 2.5$). In order to be directly compared with the generator's output, the measured diffractive-like spectrum which passes the ATLAS-veto selection should be corrected and unfolded, as like the inclusive photon spectrum.

The resulting photon spectra are normalized to the expected number of inelastic collisions, N_{inel}, calculated as $N_{inel} = L_{int}\ \sigma_{inel}$, where L_{int} is the total integral luminosity calculated base on the instantaneous luminosity recorded by ATLAS as shown in Fig. 5.1, and $\sigma_{inel} = 78.1 \pm 2.9$ mb is the inelastic pp cross section measured at $\sqrt{s} = 13$ TeV by ATLAS [70].

5.6.2 Fiducial region definition

The fiducial phase space of the measurement consists of two exclusive regions. Figure 5.5 shows the hit-map of the selected events on the LHCf-Arm1 detector. Region A covers the area of a half-disk shape with $R < 5$ mm and azimuthal angle, $-135° < \phi < 45°$ (denoted as $\Delta\phi < 180°$), where R is the distance from the beam center. Region B is defined by the sector-shape area for which 35 mm $< R <$ 42 mm and $80° < \phi < 100°$ (denoted as $\Delta\phi < 20°$). Regions A and B correspond to the pseudorapidity regions of $\eta > 10.94$ and $8.81 < \eta < 8.99$, respectively. Events are required to contain at least one photon with an energy threshold above 200GeV. At the particle level, all photons produced in the proton fragmentation process (direct photons) or from subsequent decays of directly produced particles with a mean travel distance less than 140 m, are considered. The main contribution of photons detected in the corresponding regions, are from the subsequent decays of π^0 and η.

Photon energy spectra are measured for events having no primary charged particles with p_T >100 MeV and $|\eta| < 2.5$. Primary charged particles are defined as charged particles with a mean lifetime greater than 300 ps, either directly produced in pp interactions or

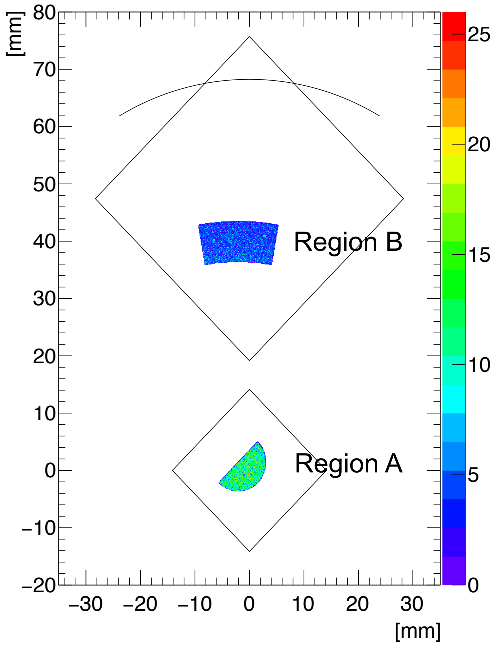

FIGURE 5.5: Hit map of selected events on the fiducial area of LHCf detector plane. The two diamond shapes illustrated the calorimeters of LHCf-Arm1 detector, the top arc represents the beam pipe projection to the detector. The beam center position that was defined as the projection of the beam direction at IP1 on the LHCf detector surface is located on (-2.04, 1.44). Region A and B were two fiducial area defined for the analysis of photon energy spectra, corresponding to $|\eta| > 10.94$ and $8.99 > |\eta| > 8.81$, respectively.

from subsequent decays of directly produced particles with mean lifetime smaller than 30 ps.

5.6.3 Event Reconstruction

The analysis procedure used to reconstruct photon events in the LHCf detector in the same as that described in Ref. [37]. The photon energy E_γ is reconstructed from the energy deposits in the LHCf calorimeters, as

$$E = J(S), \tag{5.1}$$

where, J is an empirical function determined by using the LHCf detector simulation, to covert the sum of the energy deposits S to the incident photon energy. The S is defined

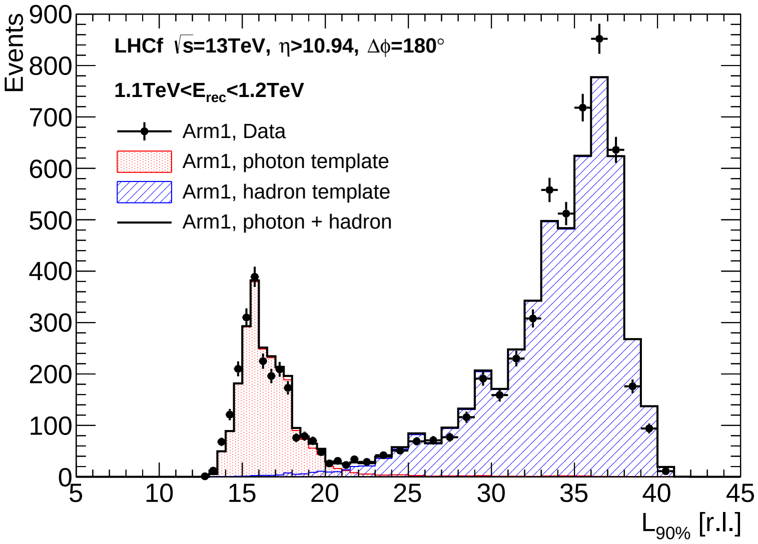

FIGURE 5.6: The $L_{90\%}$ distribution of the events selected in Region A and and 1.1 TeV $< E_{rec} <$ 1.2 TeV. The black points are the data, and the red and blue filled histogram are the template distributions of pure photons and pure hadrons, respectively. The black line represents the sum of photon and hadron templates.

as

$$S = \sum_{i=2}^{13} dE_i \, y_i(x,y) \, l_i(x,y), \tag{5.2}$$

where dE_i is the measured energy deposit at the i-th scintillation layer. In the energy reconstruction of photons, the energy deposits from 2nd to 13th layers were used. $y_i(x,y)$ is the correction factor for light-yield collection inefficiency. Due to the limitation of calorimeter size, the measured shower deposits produced by incident photons have to take into account of leakage effects. $l_i(x,y)$ is the leakage correction factor for the photon energy reconstruction.

The main observables measured by LHCf are photons and neutral hadrons (neutrons, etc.). Photon Identification (PID) is applied by using the estimator so called $L_{90\%}$, defined as the longitudinal shower depth in units of radiation length (X_0), at which the integral of the energy deposit measured by the sampling layers in the LHCf-Arm1 detector reaches 90% of the total energy deposit. The PID selection criterion is set to $L_{90\%} < L_{90\%,\mathrm{thr}}$ where $L_{90\%,\mathrm{thr}}$ is an energy-dependent value, corresponding to photon identification efficiency of 90%. Figure 5.6 shows the $L_{90\%}$ distribution of all events with reconstructed energy between 1.1 TeV and 1.2 TeV, located in the Region A. To estimate the efficiency and the purity of photons, the $L_{90\%}$ distribution was fitted by using the template distributions obtained from pure photon samples and pure hadron samples in the LHCf detector simulation.

The hit position of photon in the LHCf detector is reconstructed by searching for the maxima of the lateral distributions measured in the four position-sensitive layers. Multi-hit events, in which two or more x–y energy maxima are detected, are rejected in this analysis because of the poor performance of energy reconstruction in these events. The performance of photon energy and hit position reconstruction were studied in dedicated beam tests with electron beams [77].

Charged-particle tracks in the central pseudorapidity region ($|\eta| < 2.5$) are reconstructed using the ATLAS pixel and SCT detectors. A special track reconstruction algorithm is applied and charged particles with a transverse momentum down to $p_{\mathrm{T}} = 100$ MeV are measured. Each track is required to have at least one pixel hit, and the transverse impact parameter calculated with respect to the LHC beam line, $|d_0|$, smaller than 1.5 mm. More details about the performance of the track reconstruction in p-p collision data at $\sqrt{s} = 13$ TeV and simulation can be found in Ref. [78]. As shown in Fig. 5.3, the estimated track reconstruction efficiency for charged pions increases from about 20-60% at $p_{\mathrm{T}} = 100$ MeV (depending on η) to about 90% at $p_{\mathrm{T}} = 400$ MeV and becomes constant for $p_{\mathrm{T}} > 400$ MeV.

The necessary information to perform this analysis were stored in independent ROOT TTree files of ATLAS and LHCf. The LHCf files stored the reconstructed photon data, whereas, the reconstructed charged particles data was stored in the ATLAS files. Events in both files were ordered in such way that subsequent events are matched as described in Sec. 5.3. The analyses were performed event by event by reading the the data from both files.

5.6.4 Event selection

After the PID selection and the multi-hit rejection, selected events are required to have a reconstructed photon candidate, with a minimum energy of 200 GeV, inside the fiducial region A or B.

Next, selected events are classified based on the number of charged particle tracks, N_{track}, reconstructed in ATLAS inner detector. Figure 5.7 shows the comparison of the N_{track} distribution between the data and MC models, for events in which the LHCf-Arm1 detector reconstructed a photon (region A or B). The contribution of non-diffractive events around $N_{\mathrm{track}} = 0$ is less than 2% in all models. The ratio of $N_{\mathrm{track}} = 0$ events to the total number of events is 20% in the data, whereas the same ratio predicted by the MC models varies between 6% and 20% (depending on the model). Moreover, the contribution from double diffractive dissociation process to $N_{\mathrm{track}} = 0$ events is

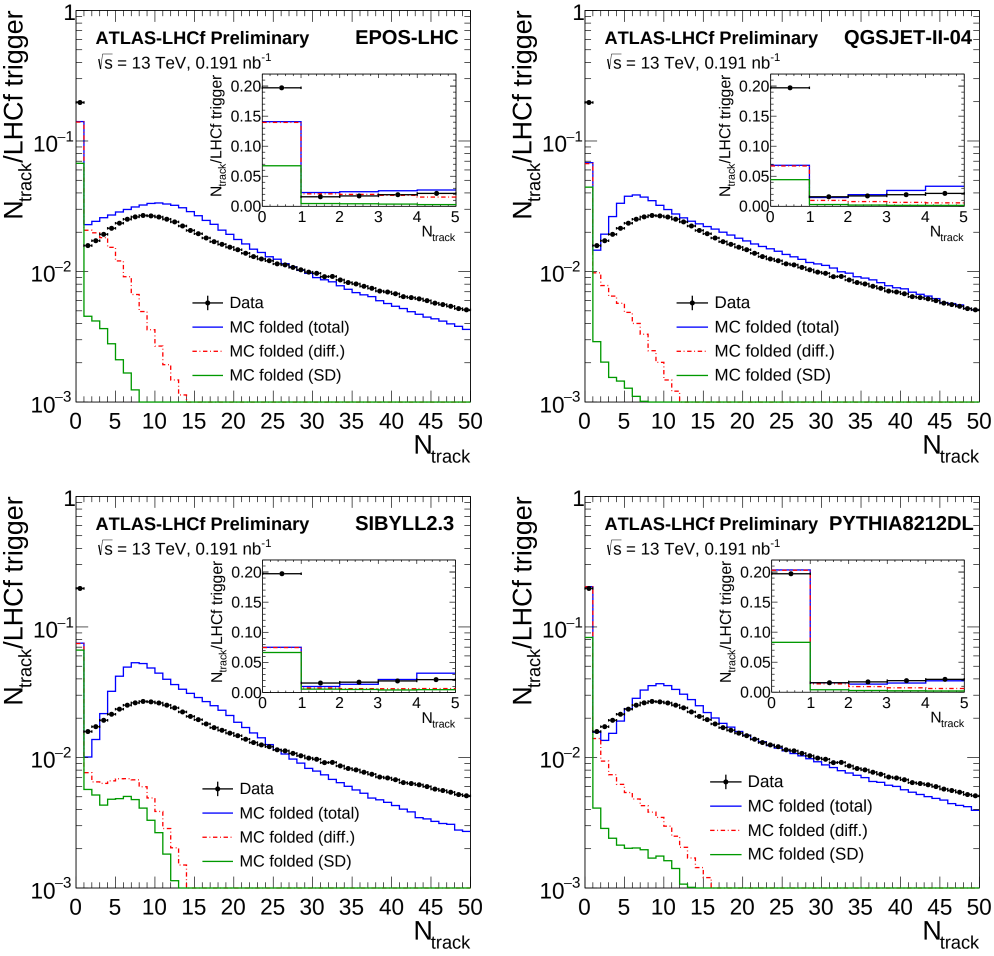

FIGURE 5.7: N_{track} distribution in data compared to several MC model predictions for events in which the LHCf-Arm1 detected a photon (in the region A or B) with $E_\gamma > 200$ GeV. All distributions are normalized to the total number of events. Black points indicate the measured spectrum and lines represent MC predictions, folded with the tracking efficiency of the ATLAS detector. Blue lines indicate the inclusive distributions, red lines the contribution from the proton diffractive dissociation events, and green lines the contribution from the single-diffractive events. The inserts show a zoom of the data and model predictions at small N_{track}. For these models only events with one particle-level photon ($E_\gamma > 200$ GeV and within the LHCf-Arm1 acceptance) are used. The LHCf simulation shows that most of the multi-photon events are rejected by the photon selection criteria and the fraction of multi-photon events remaining as a single-reconstructed photon relative to the total event yield is less than 2%.

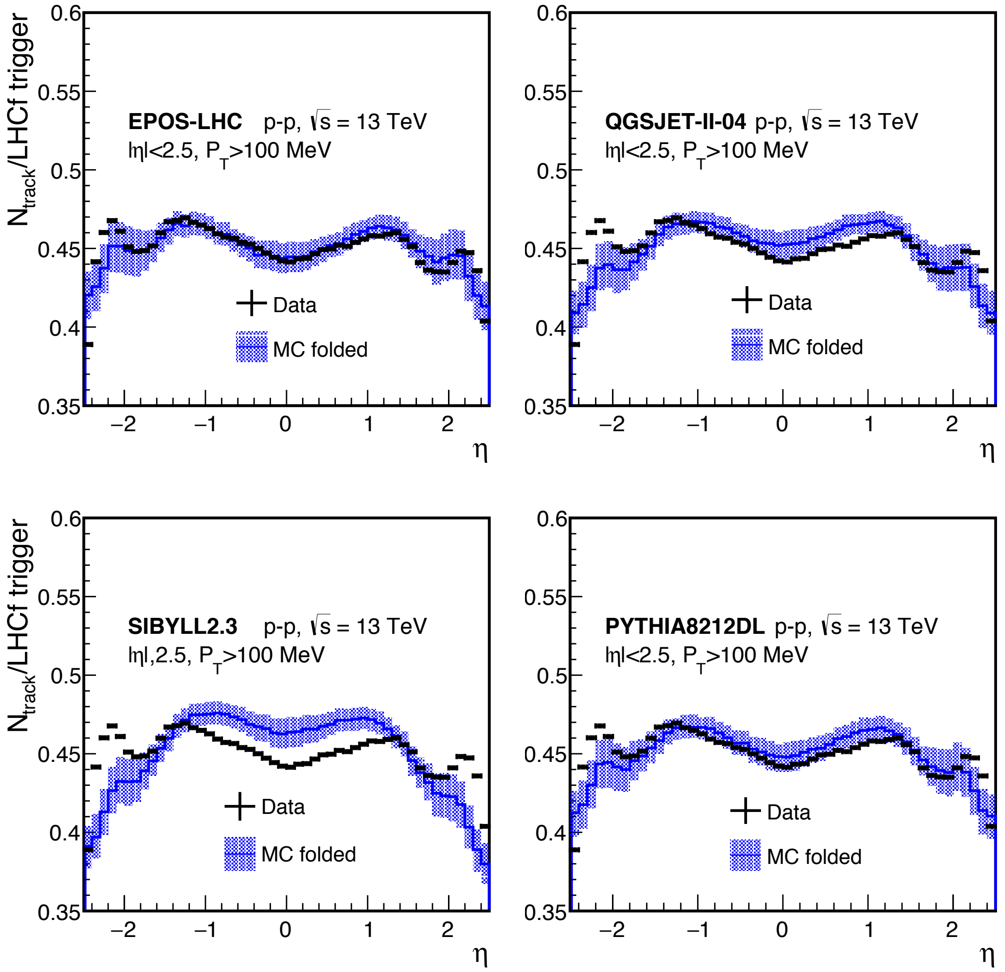

Figure 5.8: The track multiplicity of the triggered photon events by LHCf-Arm1 as a function of pseudorapidity. The blue colored lines show the distributions of the MC folded samples. The MC distributions were normalized by the area of the data. The hatched area show the systematic uncertainty estimated by varying the track detection efficiency discussed in Sec. 5.7.

relatively small for SIBYLL 2.3 and QGSJET-II-04 models, compared to EPOS-LHC and PYTHIA 8212DL.

According to the MC study described in Chapter 4, by selecting events with no charged particles with $p_{\mathrm{T}} > 100$ MeV and $|\eta| < 2.5$, non-diffractive events are rejected while keeping more than 50% detection efficiency of diffractive events and a purity of more than 99%. The purity is defined as the fraction of the selected events that are in the diffractive category based on MC true flags to all selected events. based on the predictions of QGSJET-II-04 model (Fig. 4.7). Additionally, the selection efficiency of single-diffractive (Fig. 4.14) and double-diffractive (Fig. 4.16) events based on ATLAS-veto are estimated as a function of the invariant mass of the diffractive system, M_X or M_Y. According to the QGSJET-II-04 predictions as shown in Fig. 4.14, the corresponding ATLAS-veto

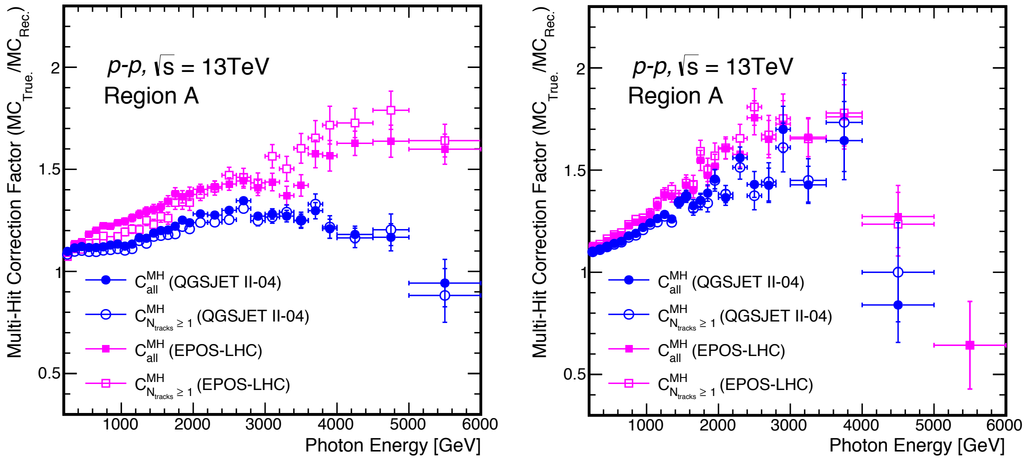

FIGURE 5.9: The multi-hit correction factor C^{MH} for both $N_{all}(E_i)$ and $N_{N_{tracks}\geq 1}(E_i)$. The correction factors calculated from the QGSJET-II-04 samples were used for the final results. The factors from EPOS-LHC were used for the estimation of the systematic uncertainty.

selection efficiency of SD events is more than 95% for $M_X < 20$ GeV and decreases to 10% for $M_X = 100$ GeV. Whereas, the same tendency of selection efficiency for the DD events was predicted based on PYTHIA 8212DL model as shown in Fig. 4.16. Therefore, mostly the low-mass diffractive events are expected to pass the $N_{\text{track}} = 0$ requirement.

Furthermore, event selection based on the charged particle tracks, N_{track}, with $p_{\text{T}} > 100$ MeV and $|\eta| < 2.5$ was widely used in this analysis. The track multiplicity distribution of the triggered photon events by LHCf-Arm1, as a function of pseudorapidity was checked as shown in Fig. 5.8. The black makers are the data, the blue lines correspond to the distributions of the MC samples with considering the track detection efficiency. To compare the shapes of these distributions between data and MC, the MC lines were normalized by the area of data. EPOS-LHC and PYTHIA 8212DL have good agreements with the data.

5.6.5 Analysis corrections

In this analysis, the reconstructed inclusive photon events, $N^{\text{all}}(E^i_\gamma)$, were classified into the events with at lest charged particle with $p_{\text{T}} > 100$ MeV and $|\eta| < 2.5$, $N_\gamma^{N_{\text{ch}}\geq 1}$ and the rest. The correction for detector effects is performed with a bin-by-bin correction procedure, based on MC simulated events, and is done separately for regions A and B. Such correction was applied to both $N^{\text{all}}(E^i_\gamma)$ and $N_\gamma^{N_{\text{ch}}\geq 1}$. The unfolded inclusive-photon rate in the i-th energy bin, $N^{\text{all}}_\gamma(E^i_\gamma)$, is obtained as

$$N^{\text{all}}_\gamma = C^{\text{all}}_\gamma \, N^{\text{all}} \left(1 - R_{\text{bkg1}}\right) , \tag{5.3}$$

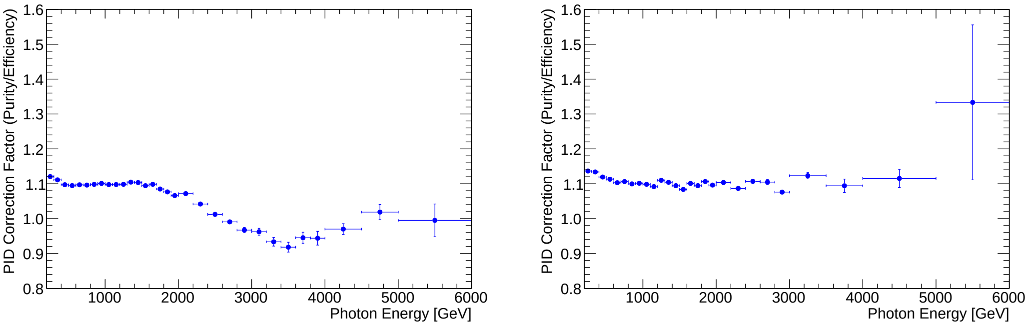

(a) $\eta > 10.94$ (b) $8.81 < \eta < 8.99$

FIGURE 5.10: The PID correction factor C^{PID} for both $N_{all}(E_i)$ and $N_{N_{tracks}\geq 1}(E_i)$. The correction factors calculated from the QGSJET-II-04 MC samples and the data.

where $C_{\gamma}^{\rm all}(E_{\gamma}^{i})$ are the correction factors related to the inclusive photon selection in LHCf, $N^{\rm all}(E_{\gamma}^{i})$ is the total number of selected events and $R_{\rm bkg1}$ is the small fraction of estimated background events. The correction factors $C_{\gamma}^{\rm all}(E_{\gamma}^{i})$ are consist of C^{MH} and C^{PID} which are relating to the muliti-hit event rejection and the PID selection. C^{MH} and C^{PID} as a function of photon energy are shown in Fig. 5.9 and Fig. 5.10, respectively. C^{PID} is used to correct the inefficiency of photon detection and the contamination of hadrons. The PID correction factors are between 0.9 and 1.1 in Region A , while around 1.1 in Region B. which were obtained from the template fitting of the $L_{90\%}$ distributions as shown in Fig. 5.6. C^{MH} was introduced to recover the photon flux reduced by the multi-hit rejection and to correct the contamination of multi-hit due to the mis-reconstruction as single-hit. Multi-hit correction factors are derived from a LHCf full detector simulation based on the predictions of QGSJET-II-04 and EPOS-LHC. In the energy region higher than 1.5 TeV in Region A and 1 TeV in Region B, photon pairs from high energy π^0 decays are dominant contribution to the multi-hit events. Due to the impact points of photon pairs on the LHCf calorimeters become closer when the π^0 energies increased, so that the fraction of multi-hit events becomes higher and higher. The factors obtained from QGSJET-II-04 were used for the correction, while the factors obtained from EPOS-LHC were used to estimate the systematic uncertainties.

By analogy, the unfolded photon spectrum for events with at least one charged particle with $p_{\rm T} > 100$ MeV and $|\eta| < 2.5$ is calculated as

$$N_{\gamma}^{N_{\rm ch}\geq 1} = C_{\rm track}\, C_{\gamma}^{N_{\rm track}\geq 1}\, N^{N_{\rm track}\geq 1}\, (1 - R_{\rm bkg2})\ , \tag{5.4}$$

where $C_{\rm track}(E_{\gamma}^{i})$ are the correction factors for the inefficiency of the track detection in ATLAS, and $C_{\gamma}^{N_{\rm track}\geq 1}(E_{\gamma}^{i})$, $N^{N_{\rm track}\geq 1}(E_{\gamma}^{i})$ and $R_{\rm bkg2}$ are defined in a similar way as parameters from Eq. 5.3, except the extra $N_{\rm track} \geq 1$ requirement. $C^{Track}(E_i)$ was

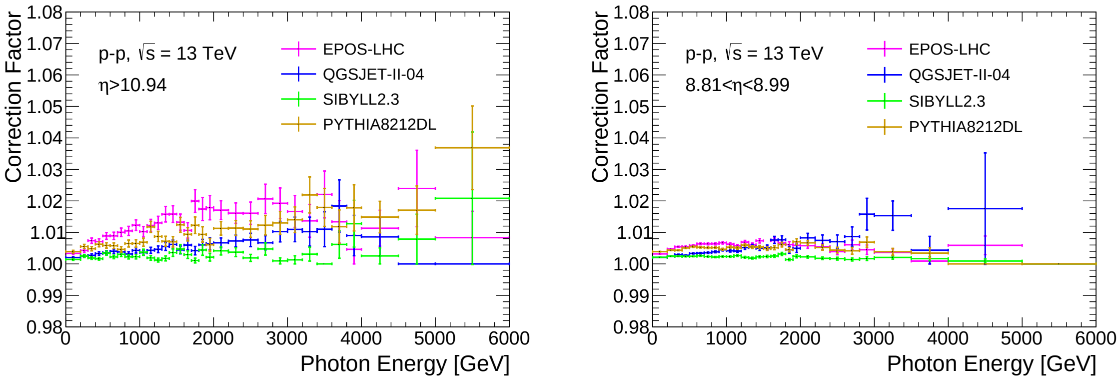

(a) $\eta > 10.94$

(b) $8.81 < \eta < 8.99$

FIGURE 5.11: The correction factor $C^{Track} = N_{N_{ch}\geq 1}(E_i)/N_{N_{tracks}\geq 1}(E_i)$. The values of EPOS-LHC were used as C^{Track}. The others were used for the estimation of the systematic uncertainty of C^{Track}.

obtained by a MC study based on the simulation samples with and without considering the track detection efficiency of ATLAS. Figure 5.11 shows the correction factors obtained from the four interaction models. The correction factor from EPOS-LHC was used in this analysis, because EPOS-LHC shows the best agreement of the η distribution with the data. $C^{Track}(E_i)$ was calculated as $C^{Track}(E_i) = N_{N_{ch}\geq 1}(E_i)/N_{N_{tracks}\geq 1}(E_i)$. The maximum deviation from EPOS-LHC was assigned to the systematic uncertainty of C^{Track}. $C_\gamma^{N_{\mathrm{track}}\geq 1}(E_\gamma^i)$ is consist of $C^{MH}_{N_{tracks}\geq 1}(E_i)$ and $C^{PID}_{N_{tracks}\geq 1}(E_i)$. Because the $C^{PID}_{N_{tracks}\geq 1}(E_i)$ has the similar values with the PID correction factor used in Eq. 5.3, so the same PID correction factor was applied to Eq. 5.4. $C^{MH}_{N_{tracks}\geq 1}(E_i)$ was obtained from the MC samples applied to the event selection $N_{tracks} \geq 1$ and they are only ±3% different from $C^{MH}_{all}(E_i)$ as shown in Fig. 5.9.

The photon energy spectrum corresponding to events with no charged particles in the fiducial region, $N_\gamma^{N_{\mathrm{ch}}=0}(E_\gamma^i)$, is obtained by subtracting the photon energy spectrum for events having at least one charged particle from the inclusive-photon spectrum:

$$N_\gamma^{N_{\mathrm{ch}}=0} = N_\gamma^{\mathrm{all}} - N_\gamma^{N_{\mathrm{ch}}\geq 1} \ . \tag{5.5}$$

The $C_{\mathrm{track}}(E_\gamma^i)$ factors are introduced to correct the photon energy spectra for events with $N_{\mathrm{ch}} \geq 1$ that fail to satisfy the detector-level $N_{\mathrm{track}} \geq 1$ requirement. The values of C_{track} are obtained from the ATLAS detector simulation and are typically between 1 and 1.05.

Once the $N_\gamma^{N_{\mathrm{ch}}=0}$ and N_γ^{all} distributions are obtained, the ratio $N_\gamma^{N_{\mathrm{ch}}=0}/N_\gamma^{\mathrm{all}}$ can be derived. Since several experimental uncertainties cancel. This allows for a more precise comparison to theoretical models.

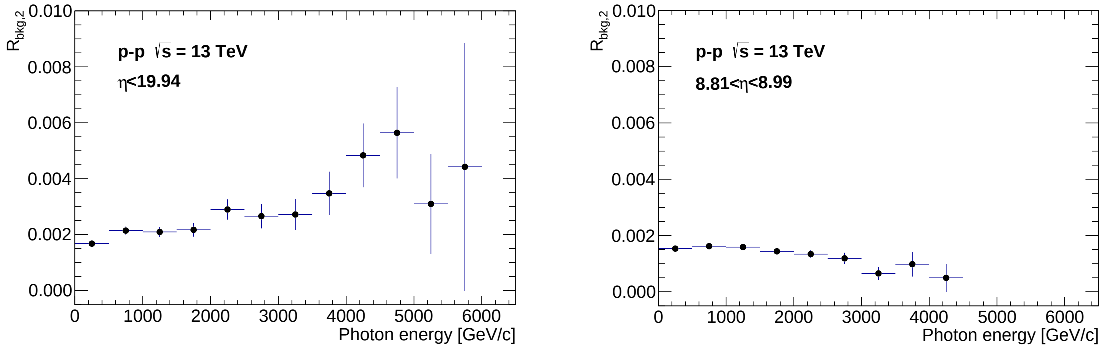

(a) $\eta > 10.94$ (b) $8.81 < \eta < 8.99$

FIGURE 5.12: The background ratio $R_{bkg,2}$ estimated as $R_{bkg,2} = \frac{N^{MC}_{N_{ch}=0\&N_{tracks}\geq 1}}{N^{MC}_{N_{tracks}\geq 1}}$ by using the ATLAS full detector simulation of non-elastic PYTHIA 8 samples.

5.6.6 Background estimation

The main background in the recorded data set is due to interactions between the proton beam and the residual gas in the beam pipe. This background is estimated by using events associated to non-colliding bunches at the ATLAS IP. The resulting estimates of the fraction of background, R_{bkg1}, in region A and B are 0.005 and 0.009, respectively, and they are found to be independent on the photon energy. Since no charged-particle tracks are detected in 90% of beam-gas background events, this background does not affect the $N_{\gamma}^{N_{\mathrm{ch}}\geq 1}$ spectrum from Eq. 5.4.

An additional source of background is pp collision events with $N_{\mathrm{ch}} = 0$ but having $N_{\mathrm{track}} \geq 1$. This background source can be split into three categories:

- Track migration from outside of the fiducial region (p_T >100 MeV and $|\eta| < 2.5$) of the measurement,
- Secondary tracks produced in interactions with dead material outside of the ATLAS tracker,
- Decay products of long-lived particles.

The contamination of $N_{\mathrm{ch}} = 0$ events due to $N_{\mathrm{track}} \geq 1$ events is estimated with the ATLAS detector simulation based on non-elastic PYTHIA 8 samples. Figure 5.12 shows the estimated background fraction, $R_{bkg,2} = \frac{N^{MC}_{N_{ch}=0\&N_{tracks}\geq 1}}{N^{MC}_{N_{tracks}\geq 1}}$, which is below 0.006.

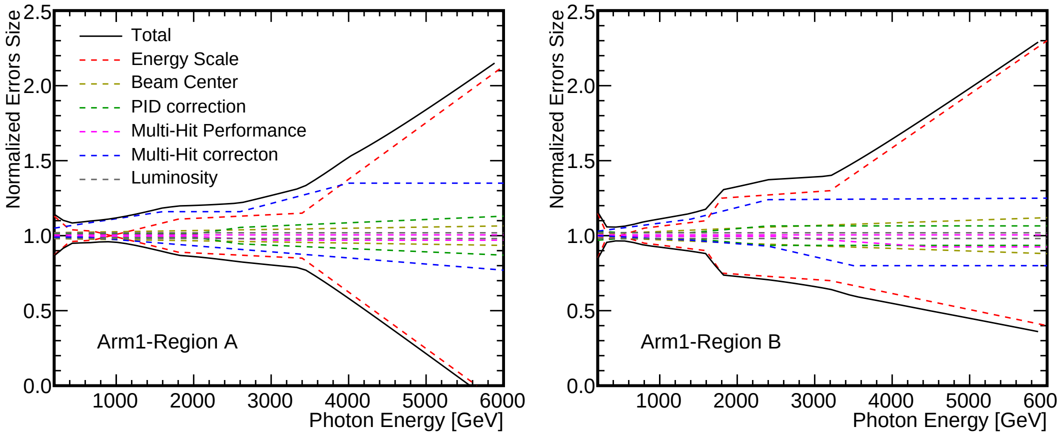

FIGURE 5.13: The summary of systematic uncertainties of LHCf photon analysis in p-p collisions at $\sqrt{s} = 13$ TeV. The left and right pads corresponding to the systematic uncertainties at RegionA and RegionB, respectively.

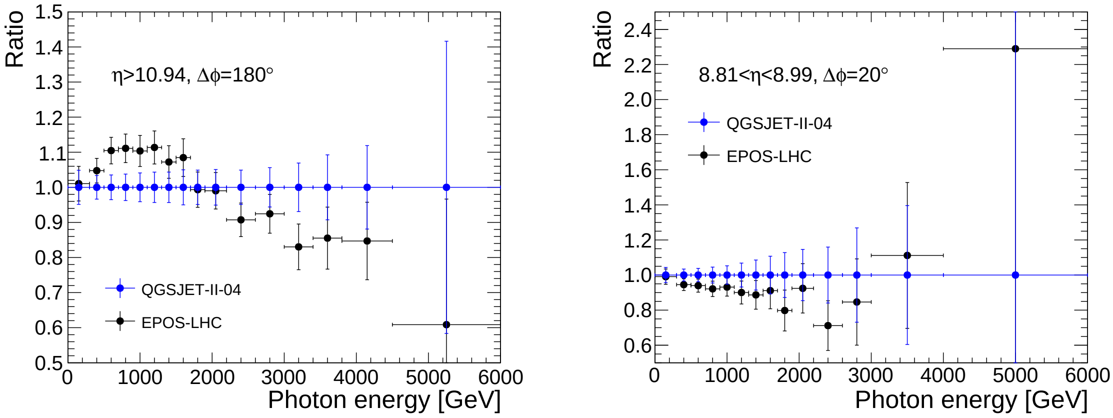

(a) $\eta > 10.94$

(b) $8.81 < \eta < 8.99$

FIGURE 5.14: The systematic uncertainty of the ratio measurement due to the multi-hit correction estimated as the double ratio $\frac{N'_{N_{ch}=0}/N'_{all} \text{ (with } C^{MH} \text{ from EPOS−LHC)}}{N'_{N_{ch}=0}/N'_{all} \text{ (with } C^{MH} \text{ from QGSJET−II−04)}}$.

5.7 Systematic uncertainties

Systematic uncertainties affecting the photon energy spectra can be categorized according to uncertainties due to the LHCf event reconstruction and correction (C_γ factors), the normalization factor, the ATLAS tracking efficiency modeling, the impact of fake tracks, as well as the C_{track} factor modeling effects. Details of these systematic uncertainties are discussed below:

- LHCf event reconstruction

  The estimation of the systematic uncertainties related to the reconstruction of the photon energy spectra follows the procedure described in Ref. [37]. Which were illustrated in Fig. 5.13, consist of the energy scale error, the beam center position, the PID performance, the multi-hit identification efficiency, the multi-hit correction and luminosity.

The photon energy scale is the dominant source of systematic uncertainty in the photon energy spectrum measurement. The photon energy scale uncertainty is 3.4%, which impacts the photon energy spectrum in region A (region B) by 15% (30%) at a photon energy of around 3 TeV. A significant number of multi-hit events is induced by photon pairs from high-energy π^0 decays. Therefore, the difference in the π^0 energy spectrum between the models induces a systematic model dependence on C^{MH}. A possible model dependence of the photon correction factors is estimated by comparing C^{MH} factors obtained using MC simulated samples based on QGSJET-II-04 and EPOS-LHC as shown in Fig. 5.9. Figure 5.13 shows the difference between these two models, it is taken as the systematic uncertainty.

Systematic uncertainties related to the photon reconstruction mostly cancel in the $N_{\gamma}^{N_{\mathrm{ch}}=0}/N_{\gamma}^{\mathrm{all}}$ ratio. However, the correction factors C_{all}^{MH} ($C_{\gamma}^{\mathrm{all}}$) and $C_{N_{tracks}\geq 1}^{MH}$ ($C_{\gamma}^{N_{\mathrm{track}}\geq 1}$) depend differently on the choice of the interaction model as shown in Fig. 5.9. This model uncertainty is also estimated by comparing predicted $N_{\gamma}^{N_{\mathrm{ch}}=0}/N_{\gamma}^{\mathrm{all}}$ ratios, based on EPOS-LHC and QGSJET-II-04 MC samples. Figure 5.14 shows the double ratio $\frac{N'_{N_{ch}=0}/N'_{all}\text{ (with } C^{MH}\text{ from EPOS}-\text{LHC)}}{N'_{N_{ch}=0}/N'_{all}\text{ (with } C^{MH}\text{ from QGSJET}-\text{II}-04\text{)}}$. This ratio measurement is the dominant source of the systematic uncertainties, as shown in Fig. 5.16, the relative uncertainties are 10% (20%) below 3 TeV and up to 40% (80%) for photons with energies above 4 TeV in region A (region B).

- Normalization factor

  The photon energy spectra are normalized to the expected number of inelastic collisions, which depends on both the integrated luminosity of the data sample and the value of the pp inelastic cross section at $\sqrt{s} = 13$ TeV. The integrated luminosity uncertainty of 1.9% [79, 80] is already taken into account in the inelastic cross section measurement. Therefore, the resulting uncertainty on the normalization factor is estimated to be 3.7% arising from the uncertainty on the measured inelastic cross section [70]. The normalization uncertainty cancels in the $N_{\gamma}^{N_{\mathrm{ch}}=0}/N_{\gamma}^{\mathrm{all}}$ ratio.

- ATLAS track reconstruction efficiency

  The uncertainty on the track reconstruction efficiency derives from imperfect knowledge of the passive material of the ATLAS detector. Corresponding uncertainty is estimated based on an extra simulation with an increased amount of detector material to evaluate the track reconstruction efficiency. Total uncertainties of the track reconstruction efficiency arises from the increased material are calculated as,

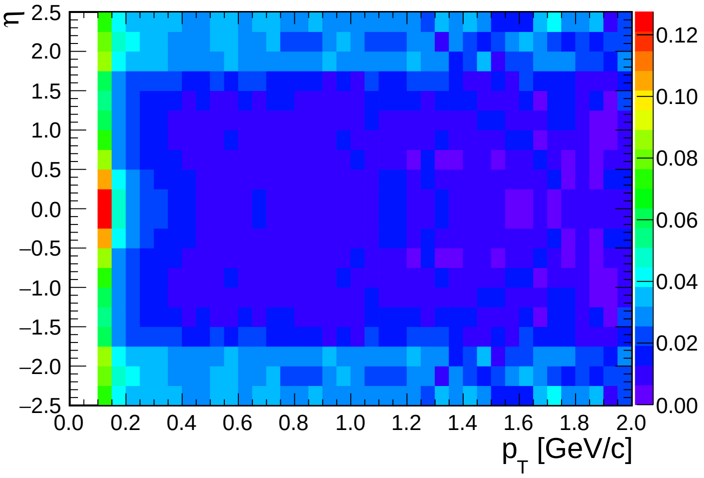

FIGURE 5.15: The estimated uncertainty of the track detection efficiency. The color shows the size of the uncertainty normalized by the values of efficiency.

linearly sum up the contributions of 5% additional material in the entire inner detector, 10% additional material in the innermost Insertable B layer (IBL) and 50% additional material in the pixel services region at $|\eta| > 1.5$. These material variations are motivated by dedicated studies of photon conversions, hadronic interactions, and track losses due to interactions with detector services [81]. The estimated uncertainty on the tracking efficiency is found to be between 2% and 12% as shown in Fig. 5.15. Such uncertainty on the tracking efficiency is assigned symmetrically to the upward and downward side.

The effect of model-dependence of the track reconstruction efficiency is studied by using four different event generators. Both the nominal tracking efficiency and the relative uncertainties of tracking efficiency were applied to the MC samples. According to the obtained photon spectra, the maximum deviation in the four event-generator samples was used as the systematic uncertainty of the spectrum. As the blue lines shown in the Fig. 5.16, the systematic uncertainty is estimated to be about 8% as the maximum deviation among the four samples.

- Fake tracks

  The impact of fake tracks on the final results is estimated by relaxing the track selection criteria. The requirement on the transverse impact parameter, $|d_0| < 1.5$ mm, is removed from the track selection, enhancing the contribution of fake tracks. A difference in the $N_\gamma^{N_{\mathrm{ch}}=0}$ spectrum between the nominal and d_0-relaxed track selection criteria is about 1%, which is taken as the systematic uncertainty.

  As a further cross-check, the analysis is repeated with an increased p_T threshold ($p_T > 400$ MeV) in the track selection. In the data, the number of events obtained with the p_T threshold of 400 MeV is about 2% smaller than of the 100 MeV

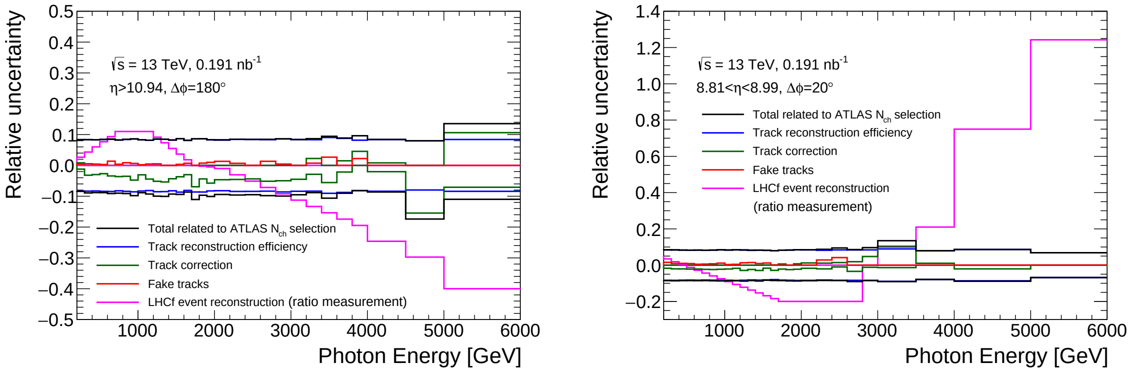

(a) $\eta > 10.94$ (b) $8.81 < \eta < 8.99$

FIGURE 5.16: Summary of systematic uncertainties related with ATLAS event selection. The uncertainties are assigned to the $N_\gamma^{N_{\mathrm{ch}}=0}$ spectra and to the $N_\gamma^{N_{\mathrm{ch}}=0}/N_\gamma^{\mathrm{all}}$ ratio. Additionally, the systematic uncertainty on the ratio related with LHCf photon selection is shown as a reference.

threshold. The differences of the spectra between two thresholds are between 1% and 10% depending on the photon energies and the models. Figure 5.17 shows the ratio $\frac{\mathrm{N\,with}\,p_T>100\mathrm{MeV}}{\mathrm{N\,with}\,p_T>400\mathrm{MeV}}$ as a function of the photon energy. The ratio of the data is located between ones of the MC folded samples. The differences between the data and the MC samples are caused by not only the fake tracks in the data but also the different p_T distributions. So the difference was not assigned as a systematic uncertainty.

- Track correction factor

  The systematic uncertainty on C_{track} is estimated by taking the maximum deviation between the values derived with the EPOS-LHC MC sample and the values predicted by other MC models. As shown in Fig. 5.16, the estimated uncertainty on the track correction factor is 5% and 3% for region A and B, respectively.

5.8 Results

The forward photon energy spectra measured by the LHCf-Arm1 detector are shown in Fig. 5.18, separately for region A ($\eta > 10.94$, $\Delta\phi < 180°$) and region B ($8.81 < \eta < 8.99$, $\Delta\phi < 20°$), and both for the N_{ch}-inclusive and $N_{\mathrm{ch}} = 0$ regions. In region A, the $N_\gamma^{N_{\mathrm{ch}}=0}$ photon energy spectrum observed in data is much harder than the inclusive-photon spectrum at the photon energies below 3 TeV, whereas the $N_\gamma^{N_{\mathrm{ch}}=0}$ and inclusive photon spectra have similar slope in region B.

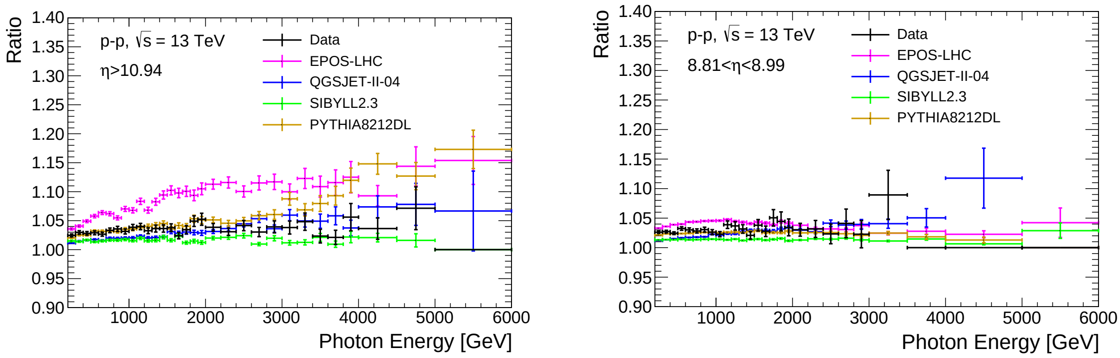

(a) $\eta > 10.94$ (b) $8.81 < \eta < 8.99$

FIGURE 5.17: The double ratio of changing the selection condition from P_T >100 MeV to P_T > 400 MeV, as the ratio $\frac{N_{\mathrm{N}_{\mathrm{tracks}=0}\ with\ p_T>100\ \mathrm{MeV}}}{N_{\mathrm{N}_{\mathrm{tracks}=0}\ with\ p_T>400\mathrm{MeV}}}$.

The results are also compared to several model predictions. Hereby, all MC predictions include an extra 10% uncertainty related to the contribution from photons produced in long-lived particle decays (with the mean lifetime above 33 ps), which is currently not taken into account in the calculation of model predictions. The PYTHIA 8212DL model shows good agreement with data up to $E_\gamma = 2$ TeV, in both the inclusive and $N_{\mathrm{ch}} =$ 0 regions. However, PYTHIA 8 predicts a significantly harder photon spectrum in the high-energy region. The EPOS-LHC model shows generally good agreement with data for all photon energies in the $N_{\mathrm{ch}} = 0$ region. QGSJET-II-04 shows good agreement with data at the photon energies above 3 TeV, whereas it predicts lower photon fluxes at the lower photon energies. SIBYLL 2.3 predict significantly lower photon fluxes in the N_{ch} = 0 region.

Figure 5.19 shows the ratio of the $N_\gamma^{N_{\mathrm{ch}}=0}$ photon spectrum to the inclusive-photon spectrum. In the region A, the ratio observed in data increases from 0.15 up to around 0.4 with increasing photon energy up to around 4 TeV and decreases to 0.15 again at the highest energy. This increase tendency is also observed for all model predictions, except SIBYLL 2.3. The PYTHIA 8 and SIBYLL 2.3 models predict higher and lower fraction of $N_{\mathrm{ch}} = 0$ events, respectively. This suggests that PYTHIA 8 (SIBYLL 2.3) predicts a too large (too small) contribution of low-mass diffractive events to the forward photon energy spectrum. In region B, the ratio in data is around 0.15 and is approximately constant over a wide range of photon energies. The SIBYLL 2.3 model predicts an average value of the ratio that is much lower than observed in data. QGSJET-II-04 predicts lower ratio at photon energies below 1.5 TeV. The EPOS-LHC and PYTHIA 8212DL generators show reasonable agreement with data.

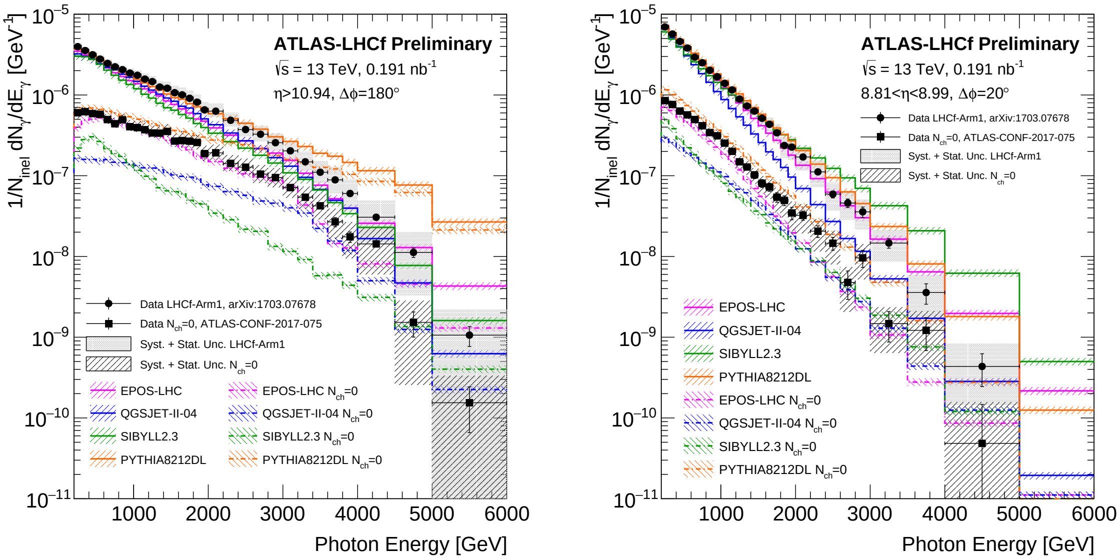

(a) $\eta > 10.94$ (b) $8.81 < \eta < 8.99$

FIGURE 5.18: Forward photon energy spectra measured by the LHCf-Arm1 detector in the regions A (left) and B (right). Filled circles show the inclusive-photon spectra measured in Ref. [37]. Filled squares indicate the spectra for $N_{\mathrm{ch}} = 0$ events, where no extra charged particles with $p_{\mathrm{T}} > 100$ MeV and $|\eta| < 2.5$ are present. Vertical bars represent statistical uncertainties of the data sample, while gray bands indicate the quadratic sum of statistical and systematic uncertainties. Colored lines indicate model predictions with (dashed lines) and without (solid lines) the $N_{\mathrm{ch}} = 0$ requirement. Hatched areas around the model lines indicate the 10% uncertainty related to the contribution from photons produced in long-lived particle decays, which is currently not taken into account in the calculation of model predictions.

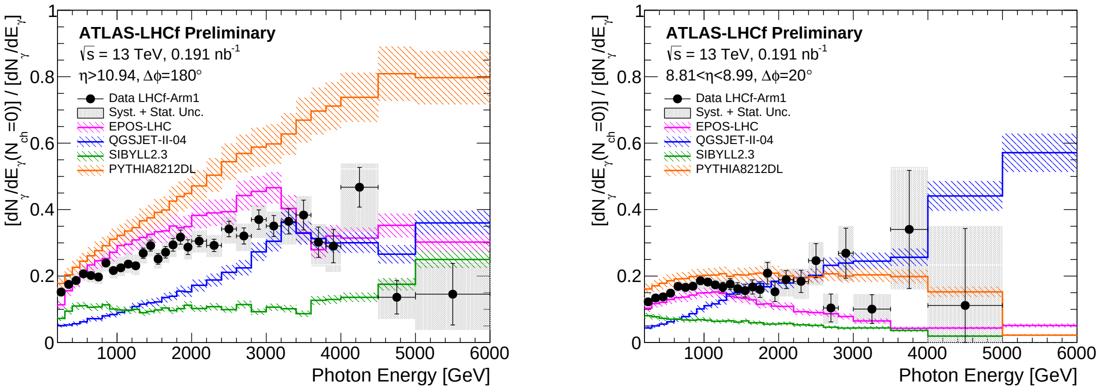

(a) $\eta > 10.94$ (b) $8.81 < \eta < 8.99$

FIGURE 5.19: Ratio of the photon energy spectrum with an extra $N_{\mathrm{ch}} = 0$ requirement to the inclusive-photon energy spectrum for regions A (left) and B (right). Vertical bars represent statistical uncertainties of the data sample, while gray bands indicate the quadratic sum of statistical and systematic uncertainties. Colored lines indicate model predictions. Hatched areas around the model lines indicate the 10% uncertainty related to the contribution from photons produced in long-lived particle decays, which is currently not taken into account in the calculation of model predictions.

5.9 Summary

This Chapter presents the first joint analyses of the ATLAS and LHCf collaborations, based on 0.191 nb^{-1} of pp collision data recorded at $\sqrt{s} = 13$ TeV. In order to study the contribution of low-mass diffractive processes to the forward photon production, the event selection relies on the veto of charged-particle tracks in the ATLAS inner tracker. The photon energy spectra are measured in two pseudorapidity ranges, $\eta > 10.94$ or $8.81 < \eta < 8.99$, for events with no extra charged particles having $p_{\mathrm{T}} > 100$ MeV and $|\eta| < 2.5$. The photon spectra for $N_{\mathrm{ch}} = 0$ events are compared to the inclusive photon spectra, to allow for a comparison of non-diffractive and diffractive particle production processes.

The ratio between the $N_{\gamma}^{N_{\mathrm{ch}}=0}$ and inclusive photon spectra increases from 0.15 to 0.4 with increasing photon energy up to 4 TeV at $\eta > 10.94$, whereas it is found to be relatively constant (around 0.15) at $8.81 < \eta < 8.99$. The results are compared to predictions based on several hadronic interaction models: EPOS-LHC, QGSJET-II-04, SYBILL 2.3, and PYTHIA 8.212DL. Predictions from EPOS-LHC generally show best agreement with data. At photon energies above 2 TeV, the PYTHIA 8 predicts significantly higher ratio than observed in data. This indicates that the large discrepancy between PYTHIA 8 and data in the high-energy photon region reported in Ref. [37] can be due to overestimation of the diffractive dissociation process in PYTHIA 8. The QGSJET-II-04 and SYBILL 2.3 models predict an average value of the ratio that is much lower than observed in data in both $\eta > 10.94$ and $8.81 < \eta < 8.99$ regions. This suggests that QGSJET-II-04 and SYBILL 2.3 predict a too small contribution of low-mass diffractive events to the forward photon energy spectrum.

Chapter 6

Discussion

6.1 low-mass diffraction

In Chapter 5, the very-forward photon production derived from low-mass diffractive processes was obtained for the first time based on the first ATLAS-LHCf joint analyses. According to the comparison between data and MC predictions on both spectra and ratio, SIBYLL2.3 predicts significantly lower photon fluxes in the $\mathrm{N_{ch}} = 0$ region and small fraction of $\mathrm{N_{ch}} = 0$ events. As introduced in Chapter 2, the pomeron flux (soft parton depends on the model) play an extremely important role in the implementation of diffractive dissociation in the models. The shape of pomeron flux exactly connected to the diffractive mass distribution implemented in the model at least in the framework of PYTHIA8 and SIBYLL2.3. As shown in Fig. 4.1, the SD cross-section as a function of $\log_{10}(\xi_X)$, which ξ_X is a function of diffractive mass, exhibits large discrepancies among models. Because the corresponding distribution of QGSJET-II-04 has been compared with the TOTEM and CMS data in several phase space intervals [30], the shape itself is believed be more close to the data. SIBYLL2.3 predict however too much different shape compare to the QGSJET-II-04, especially in the low-mass region. Therefore, we assumed that the pomeron flux implemented in SIBYLL2.3 is most plausible component which is responsible for the lower photon production from low-mass diffraction compared to the data.

To confirm our assumption, a modification of pomeron flux implemented in SIBYLL2.3 model has been applied. Since SIBYLL2.3 has just released a new version of SIBYLL2.3c without modification of pomeron flux, SIBYLL2.3c-Diff was tuned for its pomeron flux by using joint analyses results, but without the change of SD cross-section compared to SIBYLL2.3c [82]. SIBYLL2.3 and SIBYLL2.3c have no big difference in the photon

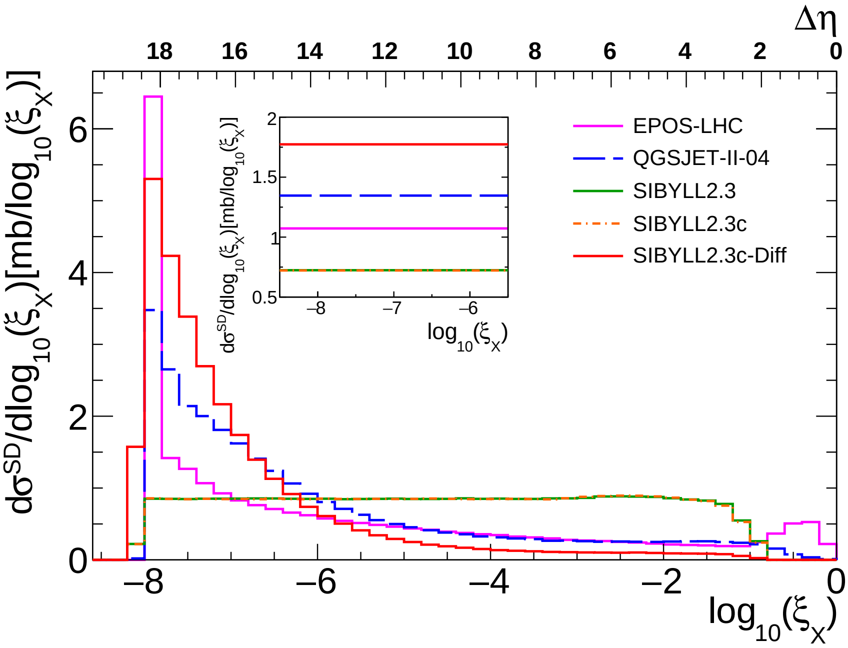

FIGURE 6.1: Diffractive mass distribution as a function of $\log_{10}\xi_x$ predicted by SIBYLL2.3, SIBYLL2.3c and SIBYLL2.3c-Diff compared with EPOS-LHC and QGSJET-II-04.

production from low-mass diffraction. Figure 6.1 shows the SD cross-section as a function of $\log_{10}(\xi_X)$. SIBYLL2.3c-Diff exhibits totally different shape of diffractive mass distribution compare to its previous models. In particular, it predicts the largest SD cross-section in the low-mass diffraction regions of -8.5 $< \log_{10}(\xi_X) <$ -5.5, increasing by 145.7% compared to SIBYLL2.3 (e.g. 4.336 mb → 10.654 mb). Then we preformed the same analyses as done in the joint analyses, and compared the predictions of three SIBYLL2.3 models to the data. Figure 6.2 shows the forward photon spectra in the regions of A and B both for the $N_{\rm ch}$-inclusive and $N_{\rm ch} = 0$ regions. By comparing with SIBYLL2.3 and SIBYLL2.3c, SIBYLL2.3c-Diff gives a good agreement with the data, which is comparable to EPOS-LHC on both region A and region B. Similarly, as the ratio results shown in Fig. 6.3, SIBYLL2.3c-Diff is dramatically improved and gives the best agreement with the data among the models, even better than EPOS-LHC. The forward neutron and π^0 productions in the two fiducial regions have also been investigated by comparing with the other several models. SIBYLL2.3c-Diff also gives the reasonable predictions. The detail comparisons are shown in Appendix A. Therefore, we can conclude at least as following in the framework of SIBYLL2.3,

- firstly, the shape of pomeron flux is an very important parameter for the implementation of diffractive dissociation,
- secondary, the cross-section of low-mass SD in the phase space of -8.5 $< \log_{10}(\xi_X) <$ -5.5 is close to 10.654 mb and 4.336 mb is too small.

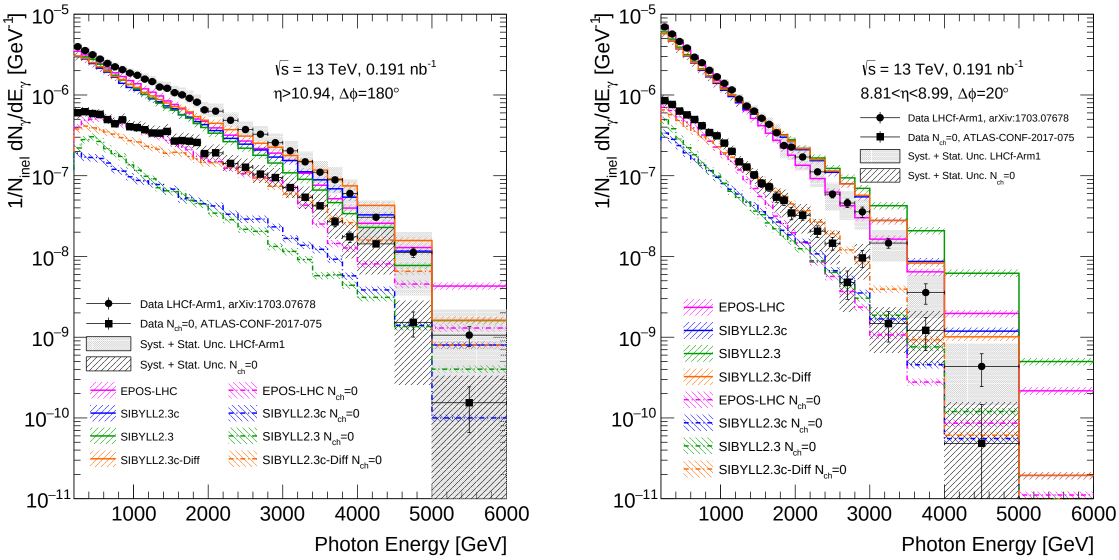

(a) $\eta > 10.94$ (b) $8.81 < \eta < 8.99$

FIGURE 6.2: Forward photon energy spectra measured by the LHCf-Arm1 detector in the regions A (left) and B (right). Filled circles show the inclusive-photon spectra measured in Ref. [37]. Filled squares indicate the spectra for $N_{\text{ch}} = 0$ events, where no extra charged particles with $p_{\text{T}} > 100$ MeV and $|\eta| < 2.5$ are present. Vertical bars represent statistical uncertainties of the data sample, while gray bands indicate the quadratic sum of statistical and systematic uncertainties. Colored lines indicate model predictions with (dashed lines) and without (solid lines) the $N_{\text{ch}} = 0$ requirement. Hatched areas around the model lines indicate the 10% uncertainty related to the contribution from photons produced in long-lived particle decays, which is currently not taken into account in the calculation of model predictions.

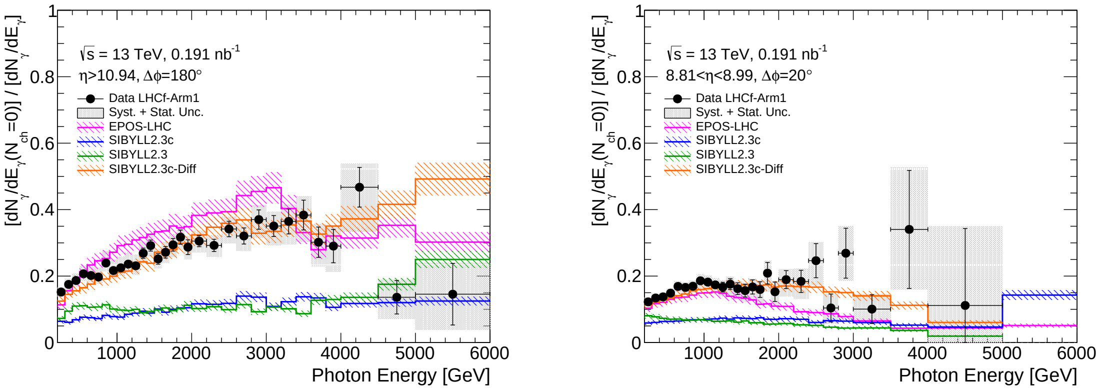

(a) $\eta > 10.94$ (b) $8.81 < \eta < 8.99$

FIGURE 6.3: Ratio of the photon energy spectrum with an extra $N_{\text{ch}} = 0$ requirement to the inclusive-photon energy spectrum for regions A (left) and B (right). Vertical bars represent statistical uncertainties of the data sample, while gray bands indicate the quadratic sum of statistical and systematic uncertainties. Colored lines indicate model predictions. Hatched areas around the model lines indicate the 10% uncertainty related to the contribution from photons produced in long-lived particle decays, which is currently not taken into account in the calculation of model predictions.

6.2 Impact to the determination of X_{max}

To investigate the impact of the measurement of very-forward photon production derived from low-mass diffractive processes to the determination of UHECR properties, we estimated the change in inelasticity due to the modification of SIBYLL2.3c then to the shift of X_{max}.

According to Equation 2.16, ξ_X can be expressed as

$$\xi_X \simeq e^{-\Delta\eta}. \tag{6.1}$$

As it is mentioned in [30], the inelasticity κ_{inela} can also be expressed by rapidity gap $\Delta\eta$,

$$\kappa_{inela} = 1 - E_{leading}/E_{primary} \simeq e^{-\Delta\eta}. \tag{6.2}$$

So that $\kappa_{inela} \simeq \xi_X$. An study about how inelasticity effects to the shifting of X_{max} was shown in Fig. 1.6, which was introduced in [19]. It suggests the mean value of X_{max} would decrease proportional to

$$-\Delta X_{max} \propto \lambda_e \ \ln\kappa_{inela} \propto \lambda_e \ \ln\xi_X \propto \lambda_e \ \log_{10}\xi_X/\ln 10, \tag{6.3}$$

where λ_e indicates an electromagnetic particle with energy E interacting after one splitting length $\lambda_e = \ln 2 \ X_0$. Here $X_0 \sim 37$ g/cm^2. The constraint on the diffractive mass distribution can directly effect the determination of X_{max}. The weighted average value of $\log_{10}\xi_X$ is -4.5336 in the original SIBYLL2.3 model. It changes to -6.919 in the model of SIBYLL2.3c-Diff based on the tuning of pomeron flux. If we assume the corresponding tuning only effects the diffractive processes (SD and DD), and inelasticity of non-diffractive processes is not changed, the shift of X_{max} is

$$\Delta X_{max} \propto \frac{\lambda_e \ (\sigma_{SD} + \sigma_{DD}) \ (\Delta\log_{10}\xi_X)}{\sigma_{inela} \ \ln 10} = 5.16 \ [\text{g/cm}^2]. \tag{6.4}$$

Here $\Delta\log_{10}\xi_X$ = -4.5336 - (-6.919) = 2.3854, and σ_{SD} = 12.17 mb, σ_{DD} = 3.35 mb. As shown in Fig. 1.4, uncertainties of mass composition predictions among the models for proton and iron are approximately 20 g/cm^2 and 15 g/cm^2, respectively. Therefore, shift of X_{max} by 5.16 g/cm^2 corresponds about 25% (33%) effect to the determination of proton (iron) primaries of UHECRs. In addition, corresponding calculations of the shift of X_{max} has been confirmed by an air shower simulation. The author of SIBYLL2.3 did a simulation to evaluate the performance of SIBYLL2.3c-Diff model. Figure 6.4 shows the comparisons of X_{max} predicted by several models, as well as the comparisons among data and models. According to the simulations, it shifts up X_{max} by approximately 5 g/cm^2 by comparing SIBYLL2.3c-diff with SIBYLL2.3c at 10^{17} eV (corresponding to

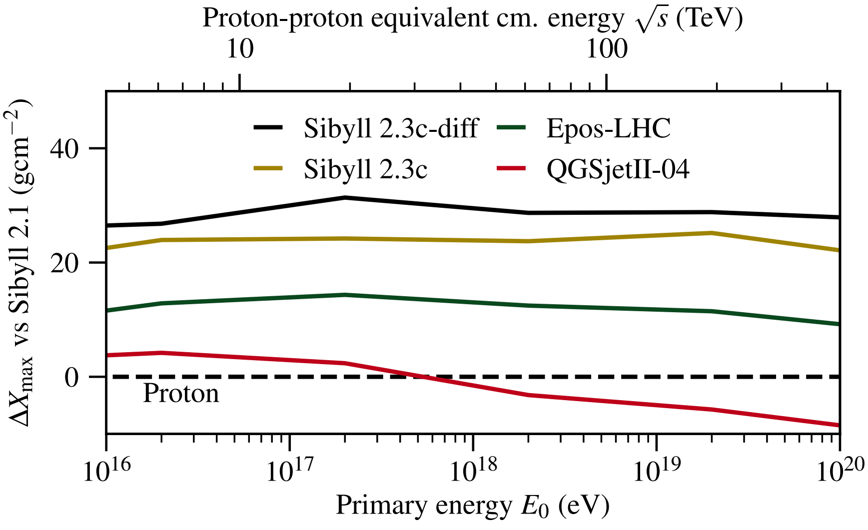

(a) Models vs. SIBYLL2.1

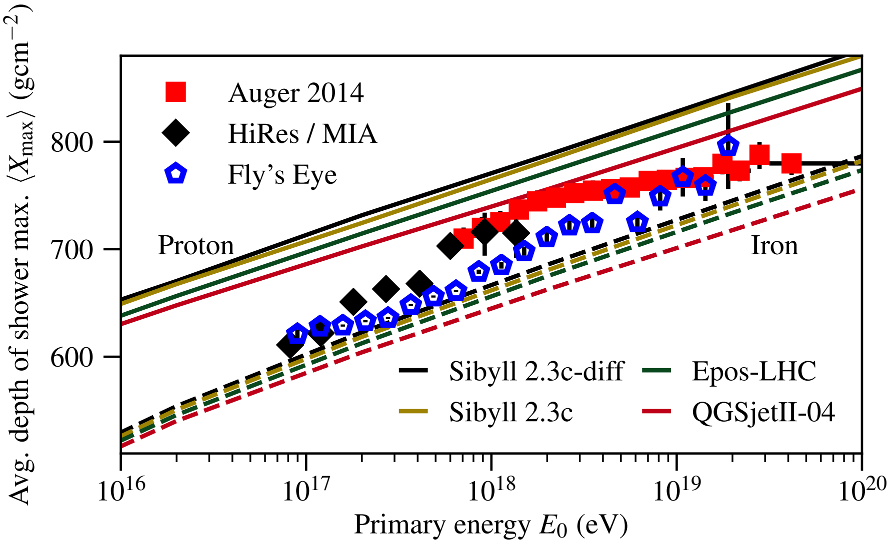

(b) Models vs. data

FIGURE 6.4: X_{max} as a function of energy. (a) indicates the ratio of X_{max} predicted by several models to predicted by SIBYLL2.1. SIBYLL2.3c-diff shift up X_{max} by approximately 5 g/cm^2 at 10^{17} eV compare to SIBYLL2.3c. (b) shows the X_{max} predicted by models and compared with experimental data [82].

$\sqrt{s} = 13$ TeV) [82]. Therefore, it is consistent with the calculation we have done above. Interpretation of experimental data based on the SIBYLL2.3c-Diff model will shift to heavier nuclei comparing to the original SIBYLL2.3c model. Accordingly, it will strongly disfavor the scenario of proton as primary UHECRs.

6.3 Future prospects for solving muon excess problem by joint analysis

Recently, one of most hottest topic in the cosmic-ray observations is the "muon excess" issue as introduced in Chapter 1. Pierre Auger Observatory reported the number of muons at the grand level is considerably larger than that of the expectation of air shower simulations based on the hadronic interaction models [16]. It directly connected to the determination of muon production depth, which is also an estimater of the UHECRs composition. The "muon excess" problem points out that the current hadronic interaction models are still poor constrained on the aspect of muon production, even in the post-LHC models, such as EPOS-LHC, QGSJET-II-04 and SYBILL 2.3.

Three observables measured based on ATLAS-LHCf joint analyses are expected to solving the "muon excess" issue:

- Measurements of the diffractive contribution to the forward neutron spectra in p–p collisions at $\sqrt{s} = 13$ TeV
- Total π^+p cross sections extracted from the leading non-diffractive neutron spectra
- The inclusive production cross sections of charged particles in the π^+p collisions

① **Forward diffractive neutron spectra**

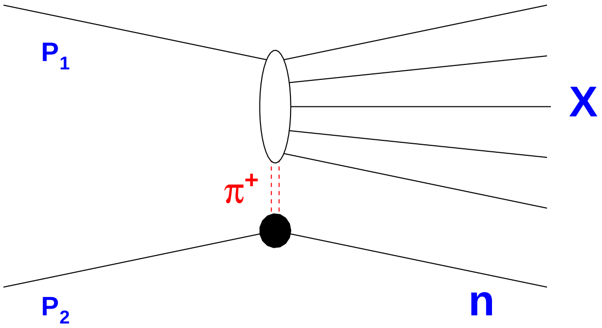

FIGURE 6.5: Feynman diagram of one-pion-exchange.

Although air shower development is a complex process, the simple cascade models can provide some insights about how air shower observables are related to the hadronic interaction physics on a microscopic level. There can be two components from the air showers be categorised into hadronic and electromagnetic parts. As introduced in subsection 1.2 in Chapter 1, hadronic components are related to the muon production through the interactions, baryons $\rightarrow$ hadronic shower $\rightarrow \pi^{\pm} \rightarrow \mu^{\pm} + \nu_{\mu}(\overline{\nu}_{\mu})$. Increase leading (anti) baryon production leads more energy provided to hadronic sub-showers, resulting in more hadron generations, and finally more muons. Discrepancies of the forward neutron (baryon) spectra predicted by several models shown in Fig. 4.3 are expected to indicate direct connection of that to the "muon excess" issue. The different dominant contributions from diffraction and non-diffraction are the sources of the discrepancies according to Fig. 4.3. The ATLAS-LHCf joint analyses can provide the first insight of dominant processes in the forward neutron production, and improve the models on the aspects of diffractive and non-diffractive differential cross sections.

② Total $\pi^{+}p$ cross section & inclusive charged particle production in $\pi^{+}p$ collisions

Air shower development is a process together with a large number of $\pi^{\pm}$-air interactions. Total $\pi^{+}p$ cross section directly impacts to the muon production depth then connects to the muon number. Meanwhile, Inclusive production cross sections of charged particles in $\pi^{+}p$ collisions are also the important parameters for the muon production. At present results of direct measurements of the $\pi^{+}p$ cross sections are known only up to $\sqrt{s} = 25$ GeV [83]. Various indirect methods for extraction of the $\pi^{+}p$ cross section were proposed by using the LHCf forward neutron data [71, 72]. All these approaches are based on the assumption of that one can isolate the pion-exchange (non-diffraction) contribution from the p–p collisions as illustrated in Fig. 6.5 ($p+p \rightarrow n+(\pi^{+*}+p) \rightarrow n+X$). However, the diffractive processes ((a) and (b) in Fig. 2.1) give a large contribution to the inclusive forward neutron spectra, and such contribution contaminate the extraction of the $\pi^{+}p$ cross section. Therefore, the neutron spectra derived from the non-diffractive processes classified based on the ATLAS-LHCf joint analyses can be used as a pure data sample to extract the total $\pi^{+}p$ cross section. Corresponding joint analyses results can be used to extract the $\pi^{+}p$ cross section at 4 TeV $< \sqrt{s_{\pi p}} <$ 6.5 TeV. On the other hand, ATLAS can measured the inclusive production cross sections of charged particles in the $\pi^{+}p$ collisions by using the LHCf forward neutron tagged events. Thus, the ATLAS-LHCf apparatus would be a powerful tool to utilize the LHC as a pure $\pi^{+}p$ collider.

The LHCf experiment has two independent detectors, called Arm1 and Arm2, installed at ±140 m from the interaction point 1 (ATLAS IP) of the LHC. The first ATLAS-LHCf joint analyses carried out based on the Arm1 photon data and the ATLAS data. It will be a more powerful data if using double arms data in future analyses of low-mass diffractive neutron production. Owing to the different shapes of Arm1 and Arm2 calorimeters, the double arm data can not only enhancing the statistics in the same phase space but also complementing the gaps of phase space of the other detector. According to the coincidence analysis of the double arm data, it can classify the forward diffractive spectra into more specific diffraction types; single diffraction and double diffraction which are illustrated in Fig. 2.1. Until now, no experiment is capable of providing the unique data at high energies which is especially sensitive to the ”muon excess” issue, except the ATLAS-LHCf joint analyses.

Chapter 7

Conclusions

Exploration of the origin of UHECRs is the remaining task of astroparticle physics. Two plausible classes of astrophysical accelerators have been considered as the candidate sources of extragalactic UHECRs: active galactic nuclei (AGNs) and gamma-ray bursts (GRBs). In order to solve the UHECR origin puzzle, it is necessary to perform precise measurements of the energy and mass composition of cosmic-rays up to the GZK cutoff region. The corresponding properties of UHECRs are obtained only from interpretation of the measurement data of extensive air showers, and thus depend strongly on the predictions of the air shower development based on hadronic interaction models. LHCf is a unique experiment dedicated to providing the calibration data in the very forward region of the collisions, to improve the understanding of hadronic interactions.

According to the published LHCf results based on the forward photon, π^0 and neutron data at different energies, no model can predict the LHCf data perfectly. Thus, we performed an analysis to classify the LHCf observables into more specific collision processes; diffraction and non-diffraction. In particular, the diffractive processes are expected to contribute approximately 25-30% of the total inelastic cross section at the LHC energies. Due to the difficultly of detection of diffractive processes, there are still poor constraints on the aspect of diffraction in the models, especially the low-mass diffraction. It is known that the low-mass diffraction has large impacts to the "muon excess" issue. In June 2015 LHCf had succeeded in data taking with ATLAS in *p*-*p* collisions at $\sqrt{s} = 13$ TeV; joint data analyses with ATLAS enable LHCf to classify the detected events into diffractive or non-diffractive collisions.

We studied the non-diffractive and diffractive contributions to very forward particle production at $\eta > 10.94$ and $8.81 < \eta < 8.89$ based on the MC predictions in *p*–*p* collisions at $\sqrt{s} = 13$ TeV. For the forward photon and π^0 energy spectra, PYTHIA8212DL predicted the largest diffractive contributions at high energies. In the cases of neutron differential cross sections at high energies, the results of EPOS-LHC and PYTHIA8212DL were dominated by diffraction at $|\eta| > 10.94$, while those of QGSJET-II-04 and SIYBLL2.3 were dominated by non-diffraction.

The methodology of identification of diffraction, based on the rapidity gap technique, was investigated. We studied the performance of an effective selection criterion for diffractive events, *there are no charged particles ($N_{track} = 0$) in the kinematic range $|\eta| < 2.5$ and $p_T > 100$ MeV*. Such a selection has ≈100% purity, independent of particle type, energy, and interaction model whereas selection efficiency increases from ∼30% to 70% with increasing energy. The surviving events from central-veto selection are mostly low-mass diffraction events in the phase space of $\log_{10}(\xi_x) < -5.5$. This indicates that the ATLAS-LHCf joint analyses can extract the low-mass diffraction with high purity. It would be the first direct measurement which is able to access such a low mass range at LHC energies. Hereby, the "muon excess" problem is considered to be connected to the poorly constrained implementation of low-mass diffraction in the models. The results of ATLAS-LHCf joint analyses are capable of both constraining the differential cross sections ($d\sigma/dE$, $d\sigma/d\eta$) of low-mass diffraction and helping to identify the inherent problems in the models corresponding to low-mass diffraction.

We accomplished the first joint analyses of the ATLAS and LHCf collaborations, based on 0.191 nb^{-1} of p–p collision data recorded at $\sqrt{s} = 13$ TeV. Joint analyses were performed following the corresponding methodology as described in Chapter 4. In order to study the contribution of low-mass diffractive processes to the forward photon production, the event was classified based on the veto of charged-particle tracks in the ATLAS inner tracker. The photon energy spectra were measured in two pseudorapidity ranges, $\eta > 10.94$ or $8.81 < \eta < 8.99$, with a selection of the events with no extra charged particles having $p_{\mathrm{T}} > 100$ MeV and $|\eta| < 2.5$. The photon spectra for $N_{\mathrm{ch}} = 0$ events were compared to the inclusive photon spectra, meanwhile, two classes of data were compared to their respective model predictions.

The ratio between the $N_{\gamma}^{N_{\mathrm{ch}}=0}$ and inclusive photon spectra increases from 0.15 to 0.4 with increasing photon energy up to 4 TeV at $\eta > 10.94$, whereas it was found to be relatively constant (around 0.15) at $8.81 < \eta < 8.99$. The results were compared to the predictions based on several hadronic interaction models: EPOS-LHC, QGSJET-II-04, SYBILL 2.3, and PYTHIA 8212DL. Predictions from EPOS-LHC generally show the best agreement with the data. At the photon energies above 2 TeV, PYTHIA 8 predicts a significantly higher ratio than the one observed in the data. This indicates that the large discrepancy between PYTHIA 8 and data in the high-energy photon region reported in Ref. [37] can be due to overestimation of the diffractive dissociation process in PYTHIA 8. The QGSJET-II-04 and SYBILL 2.3 models predict an average value of the ratio that is much lower than observed in data in both the $\eta > 10.94$ and $8.81 < \eta < 8.99$ regions. This suggests that QGSJET-II-04 and SYBILL 2.3 predict too small a contribution of low-mass diffractive events to the forward photon energy spectrum.

The common experiment between ATLAS and LHCf has succeeded. The ATLAS-LHCf joint analyses provided the world's first high-energy data to describe the performance of diffractive dissociation in the very forward region of the LHC collisions. Joint analysis results are helpful in specifying the problems in the air-shower simulation models. For instance, the SIBYLL2.3 model has already improved the accuracy of predictions of forward photon production when tuned using joint analysis results. It is confirmed that the pomeron flux is a dominant parameter for the implementation of diffractive dissociation, according to the tuning of the SIBYLL2.3c model (SIBYLL2.3c-Diff). Precise hadronic interaction models are desired, to contribute to improving the accuracy of the prediction of air showers. The tuning of low-mass diffraction in SIBYLL2.3c has a strong correlation with inelasticity. According to the presented calculations, corresponding tuning in SIBYLL2.3 shifted up X_{max} by 5.16 g/cm^2, resulting in the interpretation of Auger data shifted to heavier nuclei (disfavoring proton sources). These results have been confirmed by using air shower simulations. In the future, measurements of forward neutron production, derived from low-mass diffraction by the ATLAS-LHCf joint analysis, are expected to solve the "muon excess" problem in air shower observations. Finally, the origin of UHECRs is expected to be approached according to the results presented in this thesis.

Appendix A

SIBYLL2.3c with tuned diffractive mass distribution

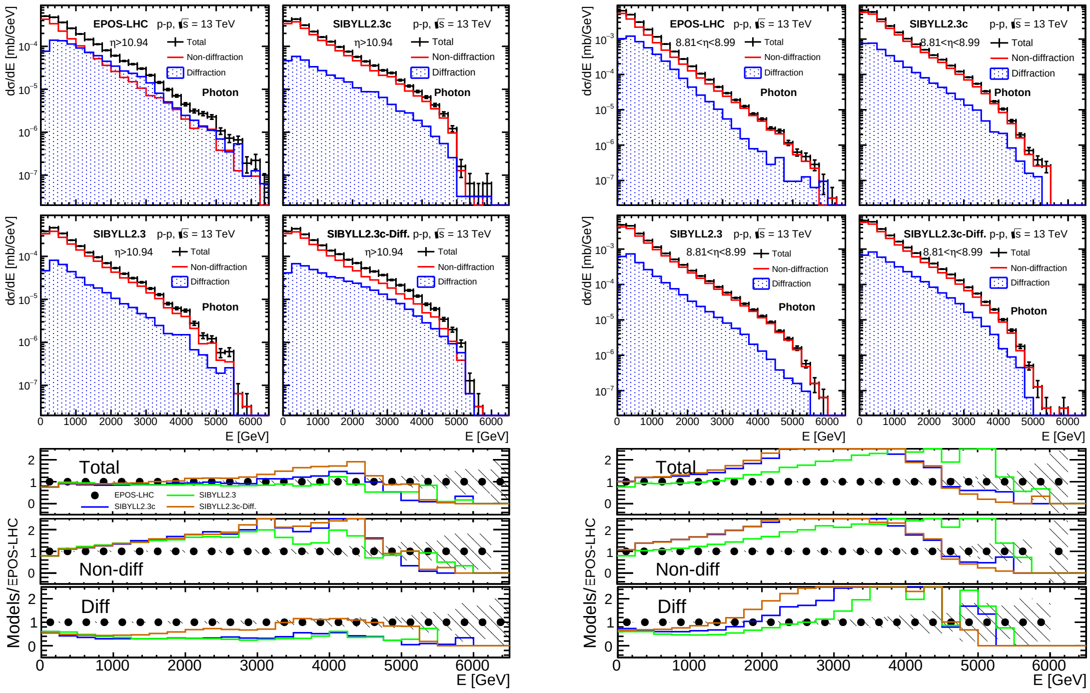

Figure A.1: Photon spectra at $\eta > 10.94$ (left) and $8.81 < \eta < 8.99$ (right) (top four panels in each set). These are generated by EPOS-LHC, SIBYLL2.3c, SIBYLL 2.3, and SIBYLL2.3c-Diff., respectively. The total neutron spectra (black) were classified by non-diffraction (red) and diffraction (blue) according to MC true flags. The bottom three plots show the ratios of the spectrum of EPOS-LHC (black markers), SIBYLL2.3c (blue lines), SIBYLL 2.3 (green lines), and SIBYLL2.3c-Diff. (orange lines) to the spectrum of EPOS-LHC. The top, middle, and bottom plots correspond to total, non-diffraction, and diffraction, respectively.

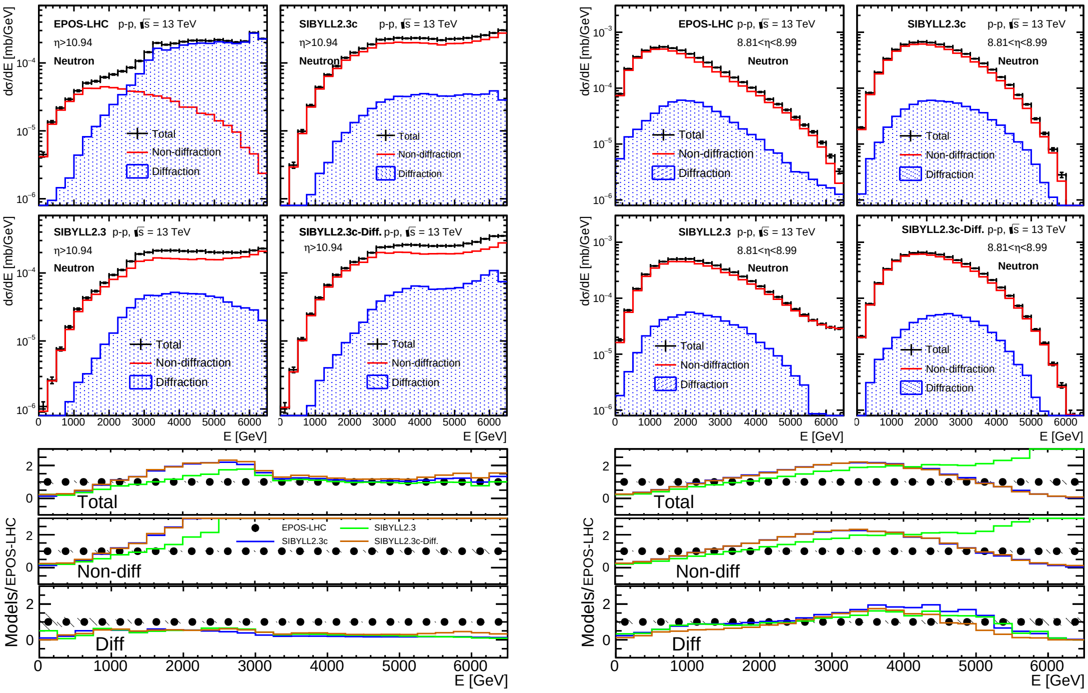

FIGURE A.2: Neutron spectra at $\eta > 10.94$ (left) and $8.81 < \eta < 8.99$ (right) (top four panels in each set). These are generated by EPOS-LHC, SIBYLL2.3c, SIBYLL 2.3, and SIBYLL2.3c-Diff., respectively. The total neutron spectra (black) were classified by non-diffraction (red) and diffraction (blue) according to MC true flags. The bottom three plots show the ratios of the spectrum of EPOS-LHC (black markers), SIBYLL2.3c (blue lines), SIBYLL 2.3 (green lines), and SIBYLL2.3c-Diff. (orange lines) to the spectrum of EPOS-LHC. The top, middle, and bottom plots correspond to total, non-diffraction, and diffraction, respectively.

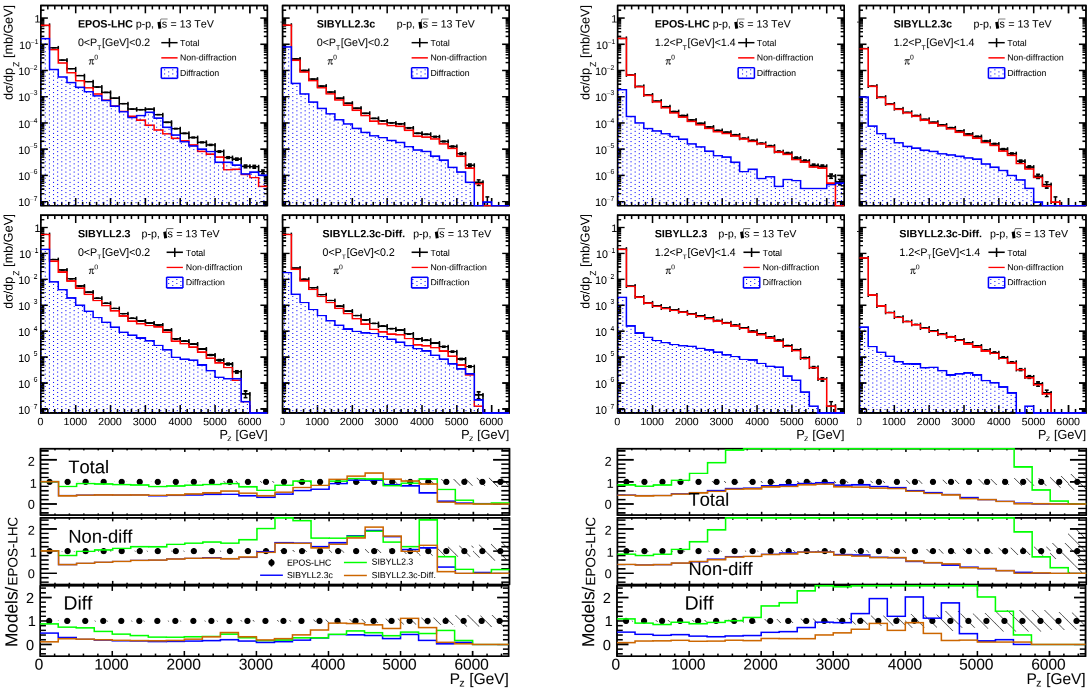

FIGURE A.3: π^0 spectra at $\eta > 10.94$ (left) and $8.81 < \eta < 8.99$ (right) (top four panels in each set). These are generated by EPOS-LHC, SIBYLL2.3c, SIBYLL 2.3, and SIBYLL2.3c-Diff., respectively. The total neutron spectra (black) were classified by non-diffraction (red) and diffraction (blue) according to MC true flags. The bottom three plots show the ratios of the spectrum of EPOS-LHC (black markers), SIBYLL2.3c (blue lines), SIBYLL 2.3 (green lines), and SIBYLL2.3c-Diff. (orange lines) to the spectrum of EPOS-LHC. The top, middle, and bottom plots correspond to total, non-diffraction, and diffraction, respectively.

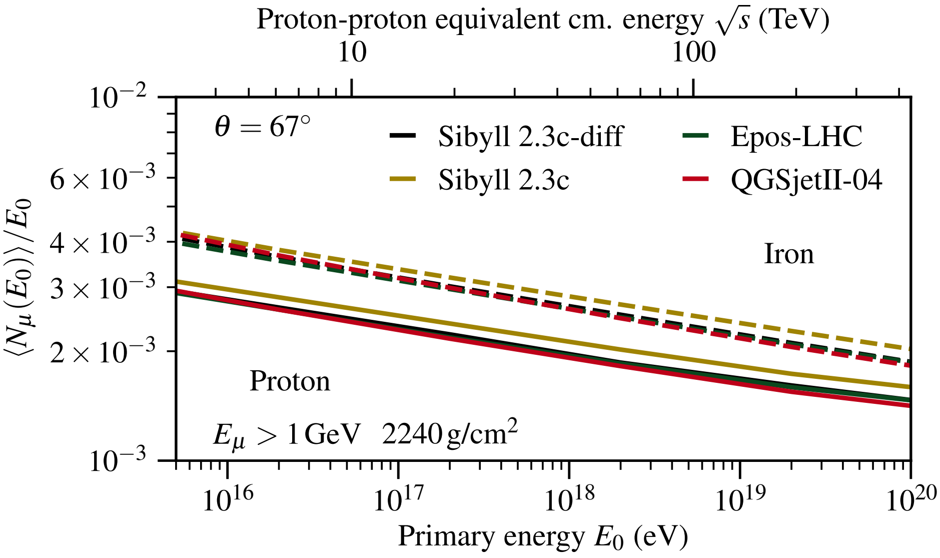

(a) Model comparison

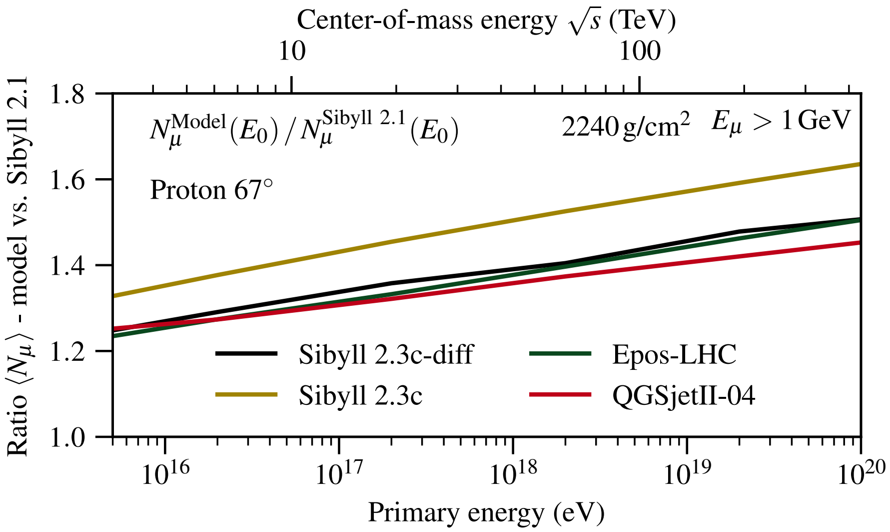

(b) Models vs. SIBYLL2.1

Figure A.4: Predictions of muon number as a function of energy. (a) shows the muon number predicted by models of SIBYLL2.3c-Diff, SIBYLL2.3c, EPOS-LHC and QGSJET-II-04. (b) indicates the ratio of X_{max} predicted by several models to predicted by SIBYLL2.1. SIBYLL2.3c-Diff predicts lower number of muons compare to SIBYLL2.3c by approximately 8%, it changes close to EPOS-LHC and QGSJET-II-04 [82].

Appendix B

QGSJET-II-04 with optional single diffraction cross section

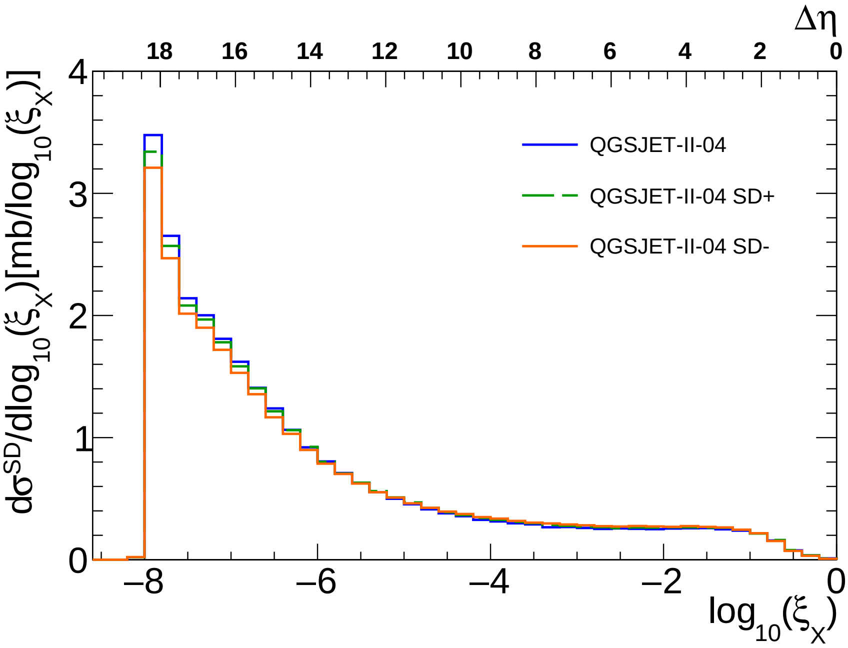

FIGURE B.1: Diffractive mass distribution as a function of $\log_{10}\xi_x$ predicted by QGSJET-II-04, QGSJET-II-04 SD+, and QGSJET-II-04 SD-.

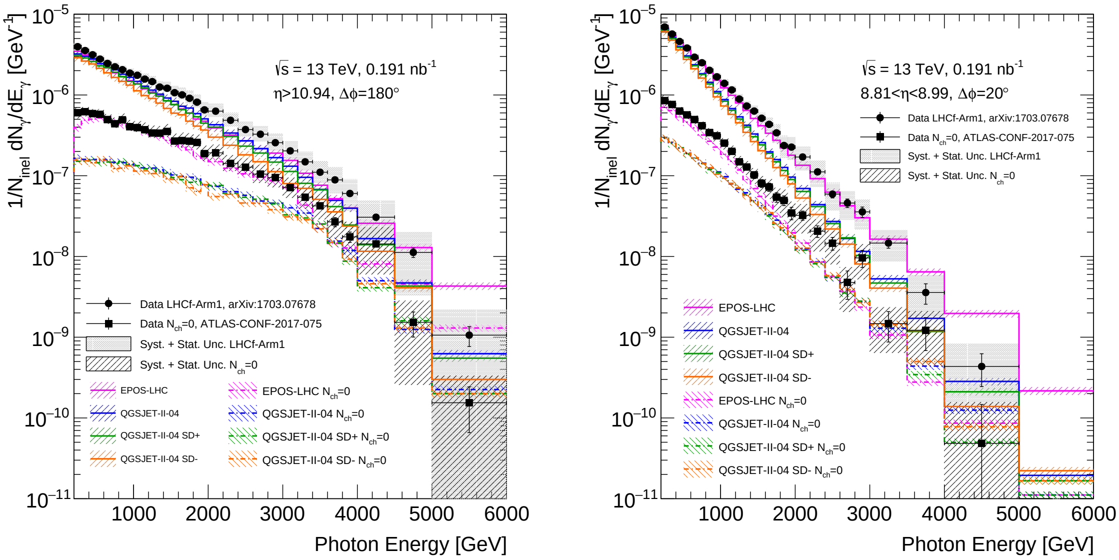

(a) $\eta > 10.94$

(b) $8.81 < \eta < 8.99$

FIGURE B.2: Forward photon energy spectra measured by the LHCf-Arm1 detector in the regions A (left) and B (right). Filled circles show the inclusive-photon spectra measured in Ref. [37]. Filled squares indicate the spectra for $N_{\text{ch}} = 0$ events, where no extra charged particles with $p_{\text{T}} > 100$ MeV and $|\eta| < 2.5$ are present. Vertical bars represent statistical uncertainties of the data sample, while gray bands indicate the quadratic sum of statistical and systematic uncertainties. Colored lines indicate model predictions with (dashed lines) and without (solid lines) the $N_{\text{ch}} = 0$ requirement. Hatched areas around the model lines indicate the 10% uncertainty related to the contribution from photons produced in long-lived particle decays, which is currently not taken into account in the calculation of model predictions.

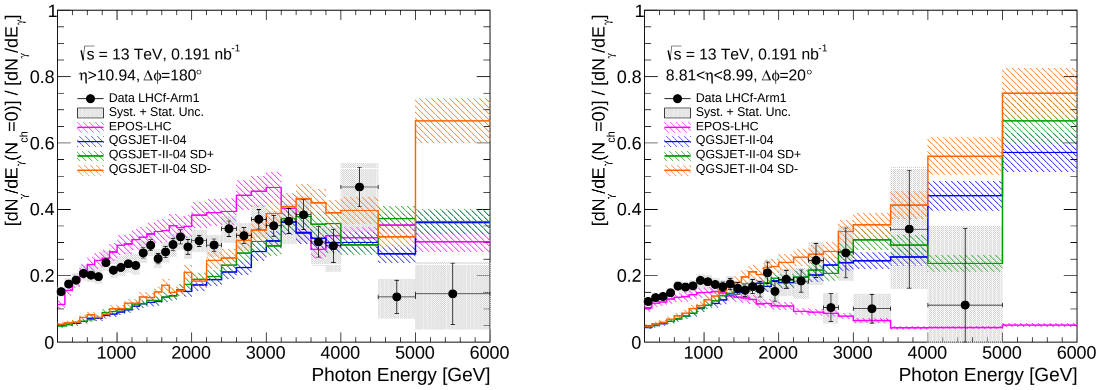

(a) $\eta > 10.94$

(b) $8.81 < \eta < 8.99$

FIGURE B.3: Ratio of the photon energy spectrum with an extra $N_{\text{ch}} = 0$ requirement to the inclusive-photon energy spectrum for regions A (left) and B (right). Vertical bars represent statistical uncertainties of the data sample, while gray bands indicate the quadratic sum of statistical and systematic uncertainties. Colored lines indicate model predictions. Hatched areas around the model lines indicate the 10% uncertainty related to the contribution from photons produced in long-lived particle decays, which is currently not taken into account in the calculation of model predictions.

Appendix C

PYTHIA8212 with MBR pomeron flux

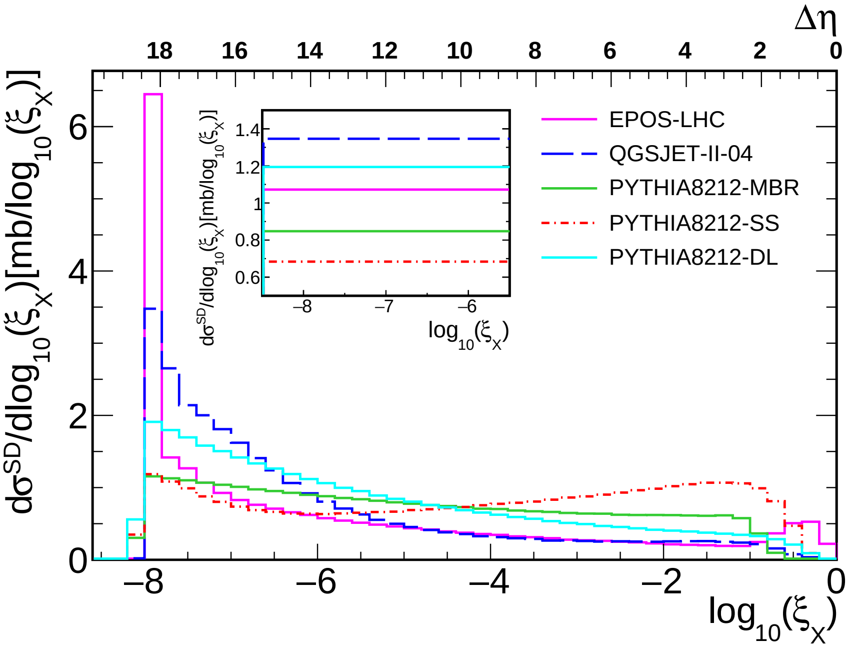

FIGURE C.1: Diffractive mass distribution as a function of $\log_{10}\xi_x$ predicted by default PYTHIA8212, and two optimized models PYTHIA8212-MBR, PYTHIA8212-DL. EPOS-LHC and PYTHIA8212 are shown as references.

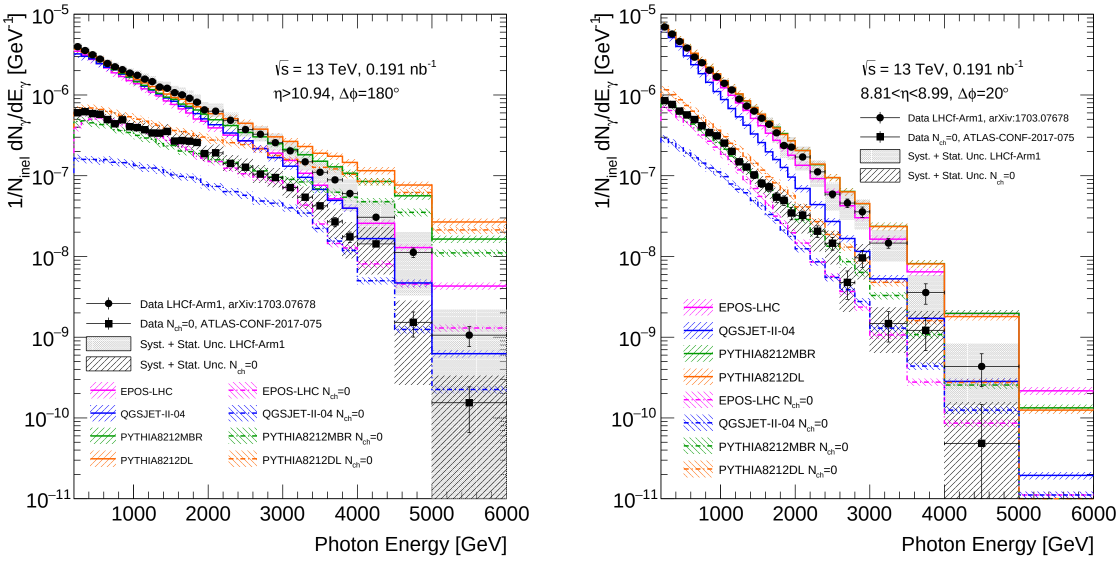

(a) $\eta > 10.94$

(b) $8.81 < \eta < 8.99$

FIGURE C.2: Forward photon energy spectra measured by the LHCf-Arm1 detector in the regions A (left) and B (right). Filled circles show the inclusive-photon spectra measured in Ref. [37]. Filled squares indicate the spectra for $N_{\mathrm{ch}} = 0$ events, where no extra charged particles with $p_{\mathrm{T}} > 100$ MeV and $|\eta| < 2.5$ are present. Vertical bars represent statistical uncertainties of the data sample, while gray bands indicate the quadratic sum of statistical and systematic uncertainties. Colored lines indicate model predictions with (dashed lines) and without (solid lines) the $N_{\mathrm{ch}} = 0$ requirement. Hatched areas around the model lines indicate the 10% uncertainty related to the contribution from photons produced in long-lived particle decays, which is currently not taken into account in the calculation of model predictions.

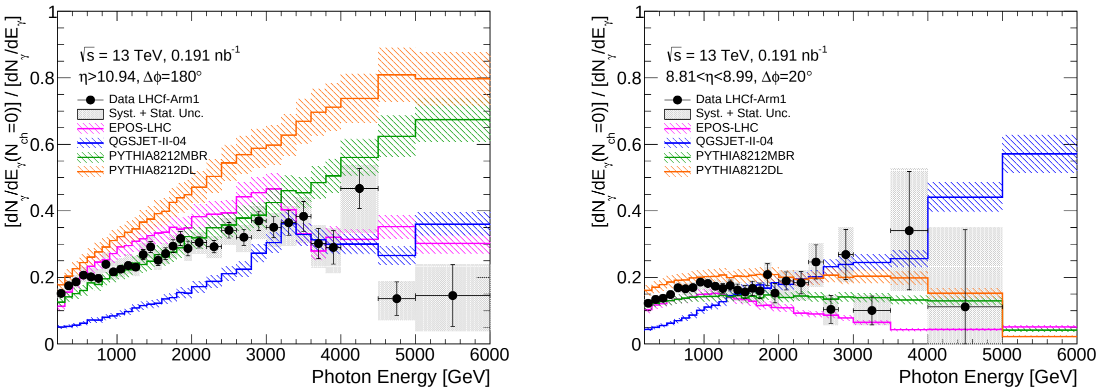

(a) $\eta > 10.94$

(b) $8.81 < \eta < 8.99$

FIGURE C.3: Ratio of the photon energy spectrum with an extra $N_{\mathrm{ch}} = 0$ requirement to the inclusive-photon energy spectrum for regions A (left) and B (right). Vertical bars represent statistical uncertainties of the data sample, while gray bands indicate the quadratic sum of statistical and systematic uncertainties. Colored lines indicate model predictions. Hatched areas around the model lines indicate the 10% uncertainty related to the contribution from photons produced in long-lived particle decays, which is currently not taken into account in the calculation of model predictions.

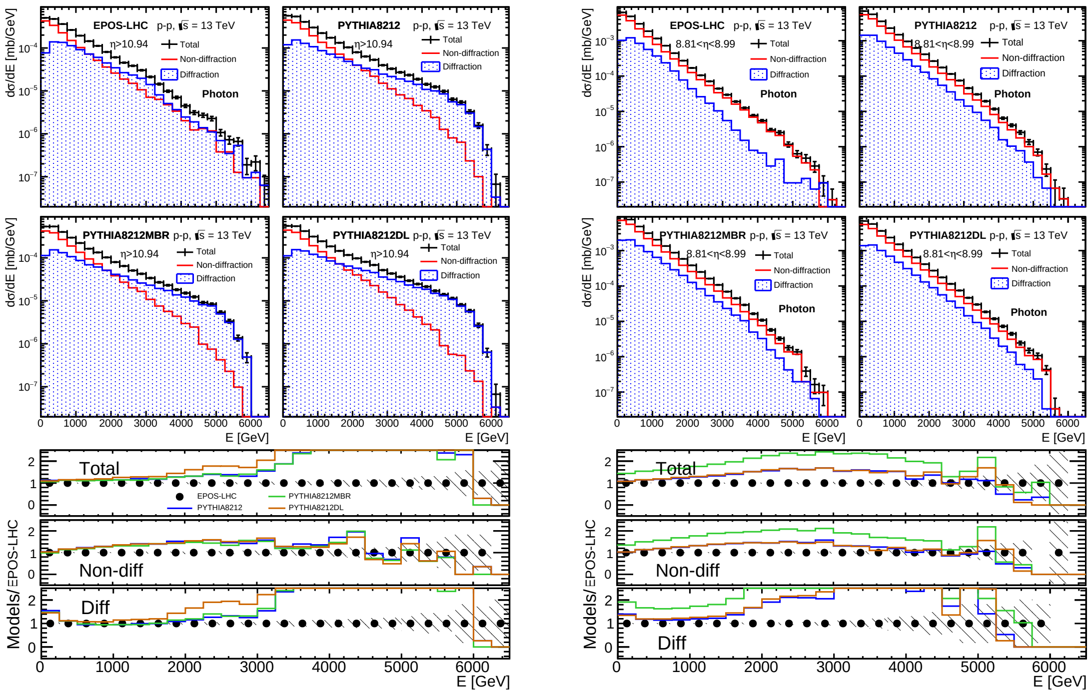

FIGURE C.4: Photon spectra at $\eta > 10.94$ (left) and $8.81 < \eta < 8.99$ (right) (top four panels in each set). These are generated by EPOS-LHC, PYTHIA8212, PYTHIA8212MBR, and PYTHIA8212DL, respectively. The total neutron spectra (black) were classified by nondiffraction (red) and diffraction (blue) according to MC true flags. The bottom three plots show the ratios of the spectrum of EPOS-LHC (black markers), PYTHIA8212 (blue lines), PYTHIA8212MBR (green lines), and PYTHIA8212DL (orange lines) to the spectrum of EPOS-LHC. The top, middle, and bottom plots correspond to total, nondiffraction, and diffraction, respectively.

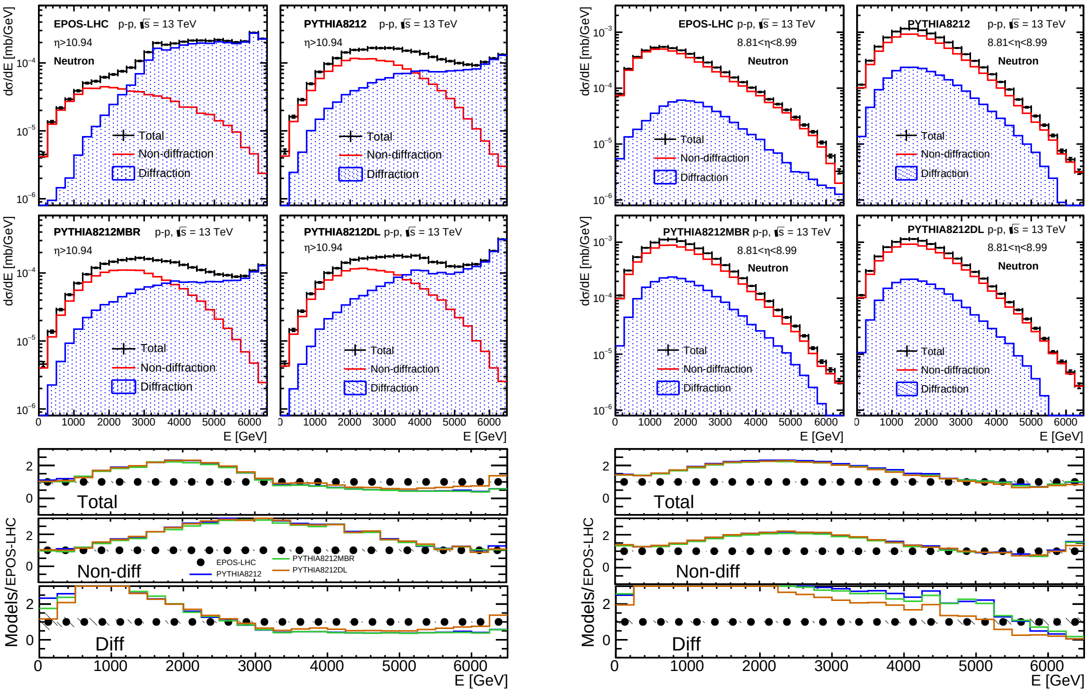

FIGURE C.5: Neutron spectra at $\eta > 10.94$ (left) and $8.81 < \eta < 8.99$ (right) (top four panels in each set). These are generated by EPOS-LHC, PYTHIA8212, PYTHIA8212MBR, and PYTHIA8212DL, respectively. The total neutron spectra (black) were classified by nondiffraction (red) and diffraction (blue) according to MC true flags. The bottom three plots show the ratios of the spectrum of EPOS-LHC (black markers), PYTHIA8212 (blue lines), PYTHIA8212MBR (green lines), and PYTHIA8212DL (orange lines) to the spectrum of EPOS-LHC. The top, middle, and bottom plots correspond to total, nondiffraction, and diffraction, respectively.

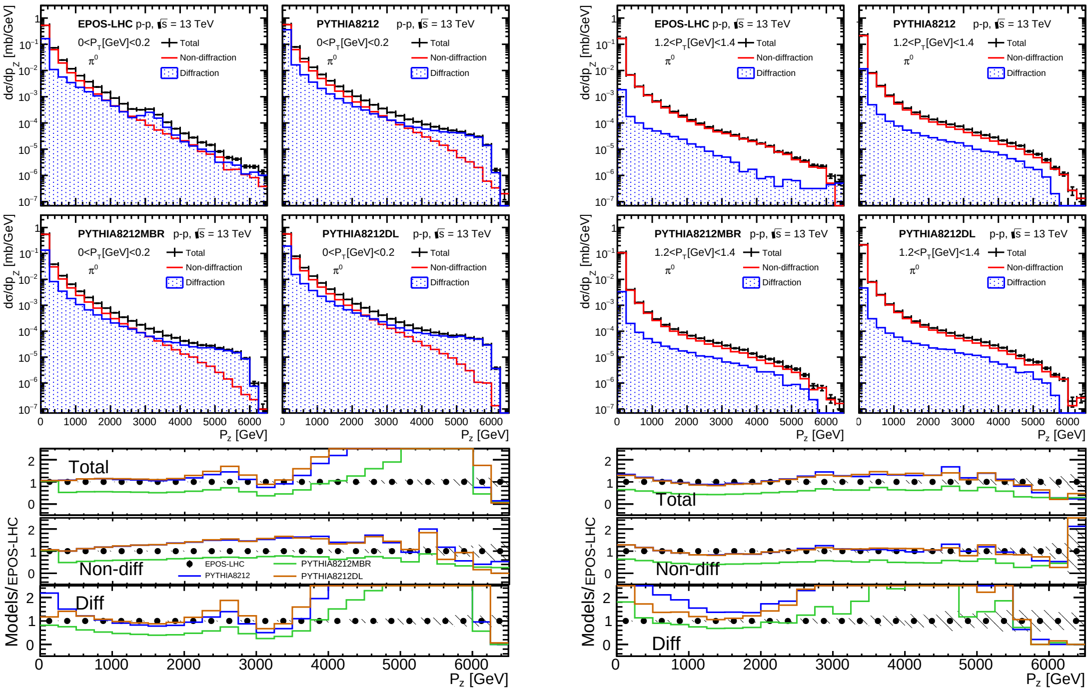

FIGURE C.6: π^0 spectra at $\eta > 10.94$ (left) and $8.81 < \eta < 8.99$ (right) (top four panels in each set). These are generated by EPOS-LHC, PYTHIA8212, PYTHIA8212MBR, and PYTHIA8212DL, respectively. The total neutron spectra (black) were classified by nondiffraction (red) and diffraction (blue) according to MC true flags. The bottom three plots show the ratios of the spectrum of EPOS-LHC (black markers), PYTHIA8212 (blue lines), PYTHIA8212MBR (green lines), and PYTHIA8212DL (orange lines) to the spectrum of EPOS-LHC. The top, middle, and bottom plots correspond to total, nondiffraction, and diffraction, respectively.

Bibliography

[1] V. L. Ginzburg and S. I. Syrovatskii, *Cosmic magnetobremsstrahlung (synchrotron radiation)*, Ann. Rev. Astron. Astrophys. **3** (1965) 297–350.

[2] E. Fermi, *On the Origin of the Cosmic Radiation*, Phys. Rev. **75** (1949) 1169–1174.

[3] E. Waxman, *Cosmological gamma-ray bursts and the highest energy cosmic rays*, Phys. Rev. Lett. **75** (1995) 386–389, `arXiv:astro-ph/9505082 [astro-ph]`.

[4] K. Mannheim and P. Biermann, *Photomeson production in active galactic nuclei*, Astron. Astrophys. no. 221, (1989) 211–220.

[5] Particle Data Group Collaboration, K. A. Olive et al., *Review of Particle Physics*, Chin. Phys. **C38** (2014) 090001.

[6] T. Gaisser, *Cosmic-Ray Showers Reveal Muon Mystery*, APS Physics **9** (2016) 125.

[7] K. Greisen, *End to the cosmic ray spectrum?*, Phys. Rev. Lett. **16** (1966) 748–750.

[8] G. T. Zatsepin and V. A. Kuzmin, *Upper limit of the spectrum of cosmic rays*, JETP Lett. **4** (1966) 78–80. [Pisma Zh. Eksp. Teor. Fiz.4,114(1966)].

[9] Pierre Auger Collaboration, J. Abraham et al., *Measurement of the energy spectrum of cosmic rays above* 10^{18} eV *using the Pierre Auger Observatory*, Phys. Lett. **B685** (2010) 239–246, `arXiv:1002.1975 [astro-ph.HE]`.

[10] Pierre Auger Collaboration, J. Abraham et al., *Observation of the suppression of the flux of cosmic rays above* $4 \times 10^{19} eV$, Phys. Rev. Lett. **101** (2008) 061101, `arXiv:0806.4302 [astro-ph]`.

[11] Telescope Array Collaboration, T. Abu-Zayyad et al., *The Energy Spectrum of Ultra-High-Energy Cosmic Rays Measured by the Telescope Array FADC Fluorescence Detectors in Monocular Mode*, Astropart. Phys. **48** (2013) 16–24, `arXiv:1305.6079 [astro-ph.HE]`.

[12] J. W. Cronin, *Recent results from the Pierre Auger Observatory*, `arXiv:0911.4714 [astro-ph.HE]`.

[13] Pierre Auger Collaboration, A. Aab et al., *The Pierre Auger Observatory: Contributions to the 35th International Cosmic Ray Conference (ICRC 2017)*, 2017. `arXiv:1708.06592 [astro-ph.HE]`. `http://inspirehep.net/record/1617990/files/arXiv:1708.06592.pdf`.

[14] Pierre Auger Collaboration, A. Aab et al., *Depth of maximum of air-shower profiles at the Pierre Auger Observatory. I. Measurements at energies above* $10^{17.8}$ *eV*, Phys. Rev. **D90** no. 12, (2014) 122005, `arXiv:1409.4809 [astro-ph.HE]`.

[15] R. U. Abbasi et al., *Study of Ultra-High Energy Cosmic Ray composition using Telescope Array's Middle Drum detector and surface array in hybrid mode*, Astropart. Phys. **64** (2015) 49–62, `arXiv:1408.1726 [astro-ph.HE]`.

[16] Pierre Auger Collaboration, A. Aab et al., *Muons in air showers at the Pierre Auger Observatory: Measurement of atmospheric production depth*, Phys. Rev. **D90** no. 1, (2014) 012012, `arXiv:1407.5919 [hep-ex]`. [Erratum: Phys. Rev.D92,no.1,019903(2015)].

[17] T. Regge, *Introduction to complex orbital momenta*, Nuovo Cim. **14** (1959) 951.

[18] V. N. Gribov, *A REGGEON DIAGRAM TECHNIQUE*, Sov. Phys. JETP **26** (1968) 414–422. [Zh. Eksp. Teor. Fiz.53,654(1967)].

[19] R. Ulrich, R. Engel, and M. Unger, *Hadronic Multiparticle Production at Ultra-High Energies and Extensive Air Showers*, Phys. Rev. **D83** (2011) 054026, `arXiv:1010.4310 [hep-ph]`.

[20] K.-H. Kampert and M. Unger, *Measurements of the Cosmic Ray Composition with Air Shower Experiments*, Astropart. Phys. **35** (2012) 660–678, `arXiv:1201.0018 [astro-ph.HE]`.

[21] T. Pierog, I. Karpenko, J. M. Katzy, E. Yatsenko, and K. Werner, *EPOS LHC: Test of collective hadronization with data measured at the CERN Large Hadron Collider*, Phys. Rev. **C92** no. 3, (2015) 034906, `arXiv:1306.0121 [hep-ph]`.

[22] S. Ostapchenko, *Monte Carlo treatment of hadronic interactions in enhanced Pomeron scheme: I. QGSJET-II model*, Phys. Rev. **D83** (2011) 014018, `arXiv:1010.1869 [hep-ph]`.

[23] E.-J. Ahn, R. Engel, T. K. Gaisser, P. Lipari, and T. Stanev, *Cosmic ray interaction event generator SIBYLL 2.1*, Phys. Rev. **D80** (2009) 094003, `arXiv:0906.4113 [hep-ph]`.

[24] F. Riehn, R. Engel, A. Fedynitch, T. K. Gaisser, and T. Stanev, *A new version of the event generator Sibyll*, PoS **ICRC2015** (2016) 558, `arXiv:1510.00568 [hep-ph]`.

[25] T. Sjostrand, S. Mrenna, and P. Z. Skands, *PYTHIA 6.4 Physics and Manual*, JHEP **05** (2006) 026, `arXiv:hep-ph/0603175 [hep-ph]`.

[26] T. Sjostrand, S. Mrenna, and P. Z. Skands, *A Brief Introduction to PYTHIA 8.1*, Comput. Phys. Commun. **178** (2008) 852–867, `arXiv:0710.3820 [hep-ph]`.

[27] J. Hamilton, W. Heitler, and H. W. Peng, *THEORY OF COSMIC RAY MESONS*, Phys. Rev. **64** (1943) 78–94.

[28] J. Matthews, *A Heitler model of extensive air showers*, Astropart. Phys. **22** (2005) 387–397.

[29] T. Pierog and K. Werner, *Muon Production in Extended Air Shower Simulations*, Phys. Rev. Lett. **101** (2008) 171101, `arXiv:astro-ph/0611311 [astro-ph]`.

[30] S. Ostapchenko, *LHC data on inelastic diffraction and uncertainties in the predictions for longitudinal extensive air shower development*, Phys. Rev. **D89** no. 7, (2014) 074009, `arXiv:1402.5084 [hep-ph]`.

[31] ATLAS Collaboration, G. Aad et al., *The ATLAS Experiment at the CERN Large Hadron Collider*, JINST **3** (2008) S08003.

[32] CMS Collaboration, S. Chatrchyan et al., *The CMS Experiment at the CERN LHC*, JINST **3** (2008) S08004.

[33] TOTEM Collaboration, G. Anelli et al., *The TOTEM experiment at the CERN Large Hadron Collider*, JINST **3** (2008) S08007.

[34] LHCf Collaboration, O. Adriani et al., *Technical design report of the LHCf experiment: Measurement of photons and neutral pions in the very forward region of LHC*,.

[35] LHCf Collaboration, O. Adriani et al., *Measurement of zero degree inclusive photon energy spectra for* $\sqrt{s} = 900$ *GeV proton-proton collisions at LHC*, Phys. Lett. **B715** (2012) 298–303, `arXiv:1207.7183 [hep-ex]`.

[36] LHCf Collaboration, O. Adriani et al., *Measurement of zero degree single photon energy spectra for* $\sqrt{s} = 7$ *TeV proton-proton collisions at LHC*, Phys. Lett. **B703** (2011) 128–134, `arXiv:1104.5294 [hep-ex]`.

[37] LHCf Collaboration, O. Adriani et al., *Measurement of forward photon-energy spectra for* $\sqrt{s} = 13$ *TeV proton-proton collisions with the LHCf detector*, `arXiv:1703.07678 [hep-ex]`.

[38] LHCf Collaboration, O. Adriani et al., *Measurement of very forward neutron energy spectra for 7 TeV proton–proton collisions at the Large Hadron Collider*, Phys. Lett. **B750** (2015) 360–366, `arXiv:1503.03505 [hep-ex]`.

[39] E. Berti, *Measurement of the energy spectra relative to neutrons produced at very small angle in* $\sqrt{s} = 13$ *TeV proton-proton collisions using the LHCf Arm2 detector*,.

[40] LHCf Collaboration, O. Adriani et al., *Measurement of forward neutral pion transverse momentum spectra for* $\sqrt{s} = 7TeV$ *proton-proton collisions at LHC*, Phys. Rev. **D86** (2012) 092001, `arXiv:1205.4578 [hep-ex]`.

[41] LHCf Collaboration, O. Adriani et al., *Transverse-momentum distribution and nuclear modification factor for neutral pions in the forward-rapidity region in proton-lead collisions at* $\sqrt{s_{NN}} = 5.02\ TeV$, Phys. Rev. **C89** no. 6, (2014) 065209, `arXiv:1403.7845 [nucl-ex]`.

[42] LHCf Collaboration, O. Adriani et al., *Measurements of longitudinal and transverse momentum distributions for neutral pions in the forward-rapidity region with the LHCf detector*, Phys. Rev. **D94** no. 3, (2016) 032007, `arXiv:1507.08764 [hep-ex]`.

[43] E. L. Feinberg and I. Y. Pomeranchuk, *Inelastic diffraction processes at high energies*, Suppl. Nuovo Cim. **4** (1956) 652.

[44] V. Barone and E. Predazzi, *High-Energy Particle Diffraction*, vol. v.565 of *Texts and Monographs in Physics*. Springer-Verlag, Berlin Heidelberg, 2002. `http://www-spires.fnal.gov/spires/find/books/www?cl=QC794.6.C6B37::2002`.

[45] M. G. Ryskin, A. D. Martin, and V. A. Khoze, *High-energy strong interactions: from 'hard' to 'soft'*, Eur. Phys. J. **C71** (2011) 1617, `arXiv:1102.2844 [hep-ph]`.

[46] H. Jung, *Hard diffractive scattering in high-energy e p collisions and the Monte Carlo generator RAPGAP*, Comput. Phys. Commun. **86** (1995) 147–161.

[47] R. L. Cool, K. A. Goulianos, S. L. Segler, H. Sticker, and S. N. White, *Diffraction Dissociation of* $\pi^{\pm}$, $K^{\pm}$, *and* $\rho^{\pm}$ *at 100-GeV/c and 200-GeV/c*, Phys. Rev. Lett. **47** (1981) 701–704. [Erratum: Phys. Rev. Lett.48,61(1982)].

[48] S. Ostapchenko, *Total and diffractive cross sections in enhanced Pomeron scheme*, Phys. Rev. **D81** (2010) 114028, `arXiv:1003.0196 [hep-ph]`.

[49] M. L. Good and W. D. Walker, *Diffraction disssociation of beam particles*, Phys. Rev. **120** (1960) 1857–1860.

[50] ATLAS Collaboration, G. Aad et al., *Rapidity gap cross sections measured with the ATLAS detector in pp collisions at $\sqrt{s} = 7$ TeV*, Eur. Phys. J. **C72** (2012) 1926, `arXiv:1201.2808 [hep-ex]`.

[51] ATLAS Collaboration, G. Aad et al., *Measurement of the Inelastic Proton-Proton Cross-Section at $\sqrt{s} = 7$ TeV with the ATLAS Detector*, Nature Commun. **2** (2011) 463, `arXiv:1104.0326 [hep-ex]`.

[52] CMS Collaboration, S. Chatrchyan et al., *Measurement of the inelastic proton-proton cross section at $\sqrt{s} = 7$ TeV*, Phys. Lett. **B722** (2013) 5–27, `arXiv:1210.6718 [hep-ex]`.

[53] CMS Collaboration, V. Khachatryan et al., *Measurement of diffraction dissociation cross sections in pp collisions at $\sqrt{s}$ = 7 TeV*, Phys. Rev. **D92** no. 1, (2015) 012003, `arXiv:1503.08689 [hep-ex]`.

[54] ALICE Collaboration, B. Abelev et al., *Measurement of inelastic, single- and double-diffraction cross sections in proton–proton collisions at the LHC with ALICE*, Eur. Phys. J. **C73** no. 6, (2013) 2456, `arXiv:1208.4968 [hep-ex]`.

[55] TOTEM Collaboration, G. Antchev et al., *Measurement of proton-proton inelastic scattering cross-section at $\sqrt{s}$ = 7 TeV*, Europhys. Lett. **101** (2013) 21003.

[56] ATLAS Collaboration, G. Aad et al., *The ATLAS experiment at the CERN Large Hadron Collider*, JINST **3** (2008) S08003.

[57] LHCf Collaboration, O. Adriani et al., *The LHCf detector at the CERN Large Hadron Collider*, JINST **3** (2008) S08006.

[58] L. Evans, *The Large Hadron Collider (LHC)*, New J. Phys. **9** (2007) 335.

[59] MIDAS. `http://midas.psi.ch/`.

[60] R. U. C. Baus, T. Pieorg. `https://web.ikp.kit.edu/rulrich/crmc.html`.

[61] P. Skands, S. Carrazza, and J. Rojo, *Tuning PYTHIA 8.1: the Monash 2013 Tune*, Eur. Phys. J. **C74** no. 8, (2014) 3024, `arXiv:1404.5630 [hep-ph]`.

[62] G. A. Schuler and T. Sjostrand, *Hadronic diffractive cross-sections and the rise of the total cross-section*, Phys. Rev. **D49** (1994) 2257–2267.

[63] A. Donnachie and P. V. Landshoff, *Elastic Scattering and Diffraction Dissociation*, Nucl. Phys. **B244** (1984) 322. [,813(1984)].

[64] ATLAS Collaboration, M. Aaboud et al., *Measurement of the Inelastic Proton-Proton Cross Section at $\sqrt{s} = 13$ TeV with the ATLAS Detector at the LHC*, Phys. Rev. Lett. **117** no. 18, (2016) 182002, `arXiv:1606.02625 [hep-ex]`.

[65] H. Jung, *Hard diffractive scattering in high-energy e p collisions and the Monte Carlo generator RAPGAP*, Comput. Phys. Commun. **86** (1995) 147–161.

[66] S. Ostapchenko, *On the model dependence of the relation between minimum-bias and inelastic proton-proton cross sections*, Phys. Lett. **B703** (2011) 588–592, `arXiv:1103.5684 [hep-ph]`.

[67] V. A. Khoze, F. Krauss, A. D. Martin, M. G. Ryskin, and K. C. Zapp, *Diffraction and correlations at the LHC: Definitions and observables*, Eur. Phys. J. **C69** (2010) 85–93, `arXiv:1005.4839 [hep-ph]`.

[68] ATLAS Collaboration, M. Aaboud et al., *Charged-particle distributions at low transverse momentum in $\sqrt{s} = 13$ TeV pp interactions measured with the ATLAS detector at the LHC*, Eur. Phys. J. **C76** no. 9, (2016) 502, `arXiv:1606.01133 [hep-ex]`.

[69] T. A. collaboration, *Measurement of the Inelastic Proton-Proton Cross Section at $\sqrt{s} = 13$ TeV with the ATLAS Detector at the LHC*,.

[70] ATLAS Collaboration, M. Aaboud et al., *Measurement of the Inelastic Proton-Proton Cross Section at $\sqrt{s} = 13$ TeV with the ATLAS Detector at the LHC*, Phys. Rev. Lett. **117** no. 18, (2016) 182002, `arXiv:1606.02625 [hep-ex]`.

[71] V. A. Khoze, A. D. Martin, and M. G. Ryskin, *Total π^+p cross section extracted from the leading neutron spectra at the LHC*, Phys. Rev. **D96** no. 3, (2017) 034018, `arXiv:1705.03685 [hep-ph]`.

[72] R. A. Ryutin, *Total pion–proton cross section from the new LHCf data on leading neutrons spectra*, Eur. Phys. J. **C77** no. 2, (2017) 114, `arXiv:1612.03418 [hep-ph]`.

[73] R. A. Ryutin, V. A. Petrov, and A. E. Sobol, *Towards Extraction of π^+p and $\pi^+\pi^+$ cross-sections from Charge Exchange Processes at the LHC*, Eur. Phys. J. **C71** (2011) 1667, `arXiv:1101.0078 [hep-ph]`.

[74] LHCf Collaboration, O. Adriani et al., *LHCf Detector Performance during the 2009-2010 LHC RUN*, Int. J. Mod. Phys. **A28** (2013) 1330036.

[75] GEANT4 Collaboration, S. Agostinelli et al., *GEANT4: A Simulation toolkit*, Nucl. Instrum. Meth. **A506** (2003) 250–303.

[76] ATLAS Collaboration, G. Aad et al., *The ATLAS Simulation Infrastructure*, Eur. Phys. J. **C70** (2010) 823–874, `arXiv:1005.4568 [physics.ins-det]`.

[77] Y. Makino et al., *Performance study for the photon measurements of the upgraded LHCf calorimeters with Gd_2SiO_5 (GSO) scintillators*, JINST **12** no. 03, (2017) P03023.

[78] ATLAS Collaboration, *Track Reconstruction Performance of the ATLAS Inner Detector at $\sqrt{s} = 13$ TeV*, ATL-PHYS-PUB-2015-018 (2015). `https://cds.cern.ch/record/2037683`.

[79] ATLAS Collaboration, *Improved luminosity determination in pp collisions at sqrt(s) = 7 TeV using the ATLAS detector at the LHC*, Eur. Phys. J. **C73** no. 8, (2013) 2518, `arXiv:1302.4393 [hep-ex]`.

[80] ATLAS Collaboration, *Luminosity determination in pp collisions at $\sqrt{s} = 8$ TeV using the ATLAS detector at the LHC*, Eur. Phys. J. **C76** no. 12, (2016) 653, `arXiv:1608.03953 [hep-ex]`.

[81] ATLAS Collaboration, *Studies of the ATLAS Inner Detector material using $\sqrt{s} = 13$ TeV pp collision data*, ATL-PHYS-PUB-2015-050 (2015). `https://cds.cern.ch/record/2109010`.

[82] F. Riehn, *Private communication*.

[83] Particle Data Group Collaboration, C. Patrignani et al., *Review of Particle Physics*, Chin. Phys. **C40** no. 10, (2016) 100001.